The Thesis Committee for Calvin Blake
Certifies that this is the approved version of the following thesis:

Centrifuge Measurements of Two-Phase Transient Flow in Rigid Porous Media

APPROVED BY
SUPERVISING COMMITTEE:

Supervisor:

Jorge G. Zornberg

Kishore K. Mohanty

Centrifuge Measurements of Two-Phase Transient Flow in Rigid Porous Media

by

Calvin Blake, B.S.

Thesis

Presented to the Faculty of the Graduate School of

The University of Texas at Austin

in Partial Fulfillment

of the Requirements

for the Degree of

Master of Science in Engineering

The University of Texas at Austin

August 2016

Dedication

To the memory of my dear departed grandfather, Thomas S. Blake.

Acknowledgements

I am indebted to Hanna, my wife, for her kind support and encouragement during this research endeavor. Thanks also go to Dr. Jorge Zornberg and Dr. Kishore Mohanty of the University of Texas Civil Engineering and Petroleum Engineering departments, respectively, for their technical guidance and interest in this study, as well as their financial support. I would also like to acknowledge Mr. Gaston Quaglia and Dr. Chammi Miller for their helpful advice and assistance in preparing and operating the laboratory equipment.

Abstract

Centrifuge Measurements of Two-Phase Transient Flow in Rigid Porous Media

Calvin Blake, M.S.E.

The University of Texas at Austin, 2016

Supervisor: Jorge G. Zornberg

Gravity driven multi-phase flow in porous media is an important mode of fluid transport in several geologic settings. Some applications where gravity drainage may play an important role in the movement of a fluid can include primary oil recovery from a petroleum reservoir or water flow into the ground surface. Because of the similarities between a single-gravity environment and a centrifugal environment, measurements of two-phase flow are often conducted in the centrifuge to observe the behavior of the whole system under gravity-like conditions while reducing the time of measurement.

In this study, measurements of transient fluid outflow from sandstone cores were conducted in the centrifuge using air as the invading phase. The draining phase in these experiments comprised three different brines and a light mineral oil. Hydraulic conductivity functions and capillary pressure curves were determined from this data using a numerical history matching technique, and the results were compared with two prevailing analytical models. The results of this study corroborate previous findings that a

full numerical history match can easily predict more realistic hydraulic conductivity functions than the prevailing analytical models.

Table of Contents

List of Tables

List of Figures

Chapter 1: Introduction

1.1: MOTIVATION

Characterization of fluid flow through porous media is critical to many applications in several engineering disciplines, ranging from petroleum extraction from a reservoir or groundwater flow in an aquifer to waste containment and mine tailings dams. In many instances it is necessary to understand how a fluid behaves in a porous material when a second fluid is also present. This is the case, for example, of unsaturated flow in surficial soils or petroleum extraction from rock using a gravity drainage gas-flood combination. The measurement and modeling of gravity drainage in rock is the primary focus of this study, though the results and tools can be extended to deformable soils with some modifications.

Two-phase flow in porous media is governed in general by the capillary pressure – fluid saturation relationship and by the total and relative permeability of the two fluids within the porous matrix.

The capillary pressure relationship also referred to as the retention function or retention curve in the soil science literature, describes how the degree of saturation of one fluid inside the porous material is related to the fluid pressure or suction required to replace it with another fluid. This is typically defined in terms of suction and volumetric water content in soil science, while in petroleum engineering this relationship is typically defined in terms of the more general capillary pressure and the degree of saturation of the pore space, due to general differences in the compressibility of the relevant soil or rock structure in each discipline. Because the two fluids can interfere with one another within the pore space and lead to trapping of isolated pockets of one fluid within the other, the capillary pressure curve is not identical for the drainage and imbibition paths (referred to as the drying and wetting paths in the soil science literature). The drainage path is typically characterized by higher degrees of saturation for any given suction than the imbibition path. The methods described in this study have been developed for the

drainage path, but some modifications can be made to apply them to the imbibition path as well.

In a typical two-phase system, one of the two fluids typically has a greater affinity than the other to be in direct contact with the pore walls of the rock. This fluid is referred to as the wetting fluid. The relative permeability function describes how the permeability of the porous matrix to one fluid (typically the wetting fluid) decreases with decreasing degree of saturation. This occurs because the connected channels within that phase become disconnected or reduced to the more restrictive pathways as the degree of saturation decreases. In applications primarily dealing with air-water systems, the behavior is typically shorthanded as the hydraulic conductivity function (K-function), in which the effects of density and viscosity are grouped into one single term. The methods used in this study are applicable only to the relative permeability of the wetting fluid.

An analogy can be established between pressure displacement and a body force displacement of the wetting phase from a porous matrix based on simple models of the drainage process, however, due to viscous fingering effects in many two-phase systems, the mechanics of the problem tend to result in different fluid recoveries and increased trapping of the wetting phase when pressure displacement methods are used. Hence, in some instances it may be more effective to initially produce a reservoir using a gravity drainage process rather than attempting to force the oil out using a water-flood or a gas-flood. The important issue, then, is to predict the rate of this primary gravity drainage to ascertain whether the rate of production will support the investment in developing the reservoir. Because of the difference in pressure displacement and gravity displacement mechanics, it becomes compelling from a theoretical perspective to model gravity-driven flow processes in a centrifuge, where the application of the centrifugal body force on the pore fluid mimics the force of gravity on the fluid in the real oil reservoir. The centrifuging process also speeds up the rate of flow in the sample due to the increased gravitational gradient, allowing faster determination of rock and fluid properties than in a single-gravity column test.

1.2: Objective and Scope of research

The objective of this study is to measure transient outflow data in the centrifuge in order to determine relative permeability functions and capillary pressure curves for some rigid homogenous rock specimens. An experimental tool to measure transient outflow data from rigid rock cores was developed, and using the experimental results produced in this study, comparisons of the measured behavior are made among four different fluids. Additionally, the relative merits of a few models of the hydraulic conductivity function are explored. This study also serves to demonstrate a baseline level of repeatability for the measurement and interpretation of transient centrifuge outflow time histories.

1.3: Organization of Thesis

This thesis is organized into six chapters. Chapter 1 introduces the motivation and scope of the research, while Chapter 2 describes the basic framework used in the interpretation of transient centrifuge data and introduces several past research efforts in the realm of transient centrifuge measurements of two-phase flow. Chapter 3 introduces the materials and routine characterizations used in this study. A brief description of the development of the experimental environment is included in Chapter 4. The experimental results are outlined in Chapter 5, while the majority of the analysis and reduction of the data is provided in Chapter 6. Our most important conclusions are reported in Chapter 7 to complete the document.

Chapter 2: Background

This chapter introduces the basic mathematical description of fluid flow in porous media and highlights previous research efforts that have captured the several important aspects of transient centrifuge testing and theory. Section 2.1 describes the layout of a typical centrifuge test and outlines the transient centrifugal flow framework used in this study. Typical testing boundary conditions are also discussed in the context of their effect on the conventional interpretation of transient centrifugal data. Section 2.2 visits several previous transient centrifuge studies and their contribution to the current understanding of the transient flow process inside the centrifuge. This study did not examine steady-state centrifuge testing, though several good reports are available in the literature.

2.1 Centrifugal Flow and Richards' Equation for Unsaturated Flow

Centrifuge permeation tests combine the effects of the centrifugal, gravity-like, body force with the simultaneously larger magnitude of the applied force, and hence the gradient in fluid potential itself. This creates an environment in which the flow is driven by similar processes to a single-gravity environment, but also increases the potential energy gradient so that the flow occurs more quickly than in a similarly scaled single-gravity environment. A core of porous material is oriented such that the centrifugal gradient is parallel to the long axis of the core while the centrifuge is rotating, and the sides of the core are sealed with an impermeable sleeve to prevent lateral flow. This creates a 1-dimensional flow regime which simplifies the measurement and interpretation of the data. Fluid outflow from the core is typically collected in a chamber travelling along with the sample, and in which the liquid level can be measured with varying levels of sophistication. Some experimental environments also include additional internal monitoring of the samples to increase the reliability of the measurement.

Figure 2.1 shows a typical non-instrumented testing layout:

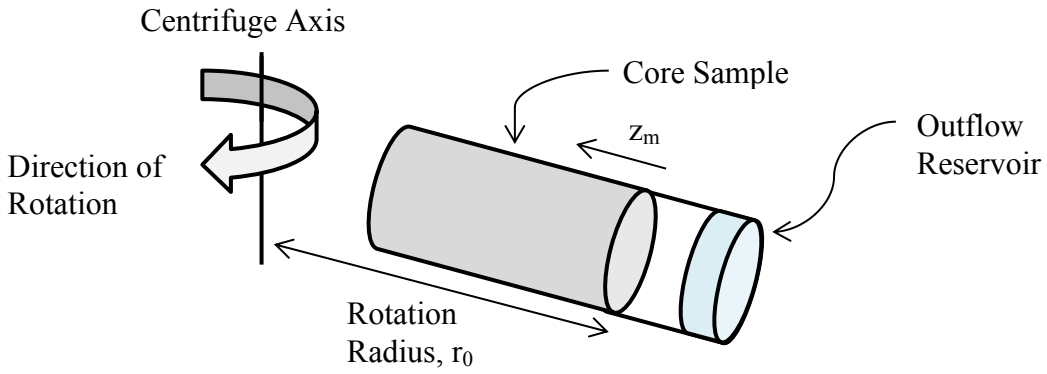

Figure 2.1: Typical Centrifuge Drainage Testing Layout

Darcy's law governs saturated flow in porous media, where the flow velocity is proportional to the applied gradient. The proportionality constant is known as the hydraulic conductivity.

$$v = Ki \tag{2.1}$$

Where v is the flow discharge velocity

K is the hydraulic conductivity

And i is the net gradient in fluid potential.

Similarly, flow of the wetting phase in a two-phase system can be described with Darcy's law, where the hydraulic conductivity is a function of the available flow pathways for the wetting fluid. This is often simply described in terms of the wetting fluid saturation. For a system undergoing drainage, the wetting fluid saturation is itself a function of the capillary pressure, so the hydraulic conductivity is also a function of the capillary pressure, P_c. In this case, Darcy's law can be rewritten as:

$$v = -K(P_c) * i \tag{2.2}$$

For flow in porous media in a centrifugal environment, the gradient can be described by the centrifugal Richards' equation:

$$v = -K(P_c)\left[\frac{\omega^2}{g}(r_0 - z_m) + \frac{1}{\Delta\rho g}\frac{\partial P_c}{\partial z_m}\right] \quad (2.3)$$

Where v is the flow velocity

K is the hydraulic conductivity as a function of the capillary pressure

ω is the rotational speed

g is the constant of gravitational acceleration = 9.81 m/s^2

r_o is the radius to the free water surface in contact with the core

z_m is the coordinate along the length of the core, defined as positive inwards

$\Delta\rho$ is the difference in mass density between the wetting fluid and the displacing fluid

P_c is the capillary pressure, defined in this study as

$$P_c = P_{liquid} - P_{gas} \quad (2.4)$$

P_{gas} is the net pressure inside the gas phase relative to the reference pressure,

And P_{liquid} is the pressure inside the liquid phase.

Note that P_c is defined such that greater pressure inside the liquid than the gas results in a positive value of the capillary pressure, while higher gas pressure results in a negative value. Naturally, this means that the capillary pore is tending to hold the liquid in tension when the liquid pressure is less than the gas pressure. Even though this definition results in negative capillary pressures much of the time in centrifuge testing, the results are typically reported as the absolute value of the suction force, and thus as a positive value.

When the flow velocity is everywhere zero within the specimen, equation 2.3 reduces to:

$$\frac{\omega^2}{g}(r_0 - z_m) = -\frac{1}{\Delta\rho g}\frac{\partial P_c}{\partial z_m} \quad (2.5)$$

which represents a state of force equilibrium between the applied centrifugal potential on the left-hand side of the equation and the capillary pressure on the right-hand side. Additionally, if the gas pressure is the same above and below the specimen, then this state of equilibrium represents the equilibrium between the applied centrifugal potential and the matric potential within the specimen:

$$\frac{\omega^2}{g}(r_0 - z_m) = -\frac{1}{\Delta\rho g}\frac{\partial \psi}{\partial z_m} \quad (2.6)$$

Where

$$\psi = P_{liquid} - P_{gas} = P_{liquid} \tag{2.7}$$

Here a negative matric potential corresponds to a positive matric suction, which facilitates the understanding that pores hold remaining liquid in tension as the sample desaturates. Again, matric suction is typically plotted as positive for simplicity.

The matric suction is very generally a function of the pore size and throat radius and of the interfacial tension as in capillary tubes, though the relationship is more complex than a simple linear tube. Indeed, one of the major objectives in centrifuge testing is the determination of the specific relationship between fluid saturation and the matric suction for a given combination of porous materials and fluids.

It is important to note that the centrifuge itself does not enforce a fluid potential, rather the centrifuge enforces a gravity-like potential *gradient*. This becomes apparent from an examination of the definition of potential energy, which is the work required to displace a body within a conservative force field:

$$U = \int F \cdot dl \tag{2.8}$$

Where *U* is the potential energy

F is the applied force

And *l* is the path length along the gradient of the force field

In a one-dimensional field this becomes:

$$U = \int_{x1}^{x2} F \, dx \tag{2.9}$$

Assuming that a connected rotating body can be modeled as being in a conservative force field, the centrifugal force will be proportional to the radial distance and the square of the rotational speed:

$$F = m\, r\omega^2 \tag{2.10}$$

Where *m* is the mass of the body, and the other variables are as introduced above.

Thus, the fluid potential becomes:

$$U = m * \int_{r}^{r_o} r\omega^2 \, dr \tag{2.11}$$

Where *U* is the potential energy of the body

F is the applied force to the body,

m is the mass of the fluid

r is the radius about the axis of rotation

r_o is the reference radius, properly taken as the radius about the axis of rotation to the free water surface, but often simply taken as the radius to the outflow end of the sample.

ω is the angular frequency of rotation (rad/sec)

We can further speak of the potential, Φ, which is the normalized potential energy per unit volume, or:

$$\Phi = \frac{m}{V} * \int_r^{r_o} r\omega^2 \, dr = \rho * \int_r^{rb} r\omega^2 \, dr \tag{2.12}$$

Consistent with the notation used by Dell 'Avanzi et al (2004) this can be rewritten in the frame of reference of the rotating sample:

$$z_m = r_o - r \tag{2.13}$$

Thus:

$$dz_m = -dr \tag{2.14}$$

and

$$\Phi = -\rho * \int_z^0 r\omega^2 \, dz_m \tag{2.15}$$

Or

$$\Phi_m = \rho * \int_0^z (r_o - z_m)\omega^2 \, dz_m \tag{2.16}$$

The integral is then simply:

$$\Phi_m = \rho \, \omega^2 (r_o - z_m)^2 + C \tag{2.17}$$

where C is the constant of integration, which corresponds to the potential at the lower boundary of the sample. If C is known, then the centrifugal fluid potential throughout the

sample is known from a theoretical standpoint. Figure 2.2 shows a theoretical suction profile at equilibrium when C = 0, derived from the parameters used in Test 17, namely, a speed of 385 RPM and a radial distance, r_o, of 0.54 m, and a wetting fluid specific gravity of 1.0:

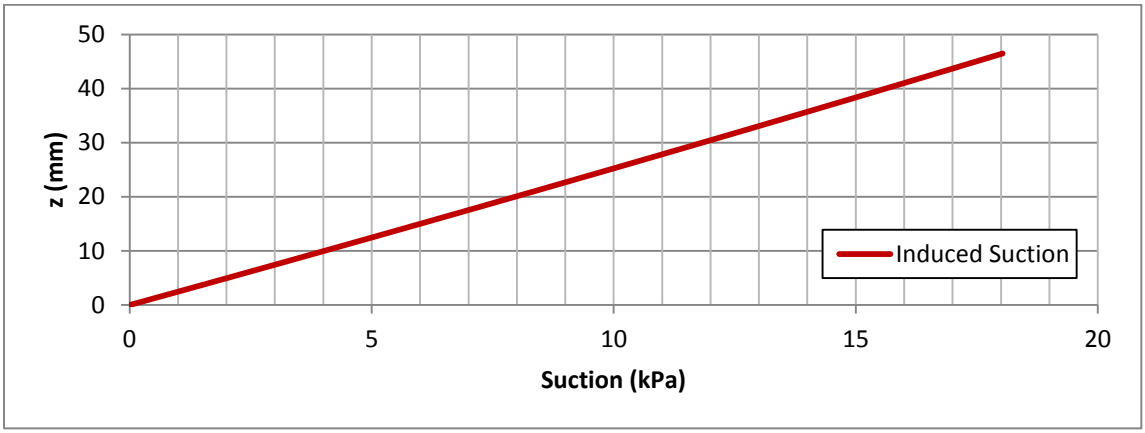

Figure 2.2: Example Centrifugal Suction Profile

For the specific variables used in this particular test, the suction profile is virtually linear because the sample is short compared to the rotational distance. This profile is not linear, however, when the sample length approaches the centrifuge beam length, which is commonly the case in smaller centrifuges.

When speaking of the centrifugal fluid potential, it is appropriate to pick a reference that remains constant throughout the experiment. Many conventional centrifuge experiments have simply assumed that the outflow end of the core, being at a fixed elevation and open to atmospheric pressure, is a good reference to define zero total potential throughout the experiment; the so-called free-flow boundary condition. However, if the outflow end somehow happens to slowly become de-saturated at higher speeds or because of atmospheric drying, then the matric suction will also slowly climb, and thus the centrifugal potential will likewise slowly increase consistent with the mathematical definition of zero total potential at the outflow end. Consequently, neither the centrifugal potential nor the matric suction will be known during the experiment. In order for the

outflow end to desaturate, though, there must be some additional source of potential, such as contact with air at a low relative humidity, or a critical gradient being applied across some of the larger pores causing them to empty (Melrose, 1988), or oscillations in the rotational speed which could cause extra inertial effects not accounted for in the simple model for potential. Because one of the main purposes in using the centrifuge for measurement in the first place is the similarity to a gravitational potential, it is important to know the real centrifugal potential throughout the experiment.

Another way to create the desired boundary condition is to place the outflow end of the sample in contact with a body of the wetting fluid which can drain into a separate collection chamber for measurement. This creates a boundary condition which not only has zero total potential (by definition), but also imposes a zero suction condition by always having the outflow surface saturated with the wetting fluid. This condition also implies a centrifugal potential equal to zero at the outflow end. Having imposed the outflow boundary condition in this way, the centrifugal potential is also imposed throughout the sample, forcing the matric suction inside the sample to respond to the applied centrifugal forces, rather than allowing both to drift because of some unknown potential.

One additional technique to impose the outflow end boundary condition is to use a saturated fine-grained ceramic disc with a high air-entry potential in contact with the wetting fluid to impose a suction value greater than zero due to the restrained column of fluid above the free water surface, as in a conventional hanging column test. However, if the air entry value of the ceramic is exceeded, then the boundary condition becomes less well defined, as in the free-flowing boundary condition.

Thus the outflow boundary condition must be enforced or measured in order to know the true potential within the specimen. Additionally, because the fluid potential is applied via connected chains of pores, any true discontinuities within the matrix can lead to a breakdown in the theory of the centrifugal potential.

The other objective of centrifuge testing is to determine the hydraulic conductivity, or relative permeability, as a function of the wetting fluid saturation. The observed general

behavior is that the material becomes increasingly less permeable to the wetting fluid as the saturation of the wetting fluid decreases, because the connected pathways within the wetting fluid become increasingly restricted to the smaller pores as the degree of saturation drops.

In order to determine this function, both the fluid saturation and the net gradient in potential must be known at the same location along the core. The hydraulic conductivity at any location, z_m, can then simply be calculated from a rearrangement of equation 2.3 above:

$$K(z_m) = -\frac{v(z_m)}{\left[\frac{\omega^2}{g}(r_0 - z_m) + \frac{1}{\Delta\rho g}\frac{\partial P_c(z_m)}{\partial z_m}\right]} \tag{2.18}$$

In the absence of localized measurements of the capillary pressure and flow velocity along the length of the core, the hydraulic conductivity function can be estimated by fitting a transient solution for this equation to the measured transient outflow data. In this case, the functions describing the unsaturated hydraulic conductivity and capillary pressure-saturation curve are assumed before conducting a forward solution. A number of functions can then be tried successively until a close match with the data is found. Our implementation of this process is described in more detail in Appendix A.

The Van Genuchten- Mualem model (Van Genuchten, 1980) was used as the basis for the transient history matching in this study. The equation describing the retention curve in this model is:

$$\theta = (\theta_s - \theta_r)\left(\frac{1}{1+(\alpha_s\psi)^{n_s}}\right)^{m_s} + \theta_r \tag{2.19}$$

Where θ is the volumetric wetting fluid content, defined as :

$$\theta = \frac{V_{liquid}}{V_{total}} = \frac{S}{\phi} \tag{2.20}$$

Where V_{liquid} is the volume of liquid inside the sample

V_{total} is the total volume of the sample

S is the degree of saturation of the wetting fluid,

and ϕ is the porosity, defined as:

$$\phi = \frac{V_{pores}}{V_{total}} \tag{2.21}$$

Other parameters in the Van Genuchten model are as follows:

θ_s is the saturated volumetric fluid content, typically equal to the porosity in a two-phase system

θ_r is the residual volumetric fluid content

ψ is the matric suction

and α_s, n_s, and m_s are additional fitting parameters to describe the shape of the curve, where:

$$m_s = 1 - \frac{1}{n_s} \tag{2.22}$$

The hydraulic conductivity function in the original Van Genuchten- Mualem model is given by:

$$K(\psi) = K_{sat} * \frac{\left(1-(\alpha\psi)^{n-1}\,(1+(\alpha\psi)^{n})^{-m}\right)^{2}}{(1+(\alpha\psi)^{n})^{m/2}} \tag{2.23}$$

Where α, n, and m are as before,

And K_{sat} is the saturated hydraulic conductivity.

The specific Van Genuchten-type hydraulic conductivity model used in the majority of this study has the same form as Equation 2.23, but defines a separate α and n independent of the retention curve. These are denoted with a subscript k to distinguish them from the retention parameters:

$$K(\psi) = K_{sat} * \frac{\left(1-(\alpha_k\psi)^{n_k-1}\,(1+(\alpha_k\psi)^{n_k})^{-m_k}\right)^{2}}{(1+(\alpha_k\psi)^{n_k})^{m_k/2}} \tag{2.24}$$

Where m_k is defined in terms of n_k as before.

2.2 PREVIOUS RESEARCH

Centrifuge testing has made significant advances in the last hundred years, from the earliest soil moisture equivalent to full time-history matching on carefully measured

transient flow data Simunek & Nimmo (2005). In 1945, Hassler and Brunner developed a centrifuge method to measure the outflow from a core sample with a stroboscope and relate the true capillary pressure curve to the average moisture content remaining in the sample and the applied suction gradient. They rightly observed that the measurement only produces the average water content as a function of the average applied suction, and proposed a procedure to estimate the true retention curve from their measurements. This analysis is predicated on the assumption that the outflow end of the core remains saturated throughout the test. Melrose (1988) investigated the validity of this so-called Hassler assumption, and determined that even for reasonably highly permeable rocks (1000 mD or less) the outflow end of the core likely does remain saturated even at reasonably large g-levels.

Hagoort (1980) developed a method to predict the relative permeability of the wetting phase from a single-speed transient centrifuge test. His method requires a reasonably large g-level and makes the assumption that the interface between the draining liquid and the invading gas creates a reasonably distinct shock front, behind which the remaining liquid drains according to the relative permeability alone. In this approach, the necessary assumption is that the zone near the outflow end actually desaturates after a shock front in the fluid passes, and that capillary gradients do not affect the flow behind the shock front.

Firoozabadi & Aziz (1986) demonstrated the non-uniqueness of the parameter estimation from a history match of transient data using a numerical simulator which accounted for the capillary pressure in addition to relative permeability. They found that a near perfect history match could be made with arbitrarily small values of the capillary pressure, but that the relative permeability curves in this case did not match the relative permeability curves obtained when using experimentally justifiable capillary pressures, contradicting one of the primary assumptions in Hagoort's work mentioned previously. They also caution against making the typical assumption that the gas/oil mobility ratio is negligible in the high saturation range in centrifuge testing.

Nimmo (1990) developed a transient test method in which initially water saturated samples of soil were successively drained at various speeds, and real-time internal measurements of the electrical resistivity were correlated to the internal saturation distribution in flight. They compared their transient centrifuge measurements against hydraulic conductivity and retention parameters previously derived for their soils. Based on their measurements, they were able to confirm that the centrifugal Richards' equation is valid, at least within a factor of 4.

Reis et al. (2011) developed an un-instrumented centrifuge test methodology to determine the retention and K function for soil samples using a simplified estimate of the transient suction profile in flight, and by imposing increased suctions at the outflow boundary by means of saturated porous ceramic stones in contact with the outflow reservoir.

Simunek and Nimmo (2005) developed a transient centrifuge module for the HYDRUS^{TM} software to simulate direct and inverse flow problems. They claim the ability to optimize hydraulic conductivity function and retention function variables from a transient outflow centrifuge test, given outflow values and internal measurements of saturation.

Chen & Balcom (2005) measured the water content in a Berea sandstone sample using Magnetic Resonance Imaging after 2 hours of centrifuging at moderate speeds to predict the actual retention curve, and determined good fits between their results and the mercury intrusion method. It is important to note that this method does not quantify the effects of fluid redistribution once the centrifugal gradient has been removed, so some additional uncertainty is present in the results of such a measurement.

In this study, we make use of several of the concepts presented above to measure transient centrifuge outflow from single and multi-step experiments. The primary objective is to examine the reliability in measuring the capillary pressure – fluid saturation relationship in the centrifuge, and to predict the hydraulic conductivity as a function of fluid saturation from transient centrifuge tests. Several details of testing procedures are discussed, and a comparison is made between measurements on four fluid types within the same rock matrix. The results of this study support many of the findings

in the literature, and pave the way for future studies in this laboratory on less conventional porous media and fluid combinations.

Chapter 3: Material Characterization

The materials used in this study are presented in this section. Berea Sandstone samples were prepared with four different fluids including a sodium chloride brine, two additional brines with different common surfactants that modify the interfacial tension, and a light mineral oil. A number of characterization tests were performed on the rock cores and the fluids. These included the determination of the air-filled porosity of the cores, measurements of viscosity and interfacial tension of the fluids, and the saturated hydraulic conductivity of the whole system.

3.1 Sandstone Core Samples

The samples of porous media used in these experiments were small plugs of Berea Sandstone. Berea Sandstone™ is the trade name for a relatively homogeneous sandstone naturally occurring in northern Ohio and marketed by the Cleveland Quarries of Amherst, Ohio. The material is quarried from the Devonian and Mississippian age belts of sedimentary rock which stretch from South to North across the center of the state. This sandstone is a commonly used outcrop rock in laboratory verification of various oil recovery technologies, as it is readily available and inexpensive (Shaw et al 1991). The material is predominantly composed of quartz grains bonded by additional silica, though a small percentage of clay fines exist. The results of several XRD Analyses presented by Shaw et al. (1991) are reproduced in Table 3.1:

Table 3.1: Berea Sandstone Mineral Characterization adapted from Shaw et al (1991)

Bulk Analysis			
Mineral (%)	Shaw et. al. (1991)	Khilar and Folger (1983)	Azari and Leimkuhler (1990)
Quartz	82.5	76	84
Feldspar	3.8	9	3
Calcite	Trace	1	1
Dolomite	1.2	4	1
Kaolinite	9.7	7	-
Chlorite	1.3	1	-
Illite/Mica	1.5	1	-
Siderite	-	1	1
Total Clay	12.5	9	10

Fines Analysis (<2 μm)		
Mineral (%)	Shaw et. al. (1991)	Azari & Leimkuhler (1990)
Quartz	2.0	-
Kaolinite	79.0	76
Illite/Smectite	7.4	trace
Illite/Mica	7.3	20
Chlorite	3.5	4
Feldspar	0.8	-
Dolomite	trace	-

Generally, the amount of Quartz is on the order of 75-85%, while the amount of clay minerals present is on the order of 10%, the majority of which is Kaolinite. Because of the presence of these clay minerals in the sandstone, the water-based liquids in this study were mixed with about 3% NaCl by weight to suppress swelling of the clay minerals.

3.2 CORE PREPARATION

The experimental samples used in this study were 1.5-inch diameter, 2-inch long cores of Berea Sandstone drilled parallel to the bedding plane (Figure 3.1b). The cores were initially cut from a block using water as the cutting fluid. They were then oven dried, weighed, and wrapped in heat-shrink tubing to help enforce a 1-D flow regime. The air-filled pore volume, and hence porosity, was determined using Boyle's Law and the

measured pressure-volume relationship between the core and a known volume of air. A diagram of the process is shown in Figure 3.1a. A control chamber of known volume (V_A) is isolated from the core (V_B) by a valve. Then the pressure in the control chamber is increased to a known value (P_A). The air pressure inside the core is measured (P_B), and then the valve between the two is opened. The air pressure in both volumes now equalizes to an intermediate pressure (P_C).

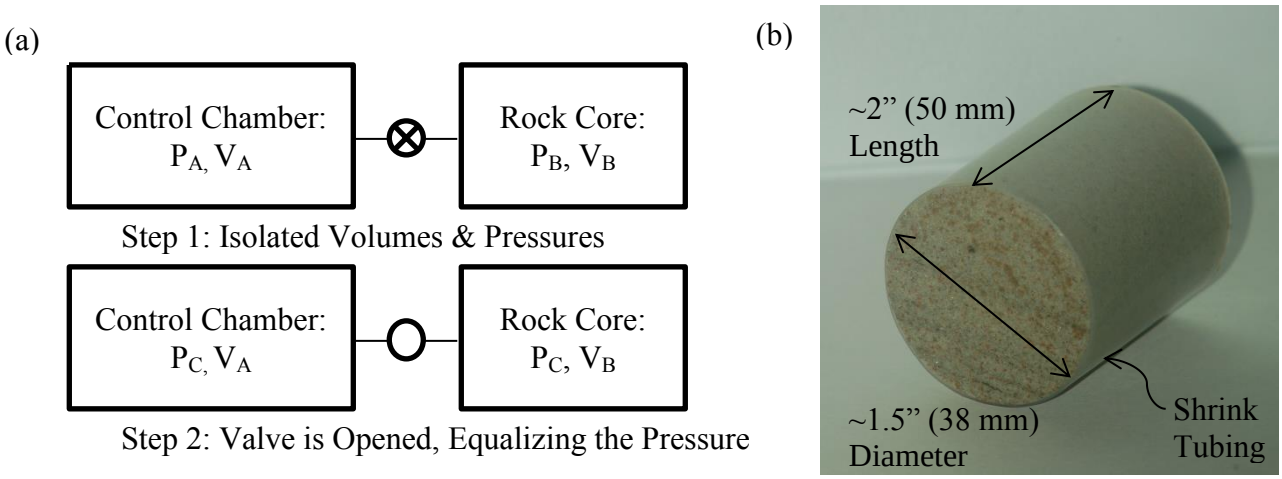

Figure 3.1: (a) Schematic of Air-filled Porosity Determination (b) Berea Sandstone Sample

The temperature is held constant, and because the system is a closed system, the number of gas molecules also remains constant. Thus, the change in pressure inside the known volume V_A is dependent on the unknown volume, V_B, according to Boyle's Law:

$$P_A V_A + P_B V_B = P_C V_A + P_C V_B \tag{3.1}$$

Or:

$$V_B = \frac{(P_A - P_C) * V_A}{P_C - P_B} \tag{3.2}$$

The porosity is then simply:

$$\phi_{Air\ filled} = \frac{V_B}{V_{Total}} \tag{3.3}$$

Some calibrations must be done on the apparatus to determine the volumes of sensors and connecting lines, but the principle is identical. The porosity of these cores was determined by this process to be 0.227.

The cores were initially saturated as 4-inch long cores with a 3% NaCl Brine in a pressure-displacement-based saturation device, and the permeability was measured at a confining pressure of about 1,000 psi. Finding that the cores were initially too long to fit in the available core holders, they were then cut in half (to a length of 2") using tap water as the cutting fluid, and re-weighed. For the first segment of the centrifuge testing program, the cores were re-saturated in the same high pressure device after every centrifuge run. Before the final segment of the testing program, the cores were re-saturated in a flexible wall permeameter device under vacuum and the permeability was checked at low net confining pressures of about 15 psi. After a sufficient number of tests were run with the brine as the wetting fluid, each core was re-saturated with a different wetting fluid for further testing.

The specific dimensions and characteristics of each core tested as part of this study are included in Table 3.2:

Table 3.2: Characteristics of Berea Sandstone Samples

Sample ID	Rock Type	Length (mm)	Diameter (mm)	Air-Filled Porosity	Pore Volume (mL)	Dry Mass † (g)	Saturated Mass *† (g)
BS-A1	Berea Sandstone	50.7	37.8	0.227	12.90	125.49	138.39
BS-A2		46.5	37.8	0.227	11.83	115.28	127.11
BS-B1		48.6	37.8	0.227	12.33	120.13	132.46
BS-B2		48.7	37.8	0.227	12.38	119.81	132.19

† Including mass of permanent shrink wrap

* Based on water with a density of 1.0 g/mL

3.3 FLUID VISCOSITY

The viscosity of fluids used in this study was measured using the cup and bob method. The apparatus was an Anton-Paar Physica 301 rheometer, which allows the control of

strain rate and temperature to the nearest 0.01°C. The machine measures the torque applied to the spinning bob while simultaneously measuring the rate of rotation. The dynamic viscosity is then computed as the measured shear stress divided by the strain rate:

$$\mu = \frac{\tau}{\frac{d\gamma}{dt}} \tag{3.4}$$

Ramped strain rate tests were run from 0 to 1000 1/s at a series of temperatures ranging from 19 °C to 33 °C for these fluids.

A plot of the measured viscosity vs strain rate is shown in Figure 3.2 for the three water-based fluids at 23 °C:

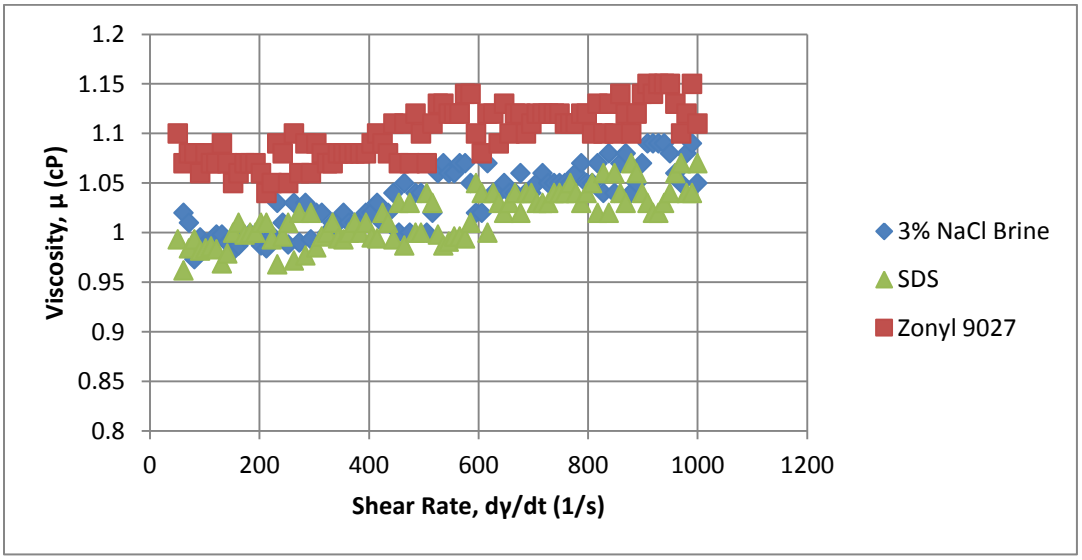

Figure 3.2: Shear Rate Dependence of Fluid Viscosity

These fluids all exhibit minimal dependence of the viscosity on the strain rate, with a slope of about $1x10^{-4}$ cP-s. Because the strain rates used in the centrifuge testing are reasonably similar among tests and are relatively small, a single average value was deemed sufficient to describe the viscosity of each fluid as a function of temperature. The average measured values for each trial are plotted in Figure 3.3 against temperature for all four fluids:

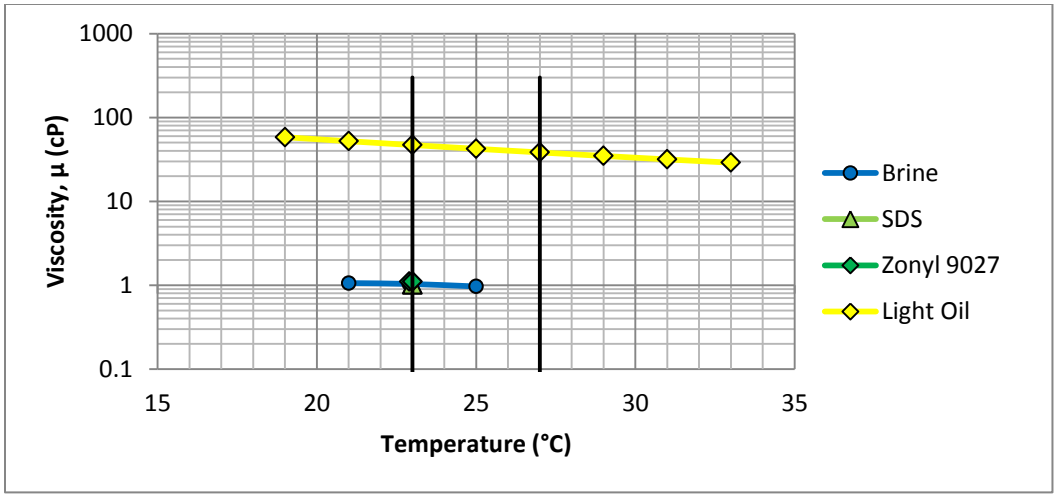

Figure 3.3: Temperature Dependence of Fluid Viscosity

From the data shown in Figure 3.3, brine and surfactant solutions were found to exhibit only minimal dependence of the viscosity upon the temperature. The light oil, as expected, has a much larger dependence on the temeprature. Because the large permeameter centrifuge has only passive temperature control, the temperature does change as a function of centrifuge speed. However, based on the range of temperatures measured in the centrifuge and the range of viscosity values for this oil, the changing viscosity with temperature should not be significant for the simple transient analysis as originally developed in this study.

3.4 Interfacial Tension

The interfacial tension between each fluid and air was measured using a Ramé-hart model 500 contact angle goniometer and tensiometer. A droplet of fluid is extruded from a small diameter needle while a camera records the droplet size and shape. When the contact angle becomes 90° and the droplet breaks off, the instrument calculates the maximum size of the droplet, and infers the tension force which had previously held the droplet.

Table 3.3 shows the measured values of interfacial tension between the 4 fluid types and air:

Table 3.3: Measured Liquid-Air Interfacial Tension

Fluid	Fluid-Air Interfacial Tension (mN/m)
3% NaCl Brine	72.0
3% NaCl - 0.25% Sodium dodecyl sulfate (SDS)	30.0
3% NaCl - Zonyl 9023	52.0
Light Mineral Oil	28.5

The Zonyl solution has an interfacial tension of about 52 mN/m. This is much larger than typically exhibited by this surfactant at this concentration; however, this particular batch of the surfactant was sufficiently old enough that the properties may have degraded with time. It is still meaningful, however, to run tests on this fluid for the later purpose of exploring the effect of the interfacial tension on the retention curve, as the real value of the interfacial tension is the controlling factor, and not the age of the surfactant. Nevertheless, the results of this particular batch should not be expected generally to apply to solutions containing Zonyl 9023.

3.5 Saturated Hydraulic Conductivity

Two sets of measurements of the saturated hydraulic conductivity were conducted on the sandstone cores. The first set was performed in the petroleum laboratory immediately after the cores were saturated with brine for the first time, and before cutting them in half. The second set was performed in the geotechnical laboratory after several centrifuge tests were run on the samples, and coincident with the final resaturation for the last set of centrifuge tests.

The flexible wall permeameter, pictured in Figure 3.4, was used to prepare the cores before the final testing segment. This apparatus allows the application of a comparatively small confining pressure to the rock sample while a small gradient is placed across the sample using a different pore fluid to measure the hydraulic conductivity.

Figure 3.4: Flexible Wall Permeameter Testing Arrangement

The pressure source is an 80-psi maximum building air supply. Volumes are manually read from a meniscus between the supplied air and water in the system. Toxic interface units allow the applied pressure to be transferred from the water in the graduated tubes to the actual pore fluid through a flexible rubber membrane. Tubing then connects the interface unit to the endcaps on the rock. The endcaps have a pattern of radial and concentric grooves to allow near-free passage of fluid while being in direct contact with the rock itself as seen in Figure 3.5. Two ports at either end of one of the radial grooves allow the endcap to be partially flushed of air before running a permeability test, though the applied pressure during tests is still high enough to dissolve most of the remaining air inside the sample.

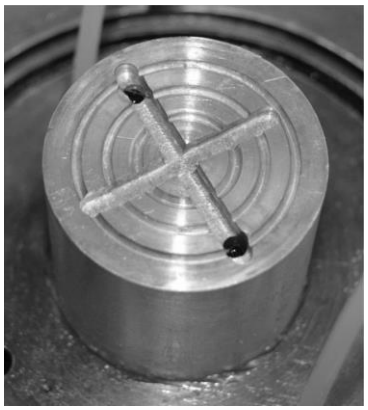

Figure 3.5: Endcap Design for Flexible Wall Permeameter

The hydraulic conductivity was measured using the falling head - rising tail method, in which the headwater pressure drops while the tailwater pressure rises during the experiment due to the constrained flow inside the system.

The hydraulic conductivity is calculated as (Daniel 1989):

$$K = \frac{aL}{2A\,\Delta t} ln\left(\frac{\Delta h_1}{\Delta h_2}\right) \tag{3.5}$$

Where

K is the hydraulic conductivity [m/s]

a is the area of the graduated head and tailwater tubes [m^2]

A is the cross sectional area of the sample [m^2]

Δt is the elapsed time between readings 1 and 2 [s]

Δh_1 is the difference in head across the sample at time 1 [m]

And Δh_2 is the difference in head across the sample at time 2 [m]

The system as pictured in Figure 3.4 has about 3m of 1/16" I.D. tubing. Given the measured flowrates during testing, the calculated Reynolds number is generally less than 0.1 and the flow is laminar, where:

$$Re = \frac{\rho v d}{\mu} \tag{3.6}$$

Re is the Reynold's number for pipe flow

ρ is the fluid mass density

V is the average fluid velocity

D is the hydraulic diameter of the tube

And μ is the viscosity of the fluid.

Taking the Darcy friction factor for laminar pipe flow, f_D as:

$$f_D = \frac{64}{Re} \tag{3.7}$$

The headloss in the tubing per unit length, h_f can be calculated using the Darcy-Weisbach equation:

$$h_f = f_D \frac{L}{d} \frac{v^2}{2g} \tag{3.8}$$

Were L is the length of the pipe

And the other variables are as introduced above.

The length of tubing in the apparatus is about 3.2m, and typical calculated values of head lost in the tubing were on the order of 0.01m out of the 2 to 3m applied across the sample, so viscous losses in the system here may be considered negligible.

Using the flexible wall permeameter, the results of the measured hydraulic conductivity using the falling head, rising tail technique are shown below in Figures 3.6 and 3.7. Measured hydraulic conductivities in the Berea Sandstone were on the order of $1x10^{-4}$ cm/s for the water based fluids and on the order of $1x10^{-5}$ cm/s in the light oil. The intrinsic permeability, k, is given by the equation:

$$k = K \frac{\mu}{\rho g} \tag{3.9}$$

Where k is the intrinsic permeability [mD]

K is the hydraulic conductivity [m/s]

μ is the fluid viscosity

and ρ is the wetting fluid density.

The measured permeability is about 175 to 240 mD for all cores using the water-based fluids. The oil-saturated core consistently had a permeability closer to 600 to 640 mD, or about three times that measured with the water-based fluids. A few possible reasons for this trend exist. If the brine concentration was not large enough to fully suppress the diffuse double layer in any clay minerals, then the use of mineral oil may further suppress

the swelling clays opening the flow pathways slightly wider and increasing the permeability. Another possibility is that the brine-based cores may not have been fully saturated, and so the slight difference in saturation leads to a lower permeability. Finally, there exists a slight possibility that an air bubble was present in the lower endcap in the water-based fluids, leading to an obstruction in the flow pathway, and reducing the measured conductivity in the cores.

Several repeat measurements were performed on each core to verify repeatability of the measurement. One such set of measurements on the oil-saturated core at 25°C is shown in Figure 3.6:

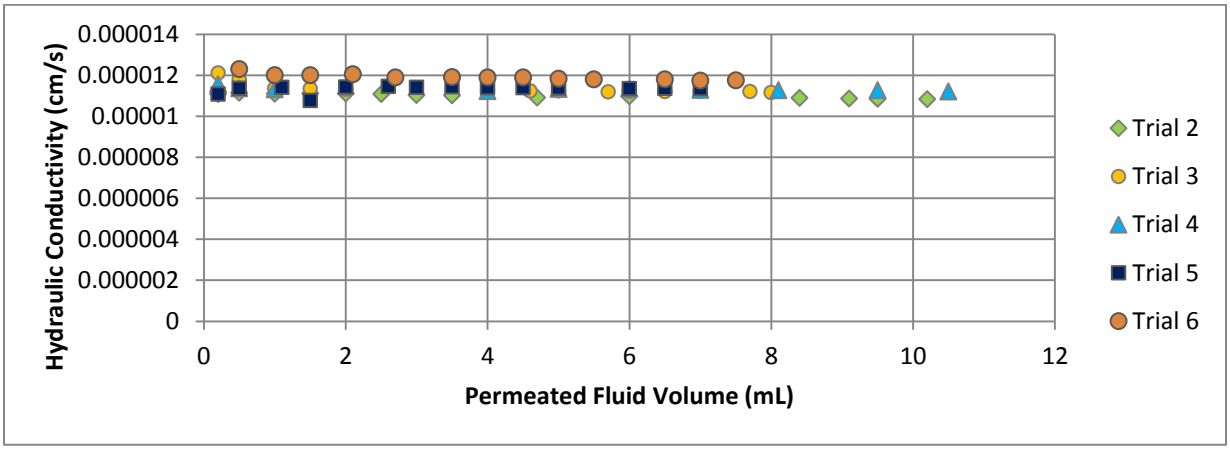

Figure 3.6: Saturated Hydraulic Conductivity of Oil-Saturated Core

The results from all cores are plotted in Figure 3.7

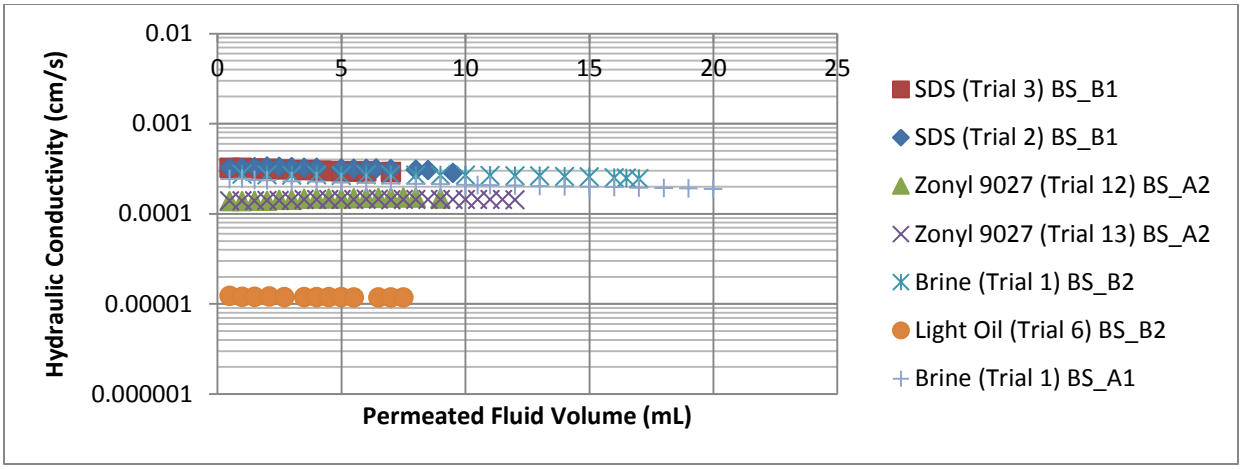

Figure 3.7: Saturated Hydraulic Conductivity for All Cores

Based on this set of measurements, it appears that there may have been a bubble in the lower endcap for many of the water-based fluids, which would cause the measurement to be highly dependent on the applied gradient as well as on the direction of flow. Figure 3.8 shows this effect of the air bubble, where the normal flow direction from bottom to top creates a decrease in the measured conductivity with a decrease in gradient, whereas the reverse flow from top to bottom exhibits an increase in the measured hydraulic conductivity with a decrease in gradient, corresponding to fewer other viscous losses in the system. The results plotted in gray are from an initial series of tests in which an O-ring spacer was placed between the rock and the endcap to increase the availability of fluid to the rock, which incidentally created a space which was not physically able to be flushed. This increases the probability that an air bubble is blocking some of the flow paths, which explains the large drop in conductivity with the drop in gradient during a test.

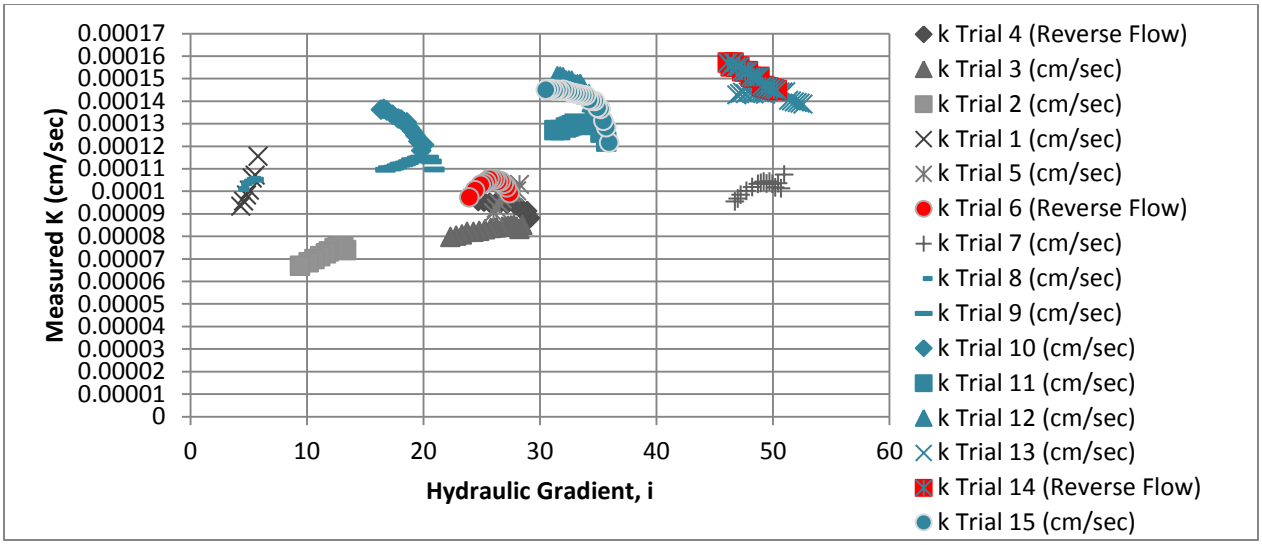

Figure 3.8: Gradient Dependence of Hydraulic Conductivity Measurement

Furthermore, the results plotted against time show that the sample was quite likely still saturating as well, since the general measurement of K does increase with time.

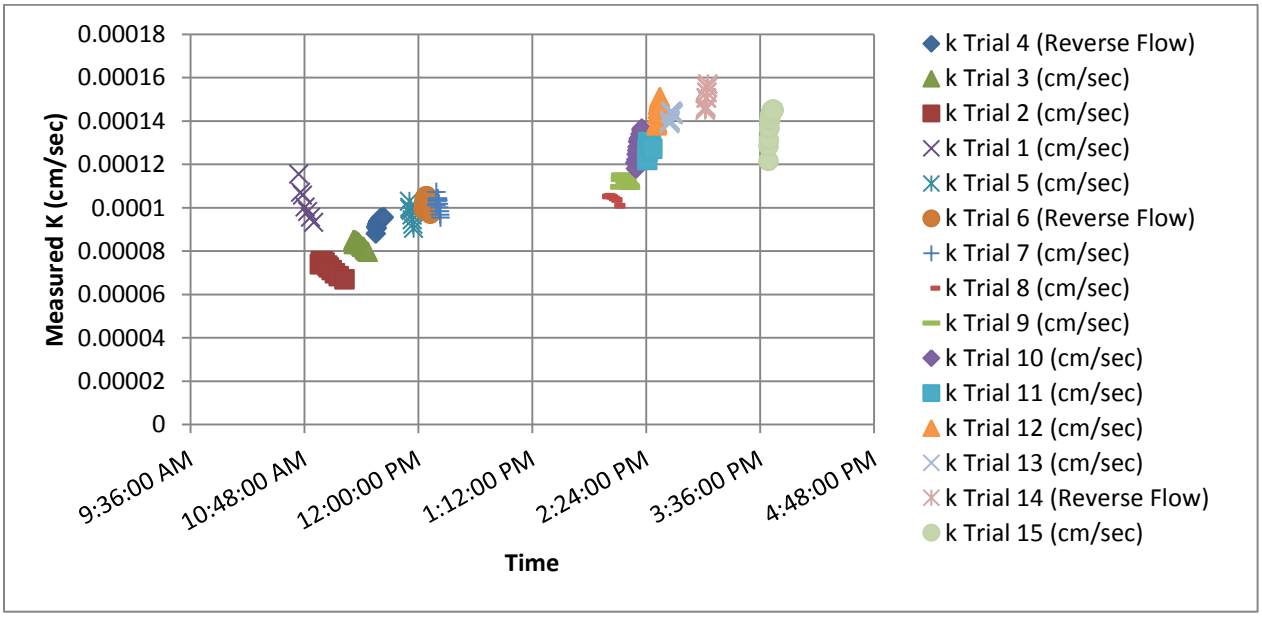

Figure 3.9: Progressive Saturation of a Core

Table 3.4 shows the best values of the measured hydraulic conductivity from the flexible wall permeameter tests, along with the interpretation of the intrinsic permeability:

Table 3.4: Measured Saturated Hydraulic Conductivities

Rock	Fluid	Measured K [cm/s]	Range [cm/s]	ρ [g/mL]	μ [cP]	k [mD]
BS-A1	Brine	2.08×10^{-4}	1.60 to 2.08×10^{-4}	1.02	0.97	236
BS-A2	Zonyl 9023	1.56×10^{-4}	1.43 to 1.56×10^{-4}	1	1.1	177
BS-B1	SDS	3.18×10^{-4}	2.29 to 3.18×10^{-4}	1	1.1	360
BS-B2	Brine	2.69×10^{-4}	2.04 to 2.69×10^{-4}	1.02	0.97	199
	Light Oil	1.23×10^{-5}	1.07 to 1.23×10^{-5}	0.84	42	638

Because these measurements were performed on separate cores, it is likely that the intrinsic permeability of the samples is indeed somewhat different, even with the same wetting fluid. It is also known that the relative ionic strength of the wetting fluid has a large effect on swelling clay minerals. This may be a contributing factor in these measurements, especially in core BS-B2, in which the permeability increased by a factor of 3 when changed from water wet to oil wet. Generally, the flexible wall tests confirm within a factor of 3 that the rock can be described by the relationship $K = \frac{k\rho g}{\mu}$, but the possibility of non-complete saturation in the water-wet cores and the lack of direct measurements on the activity of the clay minerals in these samples prohibits any better accuracy in the comparison.

Chapter 4: Equipment and Testing Procedures

This chapter outlines the equipment and procedures used to measure transient outflows from the rock samples in this testing series. Samples were placed in a core holder inside the centrifuge, which was outfitted with a high resolution, in-flight camera system capable of capturing images of the outflow volume every few seconds. A simple automatic image analysis routine converted the photographs to a measurement of the transient outflow volume with time. Additional measurements of the final saturation distribution were conducted in an X-Ray Computed Tomography scanner after centrifuging for several of the experimental runs.

4.1 Centrifuge System

The large permeameter centrifuge at the University of Texas at Austin was used as the platform for these transient experiments. This centrifuge has the capability to reach 875 RPM with a maximum radius of 0.7m, which is equivalent to approximately 600 g's of acceleration. Due to limitations in some of the current equipment on board, this test series only reached a maximum speed of 415 RPM and used a radius of only 0.5m, roughly equivalent to 100 g's of acceleration at the sample mid-height. Core samples are placed inside the core holders, and the centrifugal acceleration of the fluid relative to the core causes the fluid to flow along the length of the core in a 1-dimensional flow. Swinging buckets in the permeameter centrifuge allow the forcing gradient to always be aligned with the core, which also allows testing on unconsolidated porous media.

The core holders (described subsequently) were adapted for use in the swinging buckets by means of a bearing plate and collar (Figure 4.1).

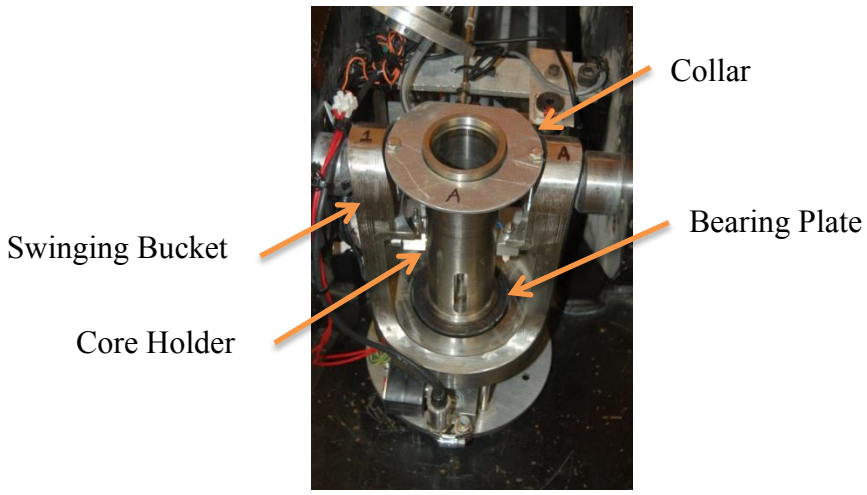

Figure 4.1: Swinging Bucket with Core Holder Mount

The core holders were placed such that the outflow chamber was directly in line with the camera system described in Section 4.1.2, so that high resolution images of the outflow level could be recorded throughout the experiment.

4.1.1 Core Holders

The centrifuge core holder system used in this study was previously developed in the Petroleum department at the University of Texas at Austin. The basic design involves a steel-walled chamber with a clear quartz cup that collects the outflow (Figure 4.2a). The rubber sleeve pictured in Figure 4.2b isolates the core from the overburden pressure chamber, and rubber O-rings isolate the overburden pressure chamber from the outflow cup, giving the system independent control of the overburden pressure and the mean pore fluid pressure. Images of the gas-liquid interface in the outflow chamber are taken through the quartz viewing window.

The outflow endcap for the rock specimen consists of a steel disc with radial and concentric channels carved into it to facilitate uniform drainage from the core. This disc has a thin diameter tube fused to the center, which passes through a variable number of rubber spacers depending on the length of the core, and then through a removable steel

cylinder which isolates the outflow chamber from the overburden pressure chamber as seen in Figure 4.2 c.

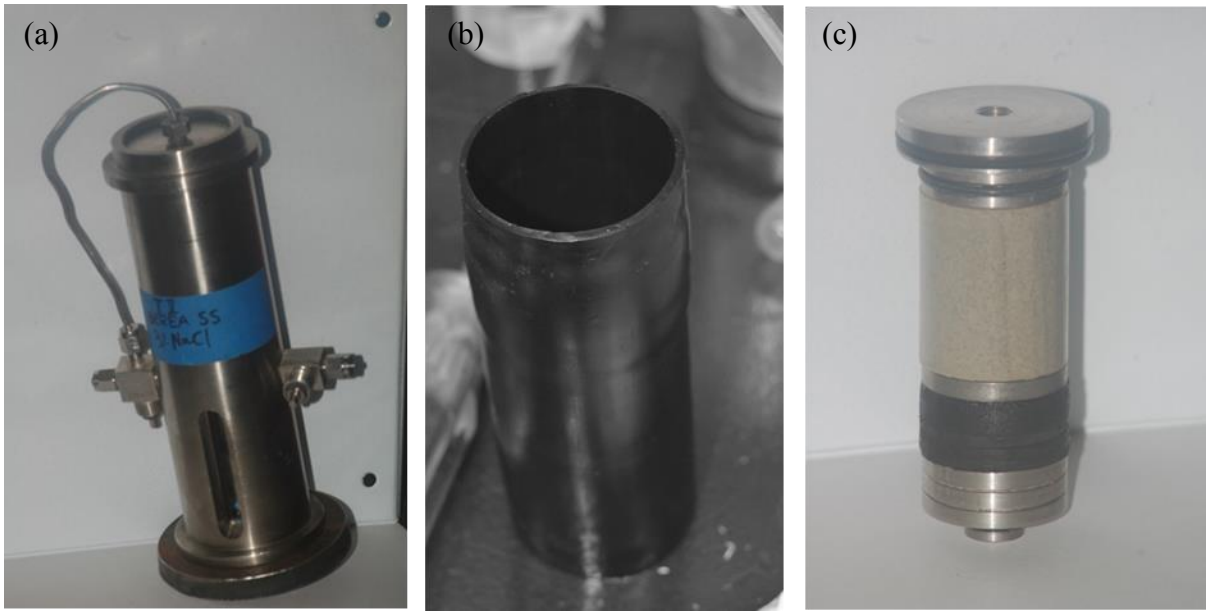

Figure 4.2 General Aspects of the Core Holder: (a) Fully Assembled Pressure Vessel (b) Rubber Sleeve (c) Endcaps

4.1.2 Camera System

The camera system consists of two GoPro Hero4 cameras mounted to the flying buckets of the permeameter centrifuge, and controlled remotely to record the transient data. On-board lighting provides a steady light source to minimize differences between images during a given test. Details of this system are provided next.

4.1.2.1 Mechanical Support

The camera system is attached to the flying buckets in the permeameter centrifuge, and is supported by steel rods threaded into the holes on the side of the bucket used by the HDU mounting plate in the original centrifuge design (Zornberg & McCartney, 2010). The centrifugal force of the cameras is carried by a 3D-printed ABS plastic case bolted to an aluminum plate, which is in turn supported by the threaded rods. These rods have a

support at the mid-span which bears on the rim of the flying bucket to prevent excessive bending deflections in the rods (Figure 4.3).

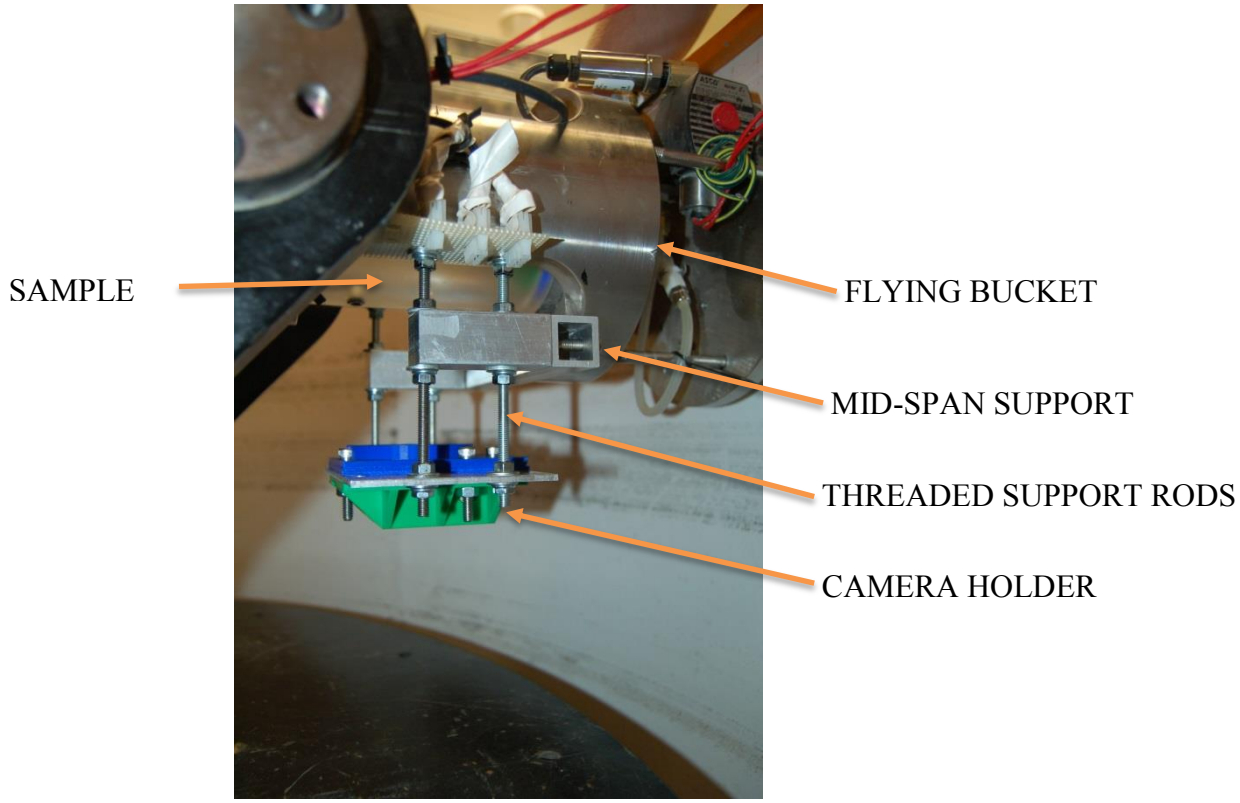

Figure 4.3: Mechanical Support for Camera System

Two critical aspects of the camera mount design were the strength of the plastic casing and the flexural rigidity of the threaded rods holding the camera mount plate. The 3D printed material is an ABS thermoplastic polymer with a melting point of approximately 200 °C. While the centrifuge temperature is well below the material melting point, the possibility of creep failure or fracture is more of a concern. Simplistically, if the centrifuge operating temperature is low enough, then the material should not creep significantly. The centrifuge operating temperature is typically in the range of 22-32 °C, indicating that the body of the camera case is safe from a temperature standpoint. The

camera itself also generates heat because of its power configuration. Also because the ABS plastic is a thermal insulator, the internal temperature of the plastic case did occasionally exceed the operating limits of the camera. However, the temperature still did not become high enough to cause excessive creep in the plastic. An updated version of the camera mounting case was constructed, which uses an aluminum plate as a heat sink on the back instead of the full plastic body, to reduce the internal temperature and protect the camera. Additionally, because the plastic is a printed material, the structure is composed of strands of more strongly bonded chains with weaker links between strands. This could be a concern at higher stress levels, as the camera casing has some more weakly bonded portions which could fail in a more brittle manner under high loads.
The flexural rigidity of the threaded rods was also a concern during the design of the camera system. Simple cantilevered beam analyses with a pin connection at the mid-span along with several detailed finite element body models revealed that the system is stiff enough at moderate g-levels. Additionally, during the development stage, several live centrifuge trials were performed using dummy weights in place of the cameras to prove the carrying capacity of the mounting cases and the rigidity of the rods.

4.1.2.2 Cameras

The two cameras are the GoPro HERO 4 Black edition each with an auxiliary glass lens to decrease the focal distance to a range of 2-12” instead of the typical 12” minimum. The cameras are placed as close to the samples as possible to provide maximum resolution within the image target and to minimize bending moments on the threaded support rods. Power is provided from the internal battery, with continual charging via the mini-USB port on the side of the camera. The two data pins on the USB cable are disabled to prevent the camera from connecting directly to the flight PC, which in the current GoPro firmware would stop any further data collection as it connected to the mother computer. A later power configuration involved a battery eliminator cable which connects to the port on the back of the camera to eliminate any additional heat from the constantly charging batteries. Because the cameras automatically stop recording once

physically connected to a PC, the cameras must be operated remotely using a LabVIEW VI which controls image capture and retrieval over the wireless network hosted by the GoPro camera Remote Application. Images are captured at 5 or 7 megapixels and returned over the wireless network to the solid state disk on the centrifuge PC. From there the images are retrieved via the high speed fiber optic rotary joint for processing on a personal laptop. Because the images are downloaded from the cameras via the wireless network, there is a small chance that the information contained in the image file may become garbled during transmission, producing false images. Typically the attrition rate is on the order of about 3 images out of every 1000. This does not significantly affect any transient measurement as the rate of occurrence is so small compared to the number of readings in a typical test.

Fluid levels in the outflow chamber are tracked by a series of images recorded throughout the test. Typical data recording rates resulted in about 1,000 images per test.

4.1.2.3 Lighting System

The lighting system was developed using a series of LED strips mounted to the centrifuge permeameter table so as to travel with the sample and preserve the same quality of lighting throughout the test. The lights are powered through one channel on the slip ring stack routed through the USR channel. Protection of the LED strips is accomplished by a clear PVC shell bolted over the lights and supported against centrifugal loads at the mid-span by two hose clamps. This prevents the LED strips from detaching from the aluminum rail in flight, and protects them from accidental contact with water. A thin space beneath the aluminum rail allows some air circulation beneath the lights, which helps to prevent them overheating in flight.

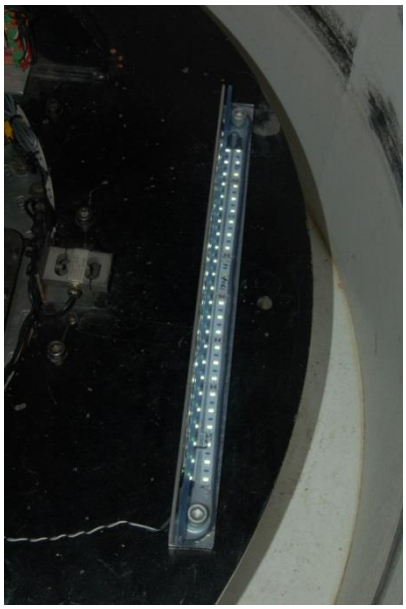

Figure 4.4: Centrifuge Lighting System

4.1.3 Image Analysis and Calibration

Images from the test were reduced to outflow data using a pixel counting algorithm developed specifically for this camera - outflow chamber combination. The average fluid level computed from several lines of pixels was taken to increase the reliability of the measurement. Calibrations from the fluid level to real fluid volume were performed using a series of images and the simultaneously measured mass of the outflow chamber.

4.1.3.1: Image Analysis Algorithm

Fluid levels throughout the test are tracked using an algorithm which runs through the entire set of images and, for a given zone of interest, finds the first major change from dark color to light color within a vertical band of pixels. For transparent fluids, this technique relies on the difference in refractive indexes between the two fluids, which results in a different background object being visible to the camera above the meniscus than is visible below the meniscus as seen in Figure 4.5.

Figure 4.5: Light Intensity Contrast within Viewing Window

This creates a dark zone and a light zone on the edge of the quartz viewing window, which is an easily recognizable feature for the image processing algorithm to track. The meniscus itself can be enhanced by floating a dark plastic disc on the surface of the water. For opaque fluids, this technique would work more generally, regardless of the refractive index of the two fluids as long as a significant color difference existed between the two fluids.

The zone of interest is chosen manually in the first image, and changes in fluid level are computed for the remaining images as illustrated in Figure 4.6

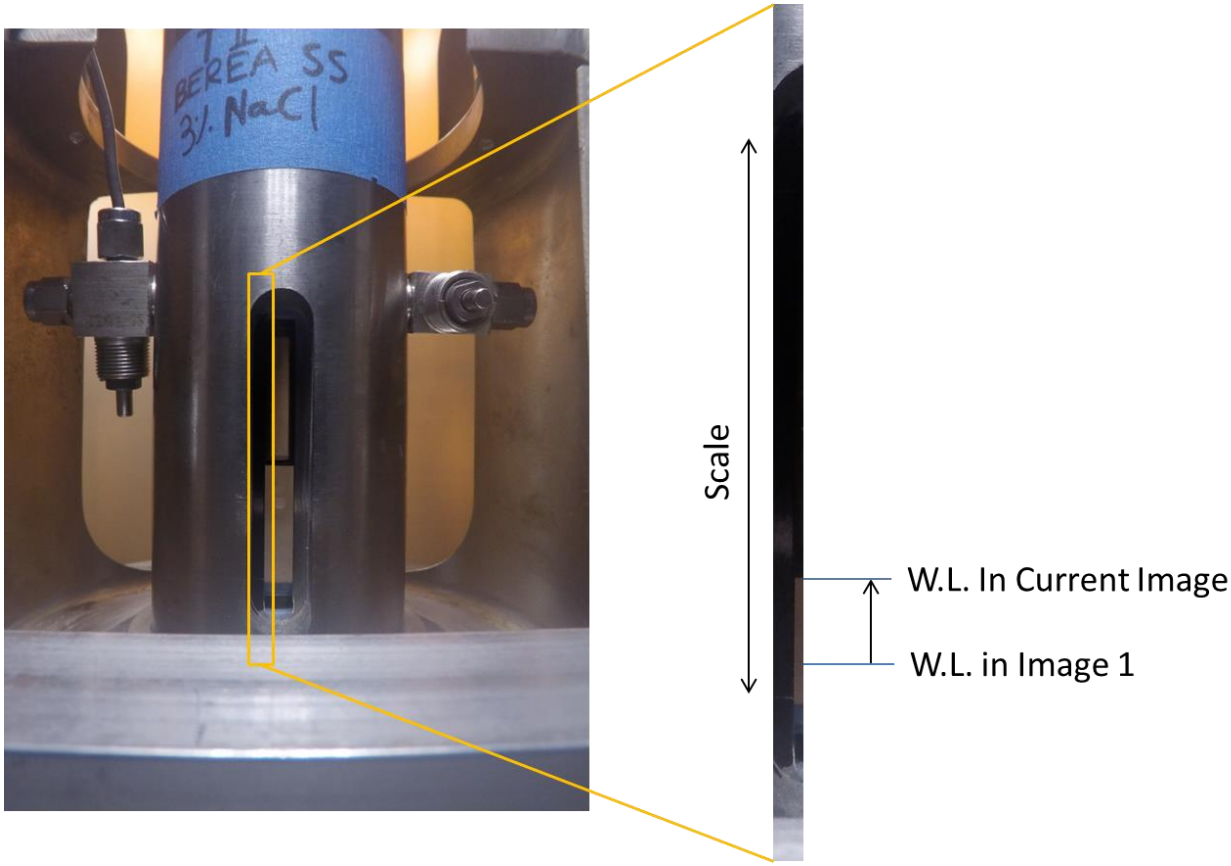

Figure 4.6: Conceptual Computation of Fluid Level

More specifically, the algorithm computes, for each line of pixels, the change in overall light intensity (defined as the sum of the RGB channels for each pixel) between each pixel and its lower neighbor; in essence a derivative of the recorded light intensity. Depending on the clarity of the image and the quality of the lighting, the biggest change in intensity is likely to occur when the fluid type changes, due to the effect of the refractive index upon the visible background, rendered in Figure 4.7.

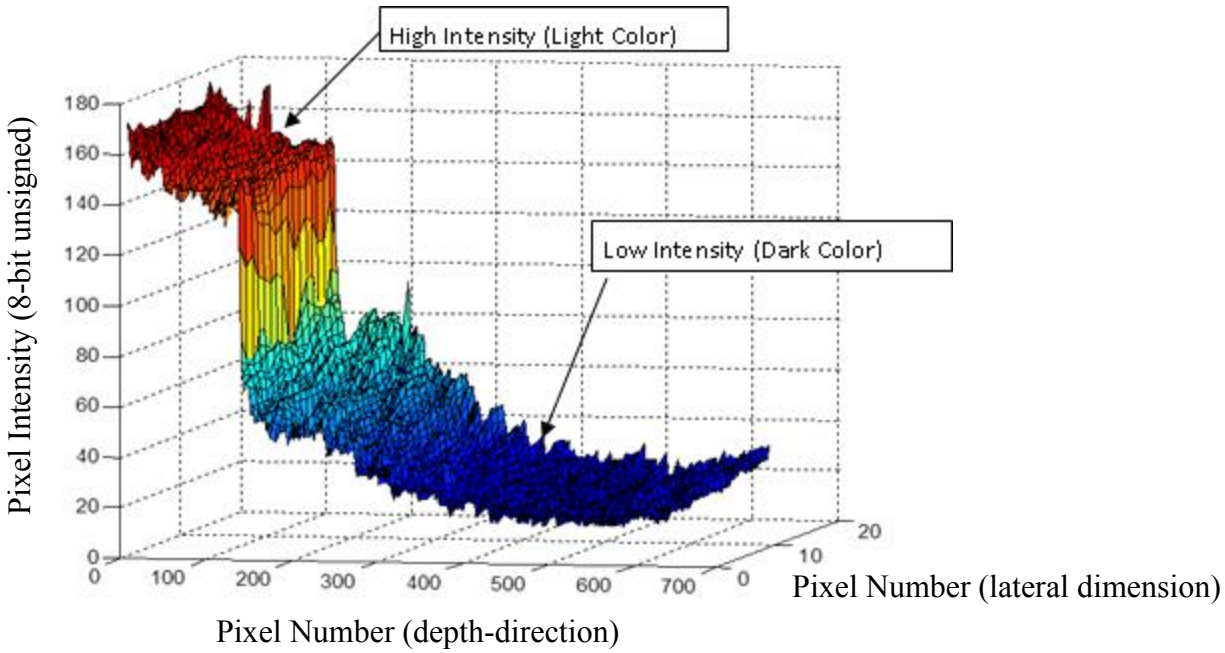

Figure 4.7: Light Intensity Pixel Values

The algorithm then computes the mode of the distance, in pixels, from the bottom of the image to where this maximum change takes place, and then for a search band of ± 5 pixels, computes the average location of the maximum change in light intensity for all selected lines of pixels. This extra step is necessary to eliminate some of the spurious results from messy images with random reflections of bright light, as illustrated in Figure 4.8.

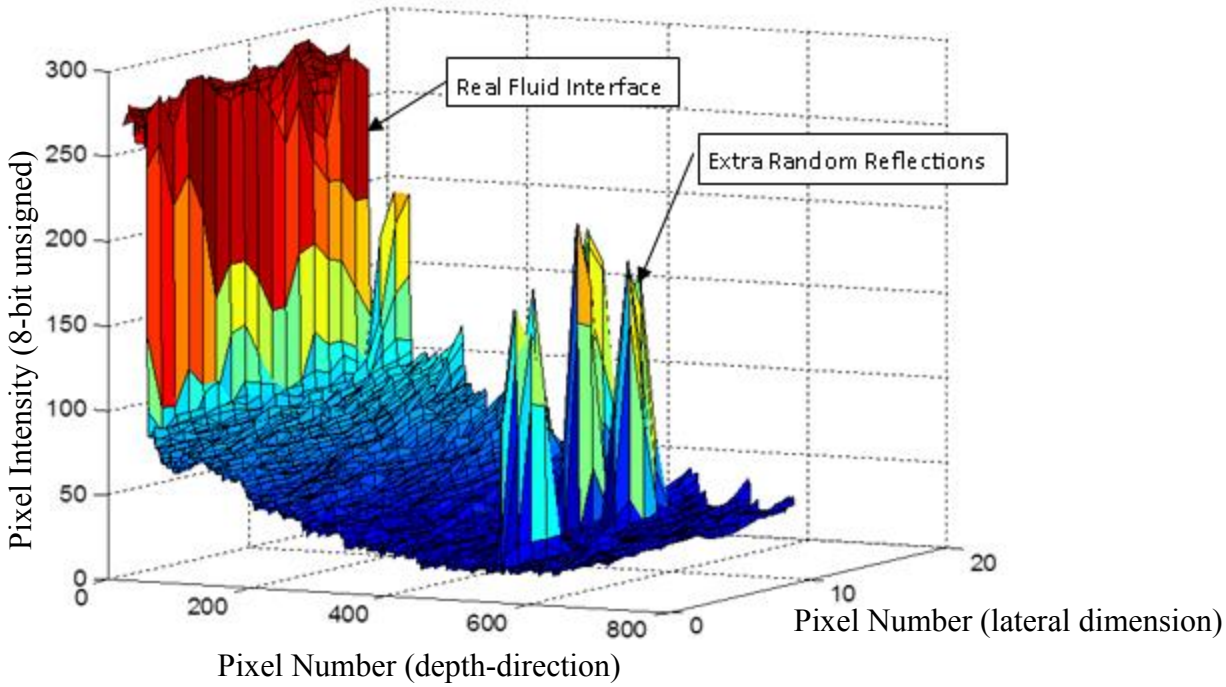

Figure 4.8: Pixel Intensities in a Messy Image

The resulting number is the distance in pixels from the bottom of the image to the fluid interface. The outflow chamber must be primed with a small amount of the draining fluid so that the fluid outflow can be computed as a change in the position of the meniscus, rather than as an absolute position of the meniscus.

A sample set of measurements interpreted using this algorithm is presented in Figure 4.9:

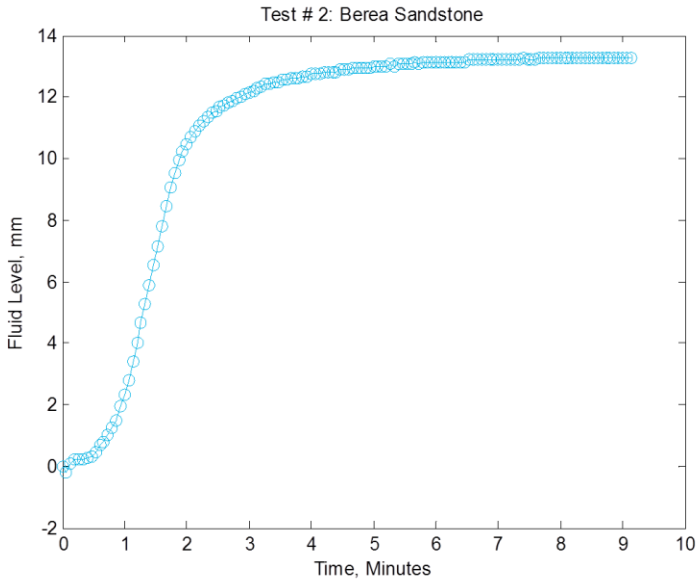

Figure 4.9 Sample Outflow Measurements

4.1.3.2 Image Calibration

The volume in the outflow chamber must be calibrated to the fluid level, and the physical distance in the images must be calibrated to the pixel count. To calibrate the pixel count against the physical distance in the images, two thin light-colored marks were etched into the steel flange next to the viewing window using a pair of calipers. The marks are visible in most of the images (Figure 4.10), and give the scaling factor between the physical distance and the number of pixels.

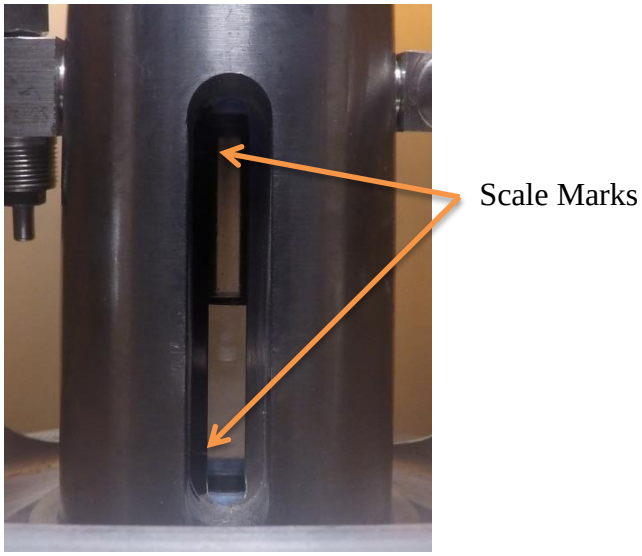

Figure 4.10: Placement of Physical Scaling Points

This allows the position of the camera to be changed depending on the exact requirements of any given test, but preserves the space calibration regardless of the camera position. The second calibration necessary is for linearity of the image with respect to physical space. By measuring the weight of the core holder while filling the outflow chamber in many small stages and recording images at each fluid level, a calibration is obtained both for the cross-sectional area of the outflow chamber, and for the linearity of the images over the range of interest. As seen in Figure 4.11, the calibration is very linear within the center of the photograph where this calibration was made. The slope of this calibration corresponds to the area of the outflow chamber, and any deviation from the slope corresponds either to a change in the area of the outflow chamber or a non-linearity in the image. The outflow chamber is machined in such a way, however, that it is highly likely that deviations from linearity are more due to the image rather than to the lack of precision in the outflow chamber.

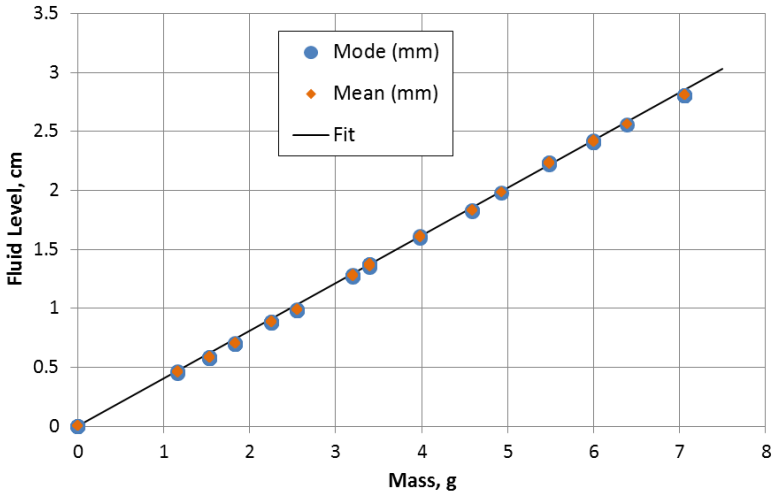

Figure 4.11: Outflow Chamber Calibration

4.1.4 Transient Test Procedures

Two classes of transient centrifuge tests were run in this testing program. Both classes were used for drainage of the wetting fluid only. In the single stage tests, the speed is increased from rest to the maximum value (100 g's) in a single stage to attempt to foster a plug drainage environment. In the multi-stage tests, the centrifuge speed is stepped up by smaller increments and held constant for a number of hours before increasing the speed again. This type of test generates a reasonable approximation to the drainage capillary pressure curve, while often taking somewhat longer time to execute. Figure 4.12 shows typical results from each type of test:

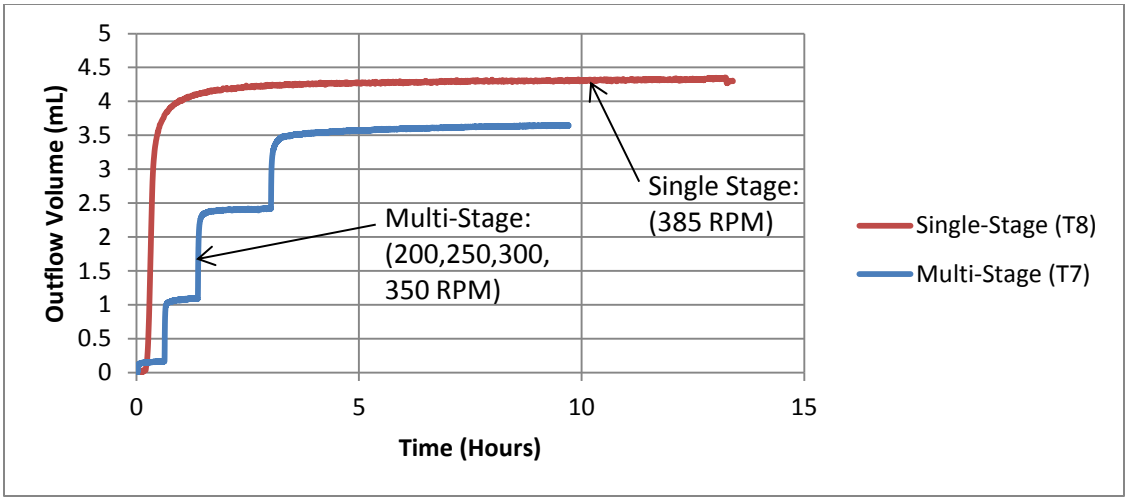

Figure 4.12: Example Test Results

The data sampling rate in these tests was designed so that recording frequency would roughly match the flow rate. Images were captured as often as once every 10-15 seconds for the beginning of each centrifuge speed step, down to as few as one image every 10 minutes during the late times of each step, as shown in Table 4.1. The reading schedule was restarted each time the centrifuge speed was increased to provide a high measurement frequency when the most flow was occurring.

Table 4.1: Typical Reading Schedule

Order	Time Between Readings	# of Readings
1	10-15 seconds	100
2	30 seconds	100
3	60 seconds	200
4	10 minutes	Up to 1000

4.2 X-Ray Computed Tomography (CT Scanning)

X-Ray Computed Tomography was used in this investigation to measure the local fluid distribution within the sample soon after completion of a centrifuge test. Computed

tomography involves inferring the mass density along a line through the sample based on the X-Ray attenuation at that orientation. The source and receiver are then rotated about the sample, and the density of each measured line is inverted with respect to the orientation of the X-Ray sensor to obtain the average density within a given number of zones within the sample. The result is an array of pixels whose intensity represents the average mass density within the representative volume. The intensities are reported in Hounsfield units, such that air has a CT number of -1000 while water has a CT number of 0. Figure 4.13 shows the complete results of one "slice" presented as an image (including the plastic stage and the cardboard support structure beneath the core). Larger pixel intensities are shown as lighter colors and correspond to denser material.

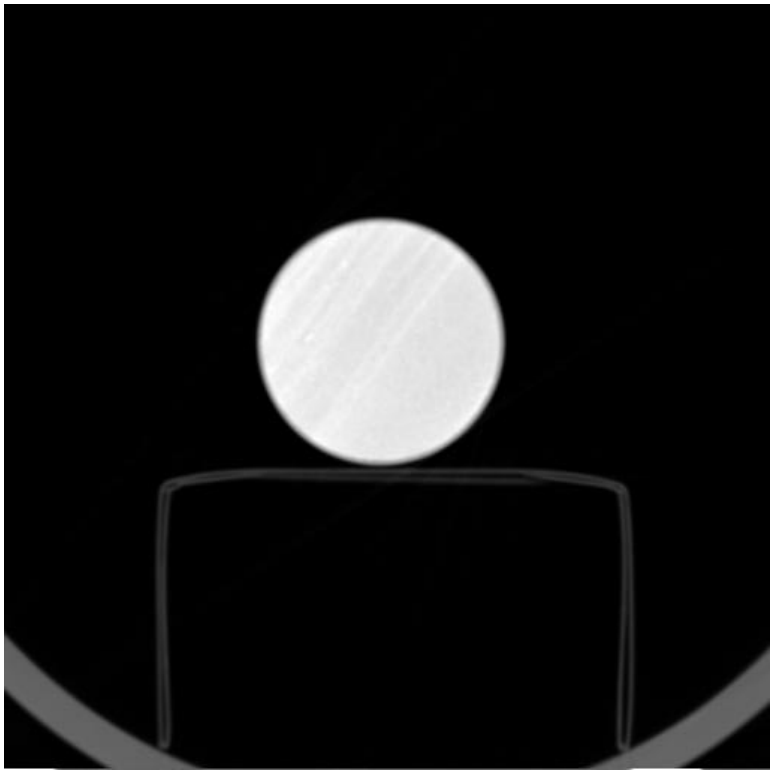

Figure 4.13: X-Ray CT Slice

The X-Ray attenuation is linearly proportional to the mass density along its path, so the degree of wetting fluid saturation after a test can be inferred from the difference in mass density at any location along the core between a saturated state and a dry state. The

process is calibrated by scanning the sample both in an oven-dry state and in a fully saturated state, as shown in Figure 4.14.

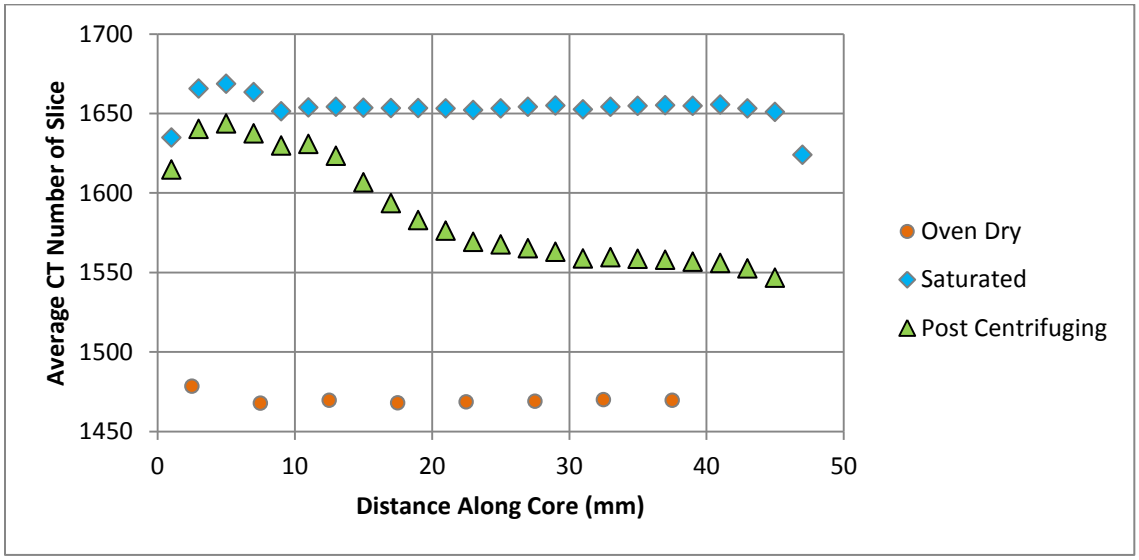

Figure 4.14: CT Calibration Scans and Sample Results

The fluid saturation is interpreted by linearly interpolating the measured mass densities after centrifuging between those measured in the fully saturated and oven-dry states. Having determined a reasonable degree of saturation, the appropriate suction is interpreted as the applied suction in the previous stage of centrifuge testing, varying from zero at the outflow end to a maximum at the top of the core, and thus the CT retention curve is built.

This process is applicable to centrifuge testing with a few caveats: as the centrifuge spins down, the centrifugal gradient is quickly removed from the equilibrium condition, and the matric suction term now dominates the fluid potential regime inside the core, creating a strong gradient in the reverse direction. Accordingly, the water in the core will redistribute in response to this gradient and the measured degrees of saturation in the CT will be more uniform than those expected under centrifugal conditions. Based on the interplay between the wetting fluid saturation and the hydraulic conductivity, we expect that this will especially be the case right at the outflow end of the sample, where the suction gradient is the same, but the conductivity is orders of magnitude larger than that

in the rest of the sample. The redistribution of fluid also results in some relaxation of the suction gradient in the sample, so not only will the measured saturations be too uniform, but also the assumed suctions along the core will encompass too broad of a range. Even with the best time-management procedures, the shortest time between beginning the spin-down process and starting the first scan in the CT was on the order of 10 minutes, so it seems likely that any real precision in the measured saturation at the outflow end was lost during this time. Cores were scanned repeatedly once placed in the CT to allow the remaining fluid redistribution to be imaged. Fluid saturations did continue to redistribute throughout the whole series of scans, which was typically limited to 30 minutes or less of total observation time. While the CT process post-centrifuging was useful to observe a reasonable estimate of the non-uniform saturation field within the sample interior, the ends of the specimen were very difficult to scan with precision because a slight difference in placement of the core on the stage can change the measured density from that of rock to that of air. Consequently, any scan within about 2 mm of either end is not expected to provide any reliable information about the degree of saturation.

One additional source of measurement error may be that the CT scanner internal calibration can change slightly between any of the scans used in the saturation calibration. Even between scans performed just minutes apart on the oven-dry samples, the CT results varied slightly but noticeably. Finally, the measurement of saturation depends highly on the quality of initial core preparation, whether the core was actually completely saturated or completely dry during the calibration scans.

Thus, the CT measurements themselves are subject to their own set of uncertainties simply because the sample was removed from the centrifugal environment in order to take the measurement. Fortunately, if the degree of saturation is low enough at the top of the core, the hydraulic conductivity is also vastly reduced, so the amount of fluid redistribution may be small enough to still provide some good information about the saturation distribution during the test, especially in the high suction range.

Chapter 5: Experimental Results

This chapter presents the results obtained from the centrifuge testing program and the subsequent CT scanning to determine fluid saturations after spinning. Second to the image analysis, the transient outflow curve is considered the most basic form of the centrifuge data. Several representative centrifuge time histories from the Berea Sandstone are included in this chapter, while the remaining time histories for analysis are provided in Chapter 6. The results of the X-Ray Computed Tomography program are also included in this section.

5.1 TESTING SCOPE

The scope of this testing program included several transient outflow experiments. In some select tests, CT scans were run on the samples after centrifuging had been completed. Table 5.1 shows a summary of the relevant parameters of the centrifuge tests.

Table 5.1: Scope of Centrifuge Testing Program

Test ID	Core ID	Wetting Fluid	$S_{initial}$ <95%	Speed (RPM)	r_o (m)	CT
T1	BS_A1	Brine		385	0.5475	
T2	BS_A2	Brine		385	0.5475	
T3	BS_A1	Brine	Y	385	0.5475	
T4	BS_A2	Brine	Y	385	0.5475	
T5	BS_B1	Brine	Y	200-385	0.5475	
T6	BS_B2	Brine		385	0.5475	
T7	BS_A1	Brine		200-350	0.5475	
T8	BS_B1	Brine		385	0.5434	
T9	BS_B2	Brine		300-385	0.5434	
T10	BS_A2	Brine		100-385	0.5434	
T11	BS_A2	Brine		385	0.5434	
T12	BS_B2	Brine		385	0.5475	Y
T13 (a)	BS_A1	Brine		850	0.2265	Y
T13 (b)	BS_B1	Brine		850	0.2265	Y
T14	BS_A2	SDS		50-385	0.5467	
T15	BS_B1	SDS		260	0.5467	Y
T16	BS_A1	Brine		385	0.5475	Y
T17	BS_A2	SDS		100-385	0.5374	
T18 (a)	BS_B2	Brine		150-415	0.5475	
T18 (b)	BS_A2	Zonyl		150-415	0.5475	
T19 (a)	BS_A2	Zonyl		100-380	0.5428	
T19 (b)	BS_B2	Light Oil		100-380	0.5414	

5.2 CENTRIFUGE OUTFLOW CURVES

Transient Outflow curves were measured in the centrifuge using the imaging system described previously in Chapter 4. Several of these curves are reproduced in Figure 5.1 in the form of the average wetting fluid saturation vs. time:

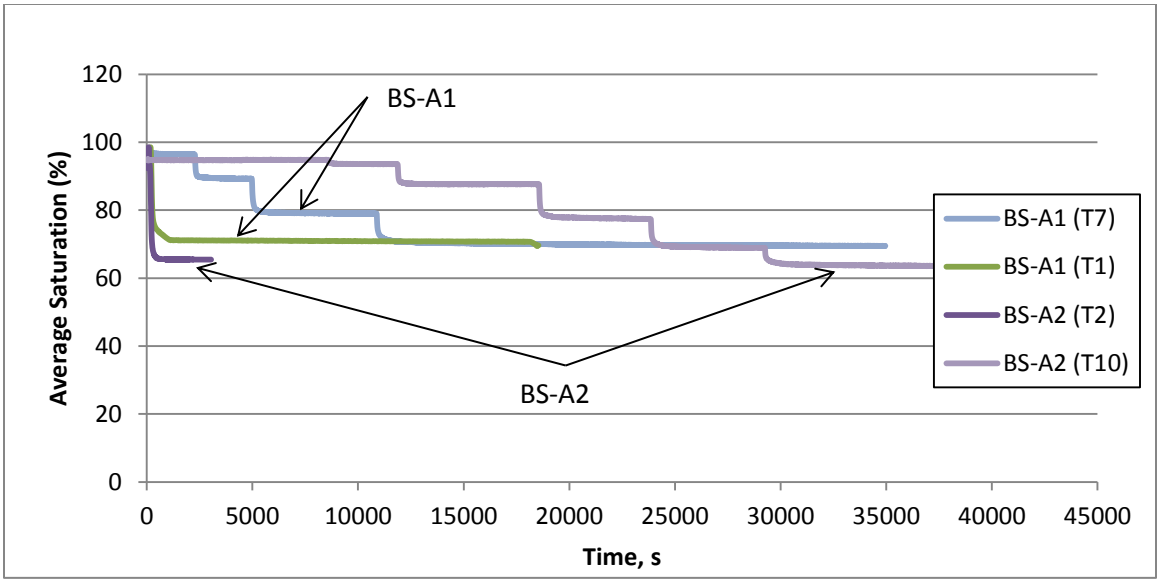

Figure 5.1: Centrifuge Outflow Curves

These particular curves correspond to Tests 1, 2, 7, and 10 on Cores A1 and A2 using 3% NaCl brine as the wetting fluid and air as the replacing fluid. These tests all ended at the same rotational speed, namely 385 RPM, corresponding to approximately 90 g's at the sample mid-height. The curves from each core line up at late times toward the end of each test, which shows that the centrifuge drainage process produces fairly repeatable results for a given core, even if the starting saturation is slightly different. Additionally, the slope of the outflow curves tends to asymptotically approach a singular value of average saturation, so the test results do visually appear to be reaching a state of equilibrium at each centrifuge speed.

For later use in fitting the transient flow solution to Richards' equation, it is important to also know the time history in the measured centrifuge speed, so measurements were taken with a load-cell mounted on the permeameter table. A set of these measurements, along with the recorded outflow from both cores in that centrifuge test, are shown in Figure 5.2:

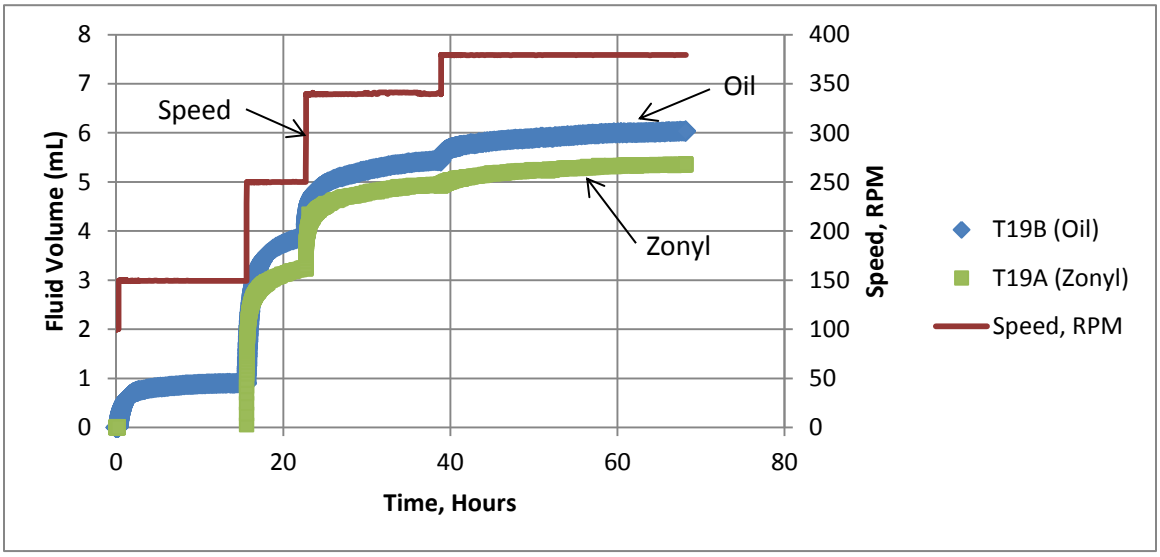

Figure 5.2: Outflow Curves and Recorded Rotational Speed for T19 (Oil & Zonyl)

Generally, as seen in Figure 5.2, the fluid outflow responds to the increased centrifugal force within about one minute of increasing the speed. Additionally, the measured centrifuge speed is quite stable over the course of the experiment.

The results of a single speed test, T15, are included in Figure 5.3:

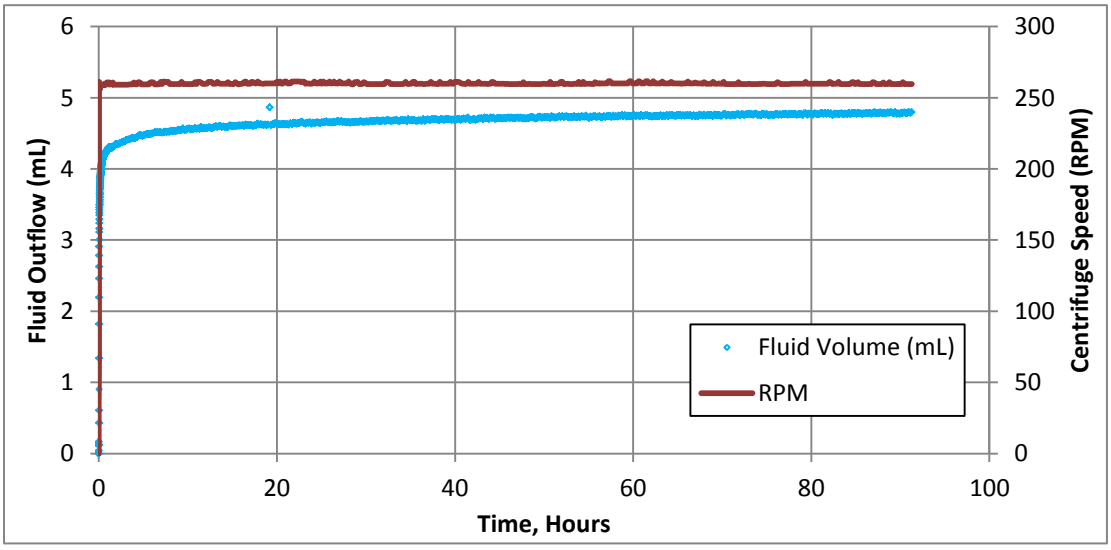

Figure 5.3: Outflow Curves for Test T15 (SDS)

As shown in Figure 5.3, the slope of the outflow curve is still non-zero even after 90 hours of centrifuging. The slope of the outflow does continuously decrease throughout the experiment to asymptotically approach a single value of the total outflow volume. Again, the centrifuge speed is quite stable over the course of the entire experiment. One measured data point in the T15 series is noticeably higher than the rest of the time history. This point corresponds to one of the garbled images referred to in Section 4.1.2.2, in which several rows of pixels were transmitted in the wrong order, displacing the observed fluid level upward by a significant amount.

5.3 VERIFICATION OF OUTFLOW VALUES

The cores were weighed at the end of each test, to provide another value of the degree of wetting fluid saturation at the end of the test. Figure 5.4 shows the difference between the outflow mass from the image analysis, and the measured change in mass of the core itself for several of the actual tests:

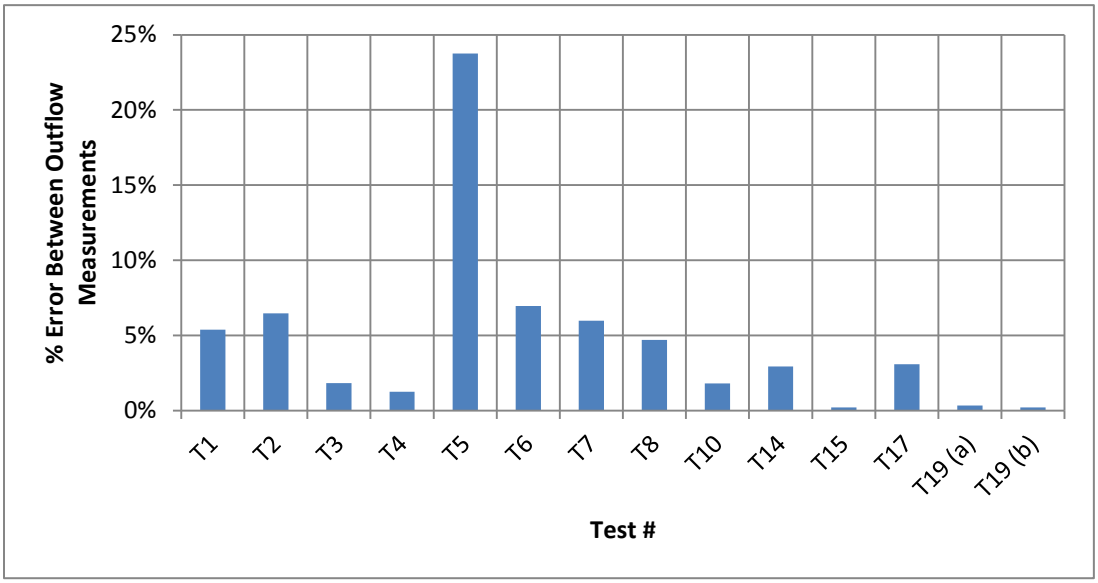

Figure 5.4: Differences between Mass and Image Analysis

The values reported in the figure above do account for the differences in fluid density. While most of the tests do fall under the 5% difference mark, many of the earlier tests show a rather large discrepancy, even as high as 23% as in T5. The shift to consistently

lower errors around T10 reflects a change in the quality of the seal between the rock and the outflow end cap, which reduced the occurrence of leaks. The original seal was dependent on the interface between a piece of stiff heat-shrink plastic tubing and the outflow end cap. However, the slight diameter difference between the rock and end cap created a space which the stiff plastic would bridge, destroying the necessary contact for a proper seal. The membrane was subsequently changed to the more compliant thick rubber membrane pictured in Figure 4.2b, along with several O-rings to ensure full contact between the end cap and the membrane.

5.4 CT SCANS

X-Ray Computed tomography was used to image the sample after spinning in the centrifuge to help validate the moisture profile inside the specimen. The output of the CT scanner is a series of "slices" along the length of the core with a resolution of (mm/pixel) within each slice (Figure 5.5).

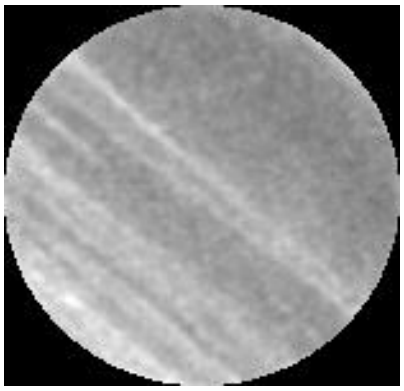

Figure 5.5: X-Ray CT Core Slice

The value in each pixel represents the average mass density of the material within that zone. CT Slices were measured at 5mm thick in the z direction for early tests and at 2mm thick in the z direction for later tests. Because the orientation of the core about its axis was not exactly replicated on the CT stage each time it was scanned, the pixels themselves do not directly correspond to one another in different sets of scans. The average value within any given slice, however, will be the same regardless of the scanning orientation. Hence, the average saturation along the core can be accurately computed by comparing the sets of live scans to the calibration scans. This analysis method does treat the core as a single homogeneous mass rather than as a group of heterogeneous zones within each cross section. This level of detail is appropriate for a comparison with the centrifuge method, which is in itself an average of the true rock behavior.

The process was calibrated in an oven dry state and in a fully saturated state to establish the limits of density that would correspond to a given saturation.

The results of the calibration for core BS-A1 using the Brine as the wetting fluid are shown in Figure 5.6:

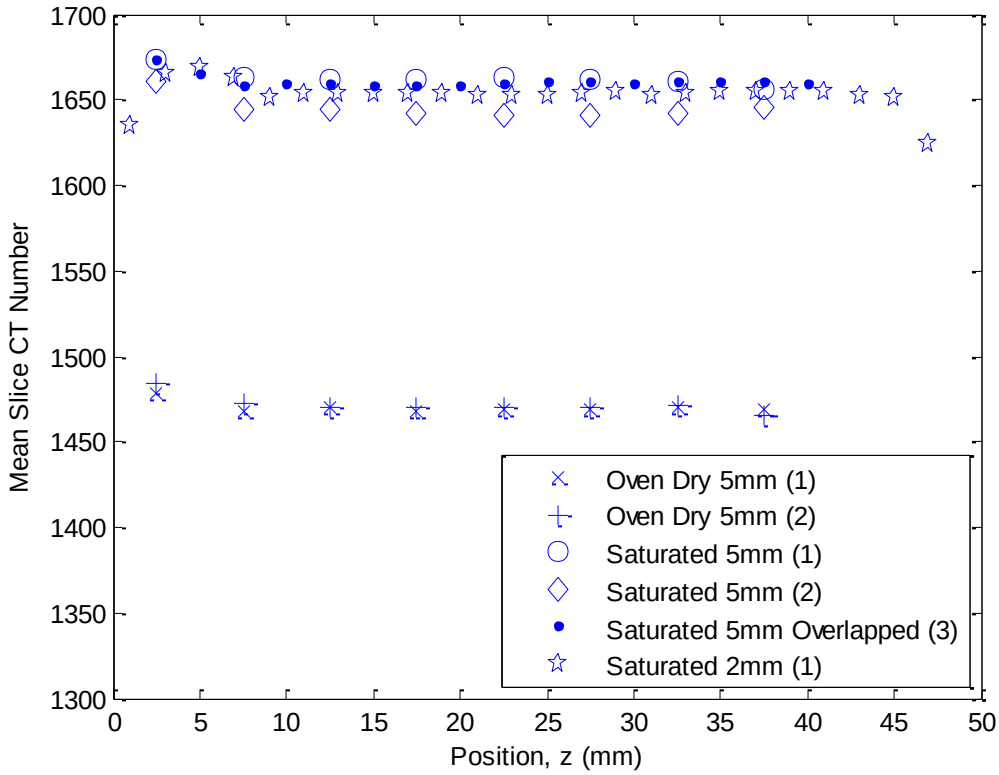

Figure 5.6: Calibration Results for Core BS-A1 (Brine)

As seen in Figure 5.6, some slight variability exists between the measured values in separate scans, even in the oven-dry cores. While this variability is partly due to the CT machine calibration, the mass of the saturated core prior to scanning were measurably different each time, so some of the variability in the saturated scans is likely due to changes in the actual brine saturation during scanning as well. Figure 5.7 shows the results of CT scans performed on Core A1 after centrifuge tests T13 and T16, along with the calibration scans:

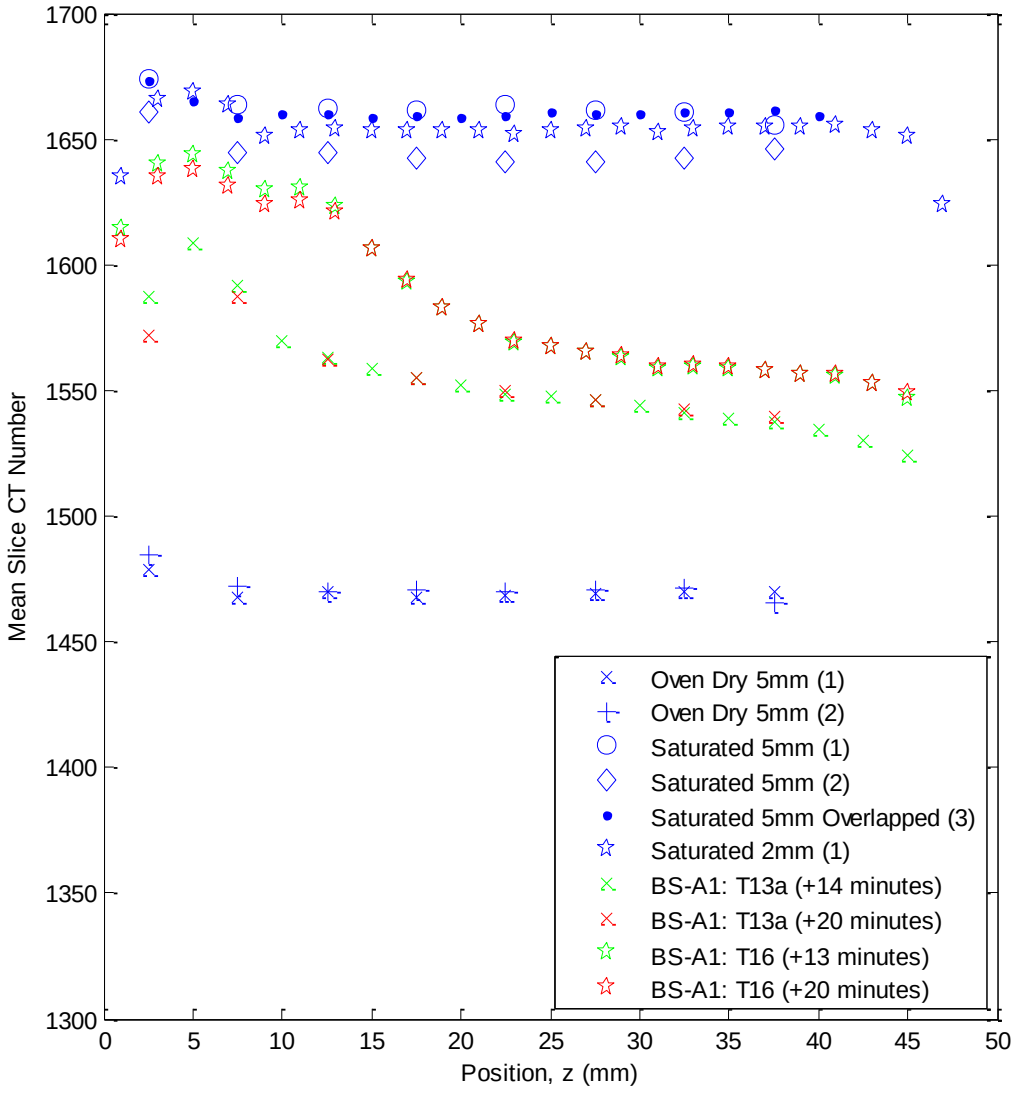

Figure 5.7: CT Scans for BS-A1 after Centrifuging: (T13a & T16)

As seen in Figure 5.7, the fluid inside the core post-centrifuging is roughly distributed according to the matric suction distribution in flight, with the maximum degree of saturation occurring at the outflow end ($z_m = 0$) and the minimum occurring at the top of the core. After stopping the centrifuge and transferring the samples to the CT stage,

repeat scans of the core were performed approximately 15 minutes apart. The measured saturations after centrifuging tended to redistribute slightly during this scanning period, as shown in the data from T13a and T16. This result is expected based on the theoretical matric suction gradient which exists inside the sample to counteract the centrifugal gradient. Once the centrifugal gradient is removed, the matric suction gradient drives the remaining fluid inside the core back toward the top of the core. The measured CT data indicate that the outflow end is only around 90% saturated by the time the measurement can be taken. Because this fluid redistribution begins to occur as soon as the centrifuge begins to slow down and because of the lack of precision in scanning the outflow end, it is not known whether the outflow end actually was at the full saturation while in flight. Another important observation from the post-centrifuging CT data in Tests T13a and T16 is that the zone of maximum saturation does become increasingly compressed toward the outflow end of the core for tests run at higher g-levels, as predicted from the theory. This allows the data to be constructed into an approximate capillary pressure curve as outlined in Section 4.2.

The redistribution of fluid can be observed more noticeably in additional data from Core B2 from the centrifuge test T12. Scans were performed post-centrifuging on this core every four to five minutes once the core had been placed on the CT stage. Additionally, this core was left inside a sealed glass jar in a vertical orientation for approximately one month following this initial set of scans, after which it was scanned again to observe the remaining fluid distribution. These results are reproduced in Figure 5.8:

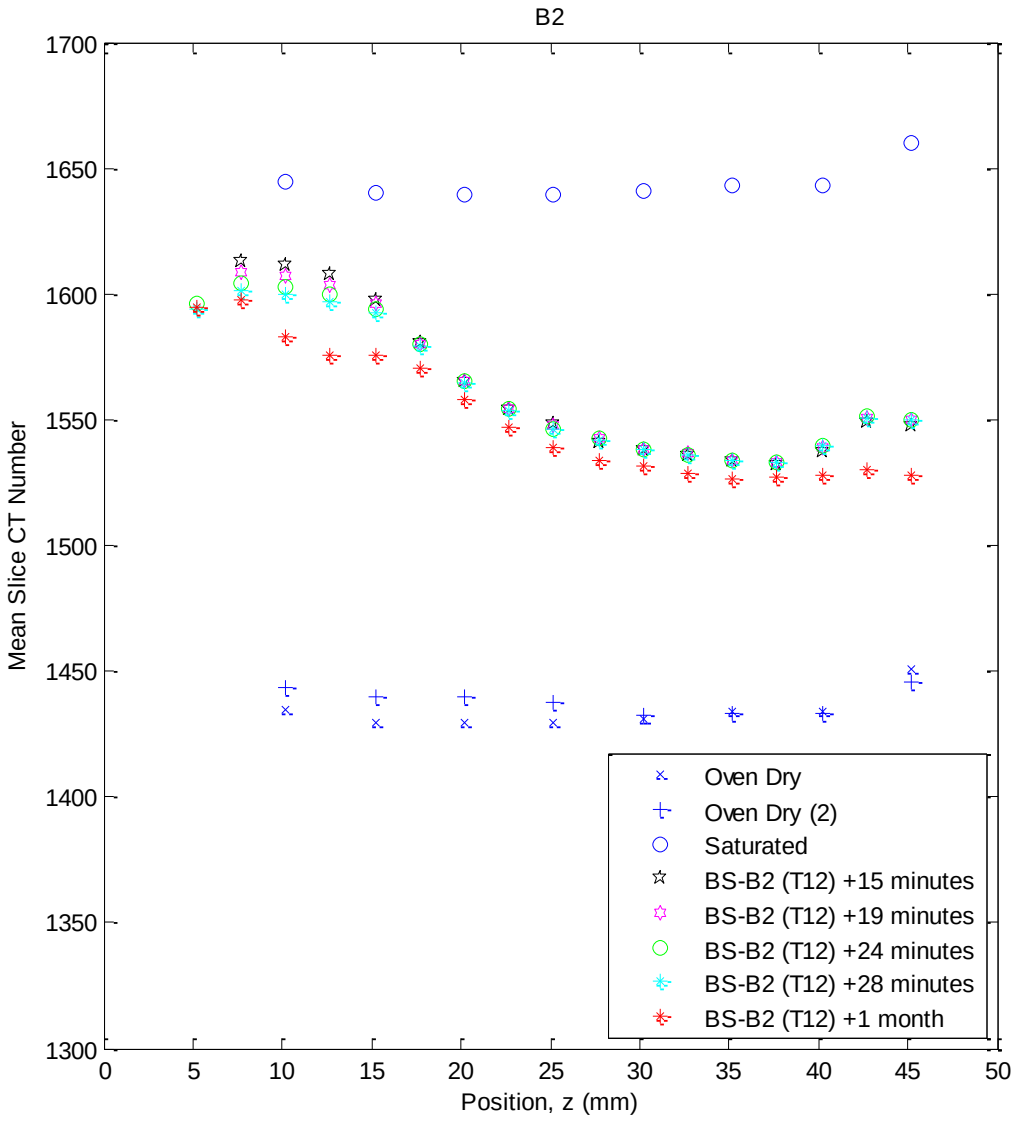

Figure 5.8: CT scan Results for BS-B2 after Centrifuging (T12)

In Figure 5.8 the results from T12 seem to indicate that the core was not at 100% saturation at the outflow end after spinning in the centrifuge. While this may be the case, the scans themselves were conducted using a 5mm beam width, with a displacement index of 2.5mm, implying that every data point fully overlaps with its nearest neighbors. This will tend to smooth out any sharp features in the measured saturation distribution, so

the apparent precision in these scans is higher than it ought to be. Nevertheless, this test illustrates the potential for concerns of desaturation of the outflow end during a transient outflow test. For this reason, it is desirable to perform centrifuge tests which enforce the saturation boundary condition discussed in Section 2.1 rather than the conventional free-flow boundary condition used in this study. Additionally, the results from the core after one month inside the glass jar do show a reasonably similar profile to the earlier results immediately after centrifuging. This is likely due to the fact that the fluid redistribution is itself an imbibition process and tends to require larger matric suctions to replace the gas phase with the liquid phase due to trapping of the gas phase inside of the pores. It appears from this dataset that the ends of the core did lose some fluid to evaporation after one month, likely because the glass jar was not perfectly sealed during that time.

Results from Core BS-B1 are included for T13b in figure 5.9:

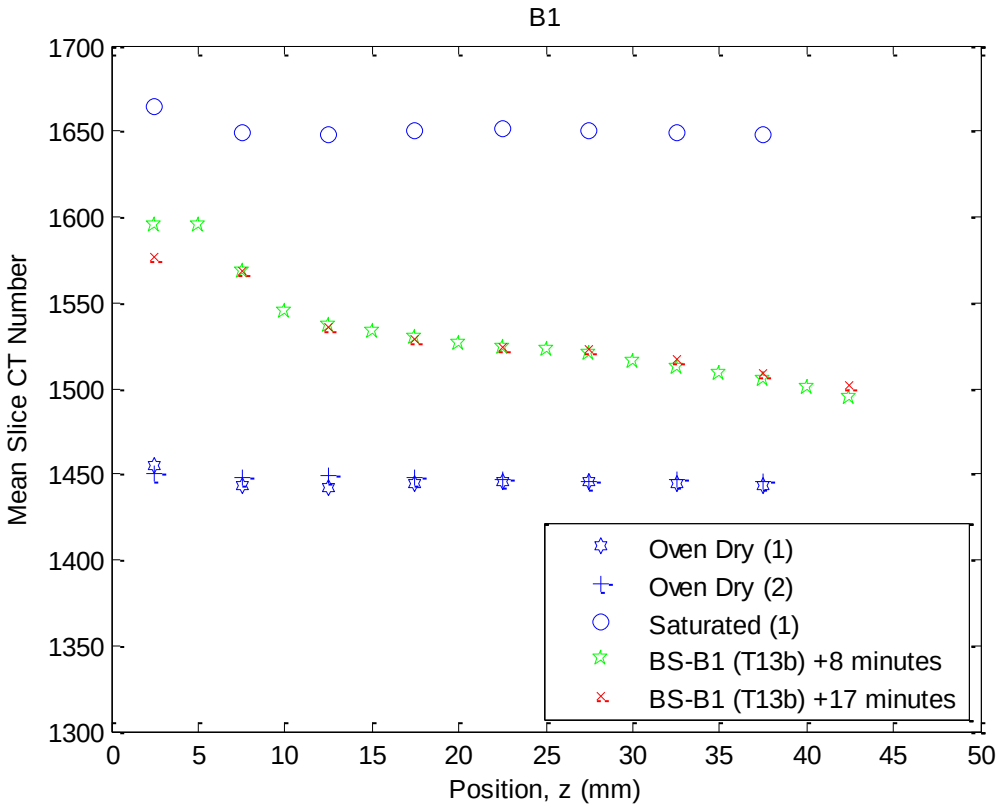

Figure 5.9: CT scan Results for BS-B1 after Centrifuging (T13b)

The data in Figure 5.9 were measured in the same overlapping manner as those in other scans from T12 and T13. For the centrifuge speed used in T13 some concerns do exist about the desaturation of the outflow end based on this data. Again, however, the low resolution in the measured data along with the fluid redistribution during the 8-minute time interval between initiation of the centrifuge spin-down process and the first scan in the CT prevents any robust conclusion about this issue.

Finally, data is presented from Core BS-B1 using the SDS as the liquid phase. The corresponding centrifuge test (T15) was run at a single speed of 260 RPM for nearly 90 hours, after which the core was removed from the centrifuge and scanned. The results from this set of scans are included in Figure 5.10:

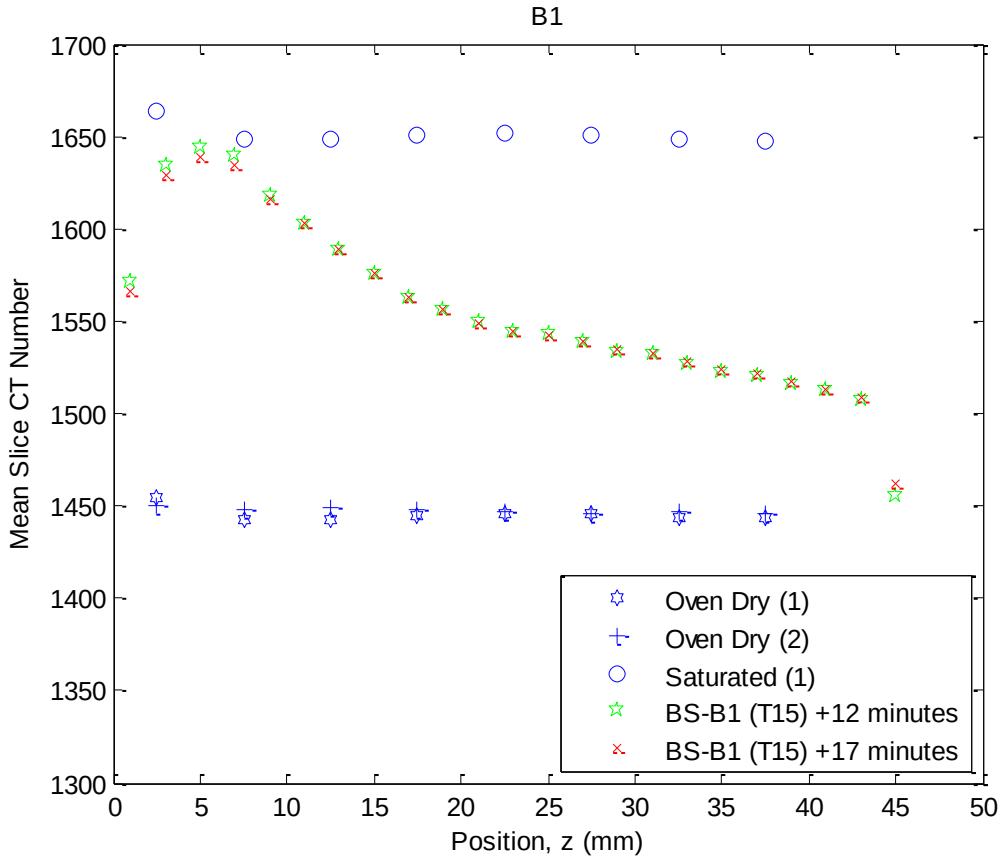

Figure 5.10: CT scan Results for BS-B1 after Centrifuging (T15)

The results presented in Figure 5.10 were measured using a 2mm beam width an index of 2mm. this means that each data point has little to no overlap with either neighbor. Consequently, the precision of the measurement is greater than in those scans from T13 and T12 using a wider X-Ray beam width and overlapping the measurements.

Chapter 6: Analysis

Centrifuge outflow curves are analyzed consistent with the Hassler assumption for the four wetting fluids tested in this study. Capillary pressure (retention) curves are generated from the centrifuge data using an iterative approach. Numerical history matching was performed using an iterative solution of the centrifugal Richards' equation, using Van Genuchten Mualem-type functions, (Van Genuchten, 1980), but using independent parameters to define the hydraulic conductivity and the retention curve. This allows a reasonable set of hydraulic conductivity functions to be derived from the transient centrifuge results. The quality of the history match is sensitive to several inputs, including the initial saturation and the saturated hydraulic conductivity. A comparison is made between history matches using both coupled and independent model parameters from the Van Genuchten Mualem model. A comparison between the hydraulic conductivity derived from Hagoort's method, (Hagoort, 1980) and the full history match is also included.

6.1 Centrifuge Drainage Retention Curves

In this study, we used core holders which did not enforce a saturation boundary condition. Consequently, the estimates of applied potentials during the experiment are less reliable than in other possible experimental setups, but for the low speed levels tested in this study, the assumption of a saturated outflow boundary is probably quite reasonable (Melrose, 1988). Assuming that the outflow end does indeed remain saturated throughout the duration of the test and that no major discontinuities exist inside the rock, such as a large cross-cutting fracture taking up the majority of the cross section, then the applied centrifugal potential is known throughout the specimen. During such a test, when all flow stops for a given rotational speed, then the sample can be said to be in a state of equilibrium, and thus the matric suction is equal and opposite to the applied centrifugal potential. If the water content is known all along the core in this state, then the moisture retention curve can be determined. In a typical transient centrifuge test, the sample cannot

be monitored internally, so the only indication of fluid saturation is the collected outflow volume with time. When the slope of the outflow curve flattens out enough (Figure 6.1), the sample is assumed to be essentially at equilibrium.

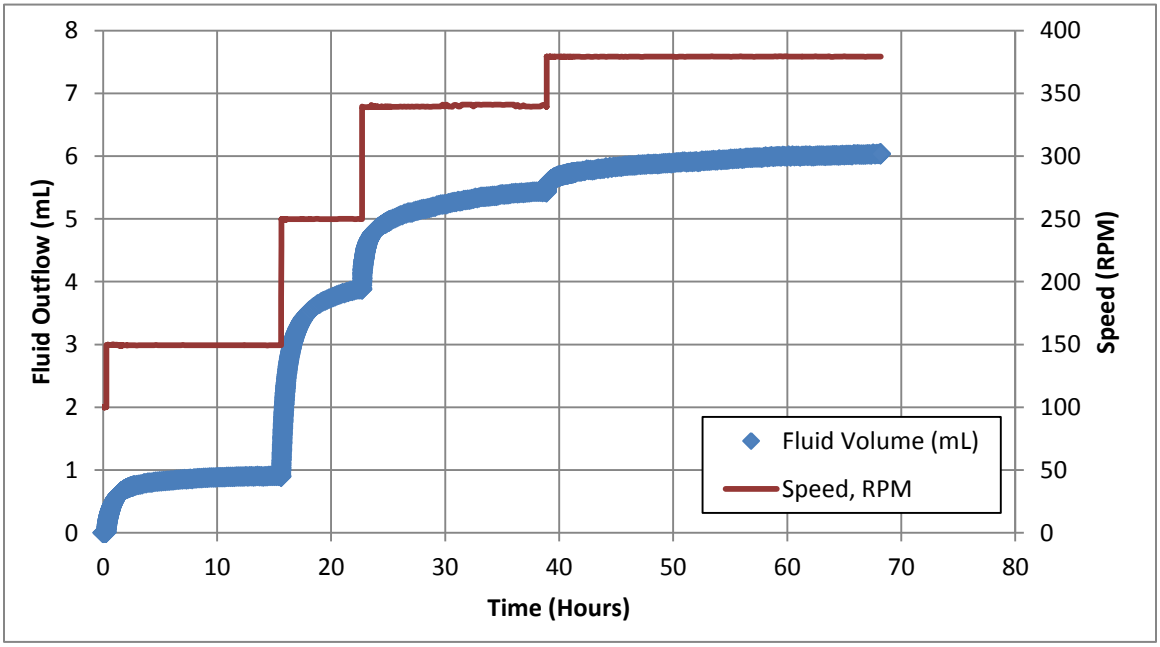

Figure 6.1: Flow Plateaus in Multi-stage Centrifuge Test

The primary result of the centrifuge tests is the retention curve of the rock-fluid combination as a function of the applied suction. As discussed in above in the Chapter 2.2, the centrifuge speed determines the average applied suction to the sample at equilibrium, while the measured outflow determines the average saturation for each step in centrifuge speed. The values plotted in these curves correspond to the last measured value of outflow at any given speed step. If that particular speed step was not run for a long enough time, then the outflow curve will not actually be that close to equilibrium, and the water content plotted in the retention curve will be too large for that given suction. The retention results of all the brine tests on the "A" cores are plotted in Figure 6.2:

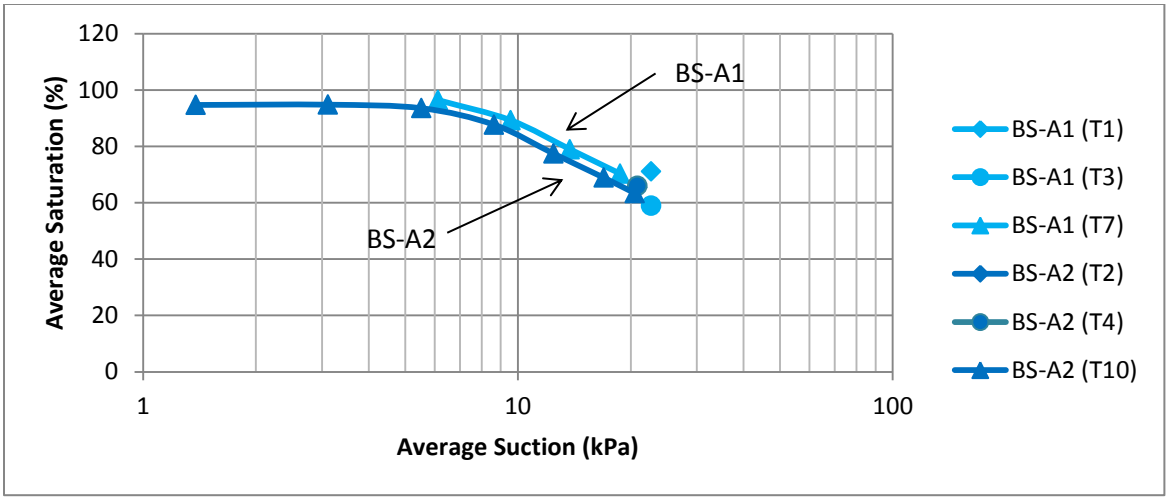

Figure 6.2: Average Centrifuge Measurements on "A" Cores

Generally, these tests show good agreement as to the average behavior of the brine in the rock under the same suction conditions. Cores BS-A1 and BS-A2 do exhibit slightly different retention behavior based on this test data, however, the difference between the curves is less than about 3 kPa in suction, so the cores were deemed identical for all practical purposes. A similar comparison is made between the results of the "A" Cores and the results of the "B" cores using brine as the wetting fluid:

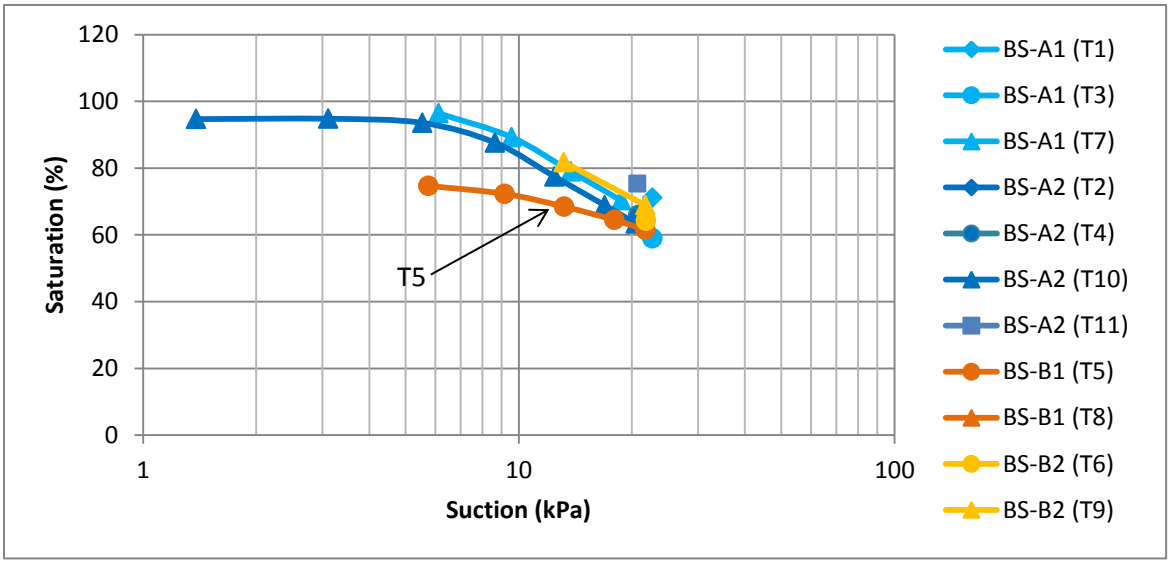

Figure 6.3 Average Centrifuge Measurements on all Cores

As shown in Figure 6.3, the measured retention is comparable among the four core plugs. Seeing as these cores were drilled from the same block in close proximity, this is not unexpected. The one apparently gross exception to this data is Test 5. Test 5 on Core BS-B1 began near 75% saturation, so the actual saturation at the outflow end is probably climbing toward 100% even while some outflow occurs from this incompletely saturated end at each speed step. This challenges all of the major assumptions made about the suction and saturation distribution in the conventional interpretation of the centrifuge test, which state that the outflow end starts from zero suction and 100% saturation. It is likely within the context of the way that the centrifuge applies force to the liquid, that the drainage suction-saturation relationship in T5 is still the same as in the other drainage experiments, but the applied suction does not span a range from 0 to a maximum at the top of the core. Instead it is probably shifted upward by about 10 kPa. This implies that the suction values as plotted in T5 are too low, and that the curve should actually be compressed upward along the suction axis. As the speed is sequentially increased during the test, however, the core approaches a state similar to that established in other tests starting from 100% saturation, so the interpreted results approach the other measured curves. This test demonstrates the importance of using cores fully saturated with the wetting fluid, or the imposition of a true zero-suction boundary condition in order to use the conventional interpretation of the centrifuge suction profile from the centrifuge speed. One other interesting observation from this data is that single stage tests run directly at a speed of 385 RPM (corresponding to an average suction around 20 kPa) did not tend to drain as much as the other multi-stage tests. This is likely a result of the behavior shown in Figure 5.1, where a finite but decreasing slope exists in the data at late times, indicating that the flow throughout the core asymptotically approaches zero as the suction equilibrates and the hydraulic conductivity decreases. Consequently, if the slope at late times was not very close to zero, the measured saturation will be consistently larger than that predicted from a longer test. This is especially noticeable in T11, where the supposed average equilibrium saturation is nearly 15% higher than in other tests which had been run for much longer overall times.

As previously discussed, the actual centrifuge measurement corresponds to the average saturation of the core at each speed, whereas the actual water content should be distributed along the core according to the applied suction profile and the true retention curve as illustrated in Figure 6.4:

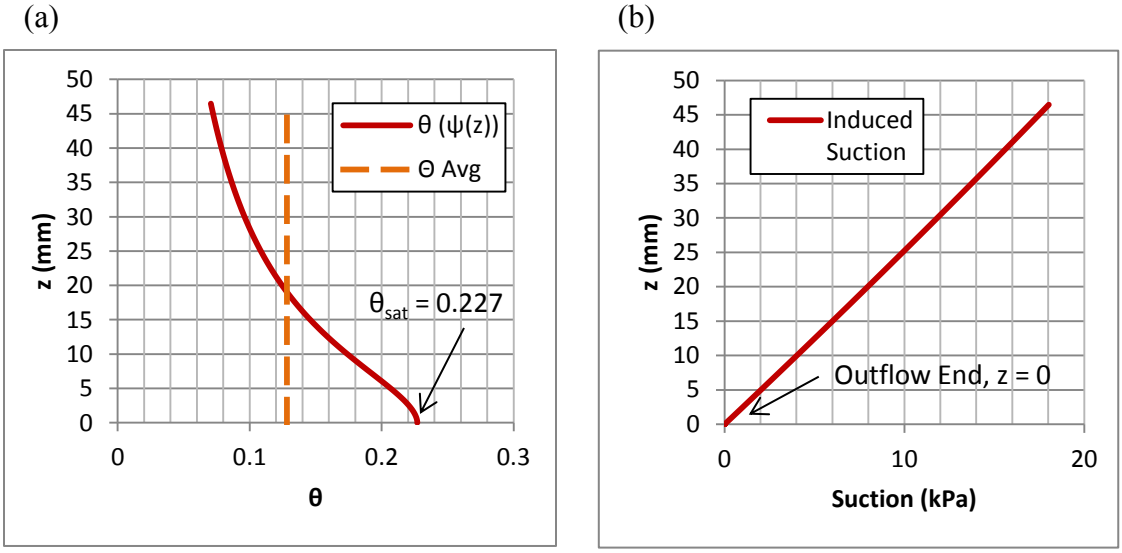

Figure 6.4: Theoretical Centrifuge Profiles: (a) Equilibrium Moisture Profile and (b) Suction Profile

Consequently, an unknown function representing the true moisture retention must integrate over the applied suction profile to give the average saturation as measured at the end of each speed step in the test:

$$\Theta_{avg} = \int_{\psi(0)}^{\psi(L)} \theta\big(\psi(z)\big)\, dz \qquad (6.1)$$

Where Θ_{avg} is the average volumetric water content over the whole core

ψ is the suction at any location along the core

θ is the actual volumetric water content anywhere along the core

z is the length dimension

L is the length of the core

Two similar iterative methods were used to find the best-fit retention functions, which were modeled using Van Genuchten functions (Van Genuchten 1980).

The first method to determine the retention function is to numerically compute the integral over the applied suction range of an assumed retention curve for each testing speed, and then minimize the error between the numerical integral and the measured data by manipulating the retention parameters, α_s and n_s, using Microsoft Excel's *Solver* function. Given the appropriate set of starting parameters, this algorithm can find an extremely good match every time. This method does provide such a good fit to the data, though, that if the measurement itself was not close enough to equilibrium, then the retention function will reflect the establishment of equilibrium when, in fact, there was still more flow to occur. The ideal situation for a model of the retention, then, would be to find a curve which is slightly lower than the measured values so that a full history match of the transient data can find a more appropriate K-function to describe the transient measurements up to the point that the test was stopped.

The other method adopted herein to address this issue was to randomly postulate a retention function and integrate it over the supposed suction conditions during the test at equilibrium and check how well the integral matches the measured data, while ensuring that the last measured data point is larger than the corresponding value from the numerical integration. This stipulation helps ensure that the retention curve is biased toward slightly more outflow than was measured, so that the K-function in the subsequent history matching procedure will be more reasonable. Functions outside of the given fitting tolerance are discarded. One example of such a function and its integral is shown in Figure 6.5:

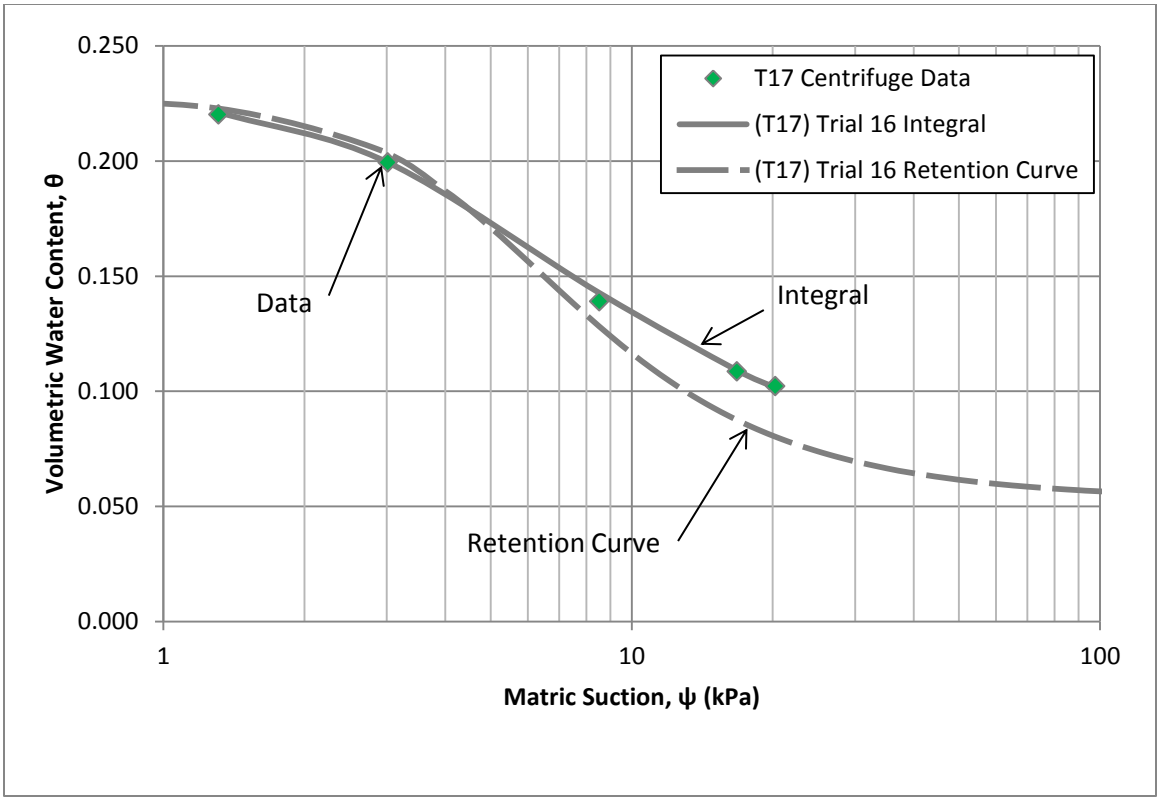

Figure 6.5: Retention Function and its Integral

In fact, several functions can equally satisfy the integration condition if the fitting tolerance is broadened, but within the center of the data they all match quite well, as seen in Figure 6.6.

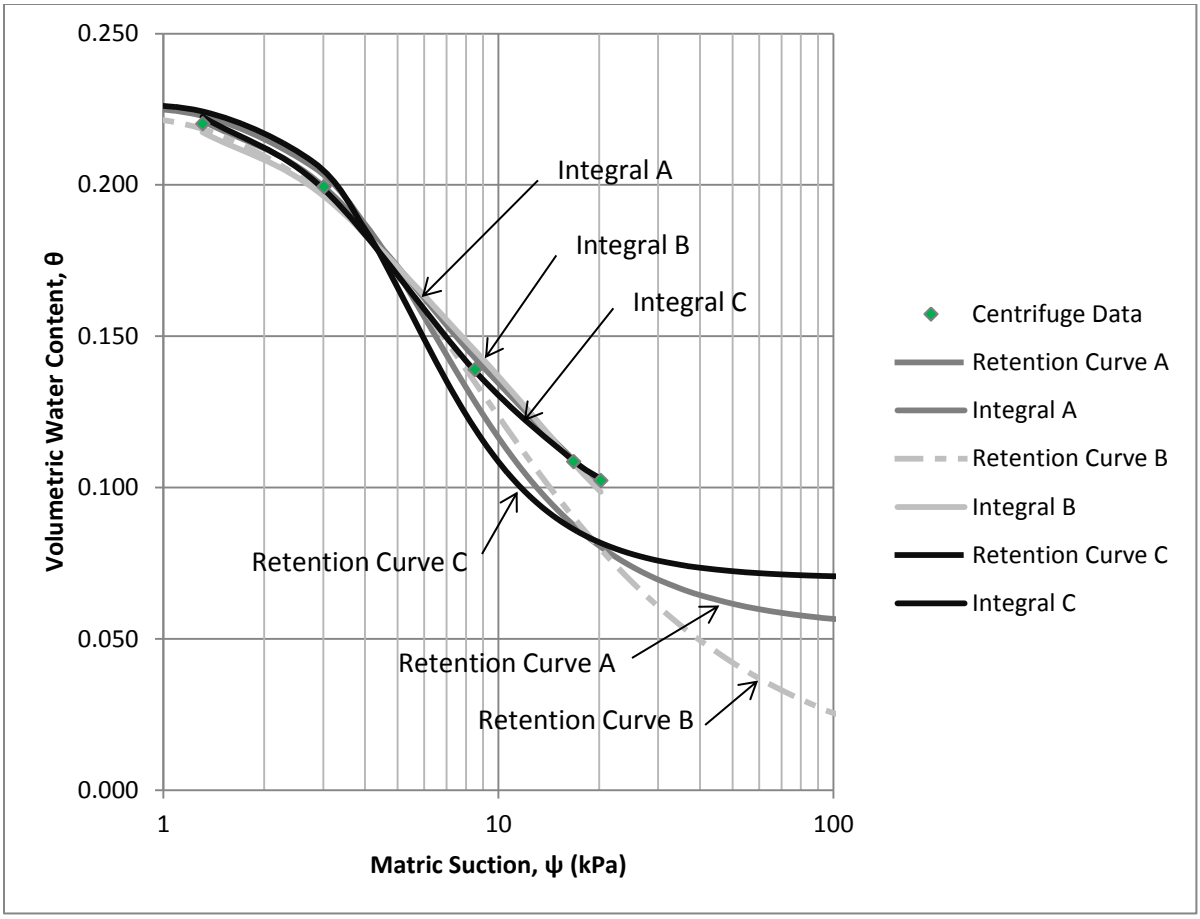

Figure 6.6: Multiplicity of Possible Retention Functions

The last few data points toward the high suction range provide insight into what occurred at comparatively low speeds, but the true curve cannot be known with precision at the highest measured speeds strictly from a centrifuge measurement, due to the uncertainty in fitting the data.

Combining the centrifuge results with the CT scan results after centrifuging can give some additional insight into which retention curves make more physical sense. Figure 6.7 shows the data from Test 17 conducted on a surfactant saturated core, and CT results from Test 15 conducted using the same fluid.

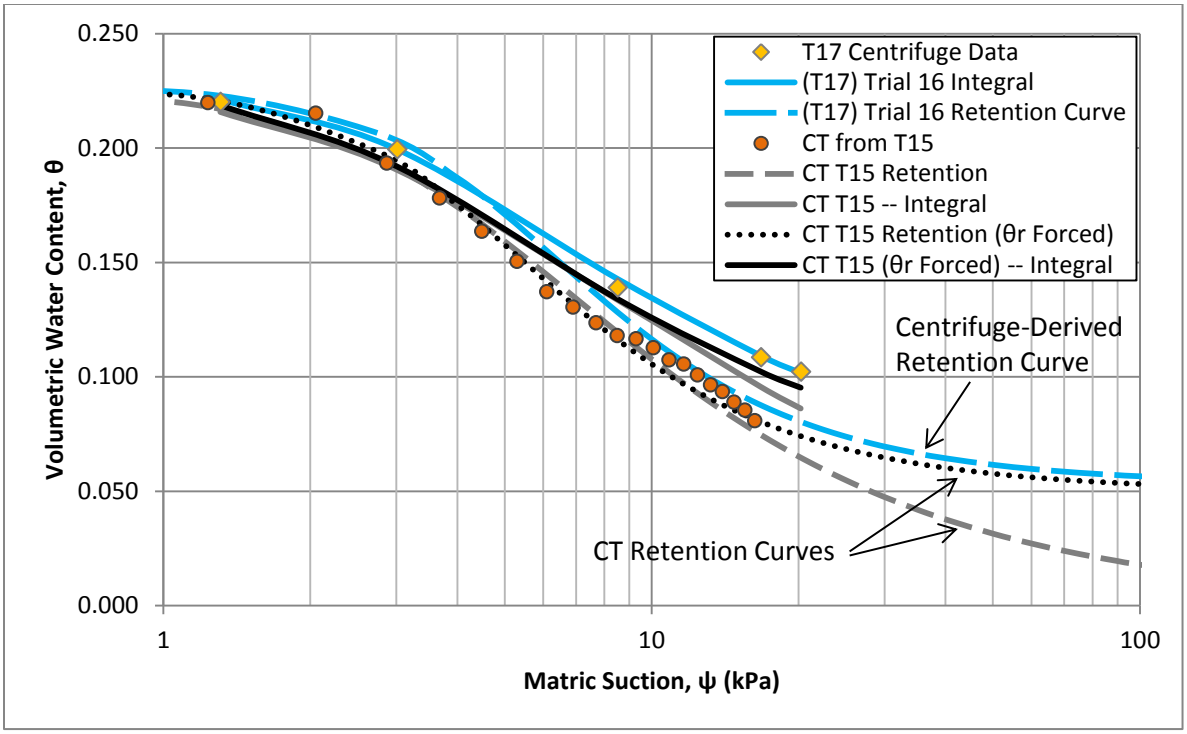

Figure 6.7: Match between Centrifuge and CT Retention Curves

Again, several possibilities exist for the residual water content based on this fitting. For consistency in later comparisons between different fluid types, the residual water content will be fixed between 0.053 and 0.054, though this is not strictly necessary for a comparison of the low suction regime measured in these tests.

6.2 Effect of Liquid-Gas Interfacial Tension

The measured average centrifuge retention curves are plotted in Figure 6.8 for all four fluids tested here:

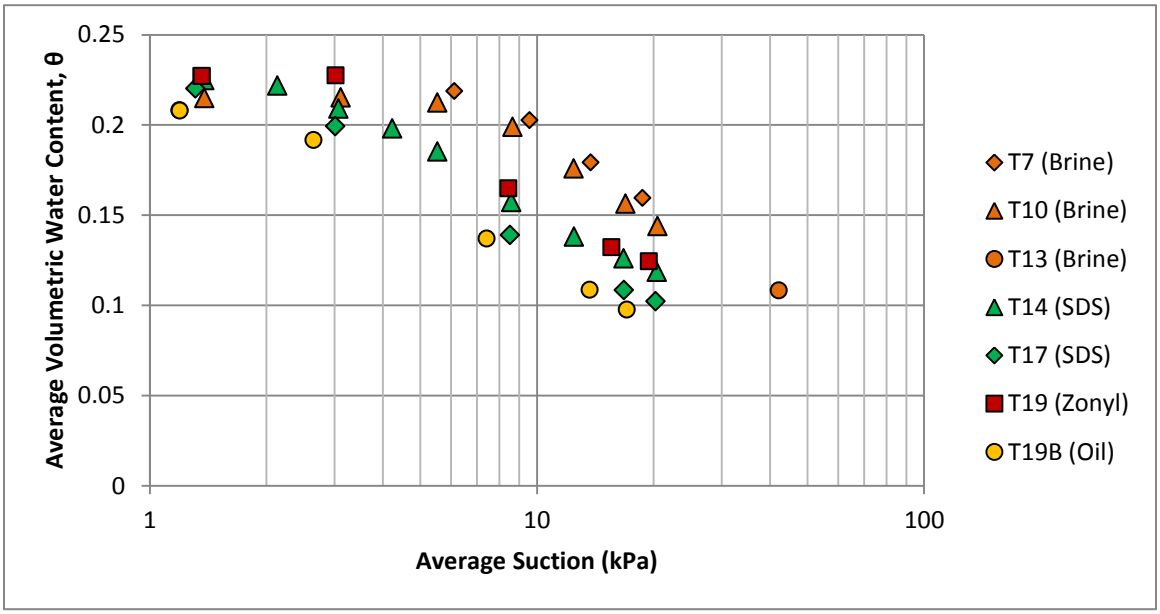

Figure 6.8: Raw Centrifuge Retention Data for all Fluids

This figure shows that the average retention behavior for these cores does tend to translate along the suction axis. In order to evaluate the effect of the surface tension more carefully, reasonable retention curves are fit to the data, as seen in Figure 6.9, again noting that the residual water content value has been fixed between 0.053 and 0.054 for consistency between models, and because no measurements were taken in the high suction region.

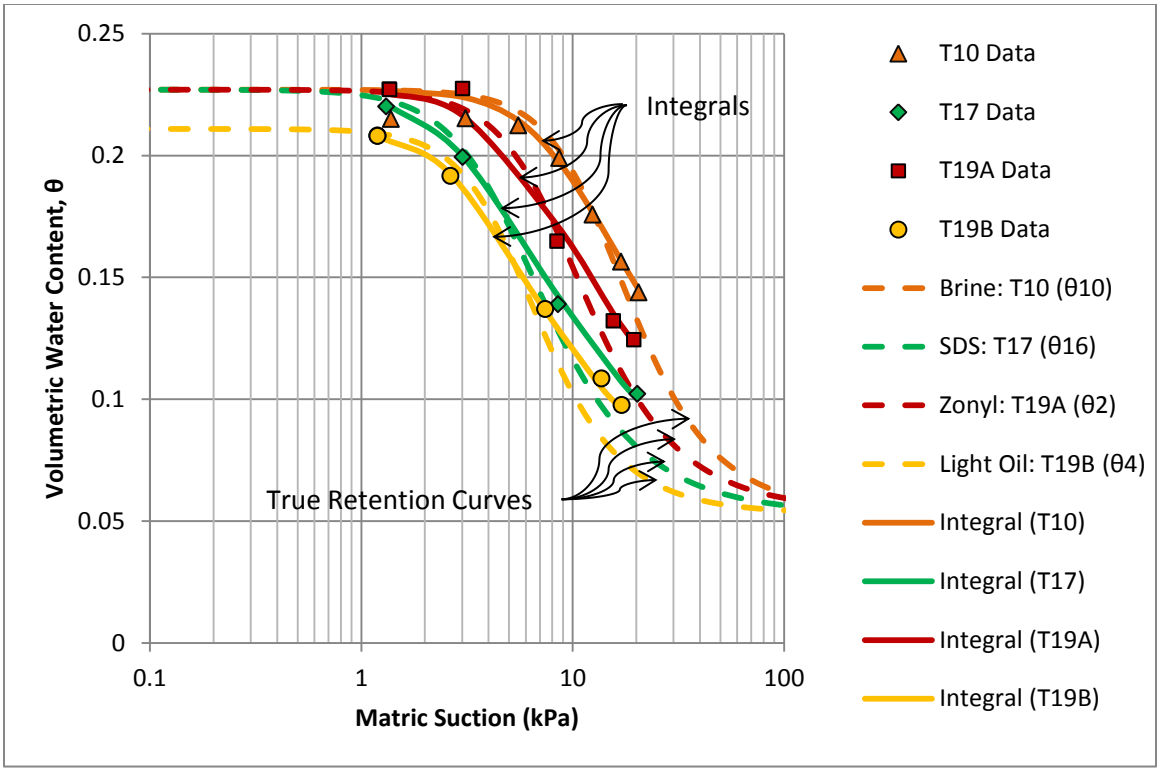

Figure 6.9: Retention Models for each Fluid

Figure 6.9 shows the retention curves and their integrals plotted with the measured data. The retention curves all match the data well. Additionally, the retention curves all generally assume the same shape.

Comparing the back-fit retention curves to the measured fluid distribution inside the cores afterward using X-Ray CT, generally good agreement is observed between the centrifuge and CT interpretation. These are plotted in Figure 6.10:

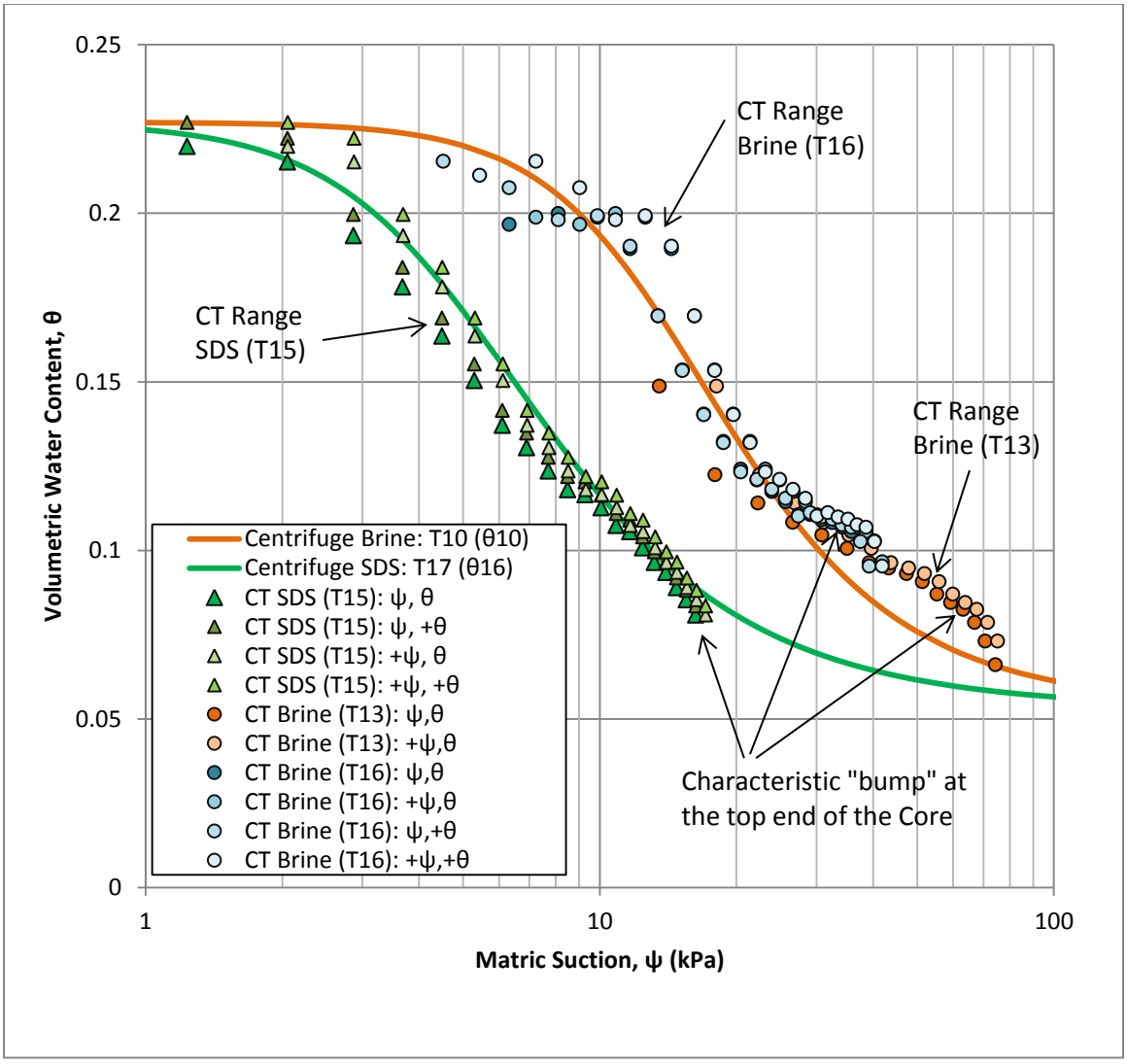

Figure 6.10: Comparison of Centrifuge Models and CT Data Range

Figure 6.10 shows the most probable range for the measured CT data after accounting for uncertainties in the measured saturation and assumed suction distribution. The data show that the retention model is reasonably consistent between the inferred behavior from the centrifuge data and the post-centrifuge Computed Tomography measurements. Additionally, the internal measurements from the CT confirm that the results do in fact scale by the interfacial tension of the two fluids in the system. One feature which is present in all of the CT scans conducted after centrifuging is the characteristic “bump” in

the volumetric water content at the highest suctions measured in that core. This feature may be a consequence of the fluid redistribution after spinning down the centrifuge, as the water content is always apparently larger at the top end of the core for any given suction, even where testing data overlap, as in Test T13 and T16. Another possible explanation for this characteristic feature is insufficient centrifuging time during the test. Given that Test T15 was under one centrifugal speed for up to 90 hours prior to scanning, however, this explanation is unlikely.

Table 6.1 shows the model parameters which best fit the retention data for each of the four fluid types. In these models, the residual saturation has been fixed to within 0.053 and 0.054 for consistency, and because no data was collected in the high suction range.

Table 6.1: Best-fit Van Genuchten Retention Curve Parameters

Test	Sample	Fluid	σ_{gl} (mN/m)	a_s (ψ in kPa)	n_s	m_s	θs	θr	$1/4a$ (kPa)
7	BS-A1	Brine	72	0.0585	2.9848	0.6650	0.2270	0.05330	4.27
10	BS-A2	Brine	72	0.0716	2.6200	0.6183	0.2270	0.05330	3.49
14	BS-A2	SDS	30	0.1489	2.2542	0.5564	0.2270	0.05330	1.68
17	BS-A2	SDS	30	0.1982	2.3211	0.5692	0.2270	0.05321	1.26
19A	BS-A2	Zonyl	52	0.1073	3.1088	0.6783	0.2270	0.05330	2.33
19B	BS-B2	Light Oil	28.5	0.1883	2.6679	0.6252	0.2109	0.05331	1.33

In the Van Genuchten model, the air entry capillary pressure for this data is found to be roughly equal to $1/(4\alpha)$. Plotting the air entry value against the interfacial tension, there is a good trend to the scaling behavior as seen in Figure 6.11:

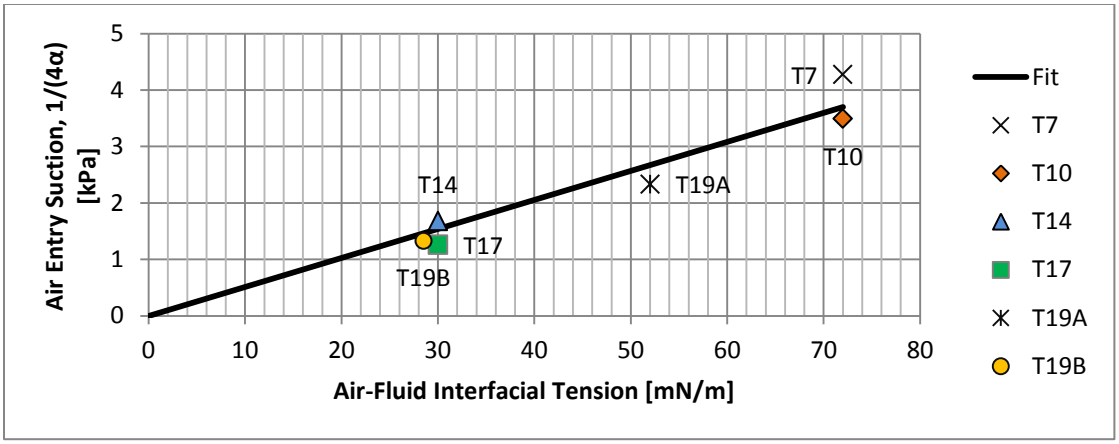

Figure 6.11: Scaling Between Air Entry Pressure and Interfacial Tension

Figure 6.12 shows the n-parameter plotted against the interfacial tension. In the Van Genuchten model the slope of the capillary pressure curve in the range of mobile saturations is dependent on *n*. There is no real trend in the n-parameter with the interfacial tension, which shows that the saturation-suction curves are all roughly parallel in the funicular saturation regime.

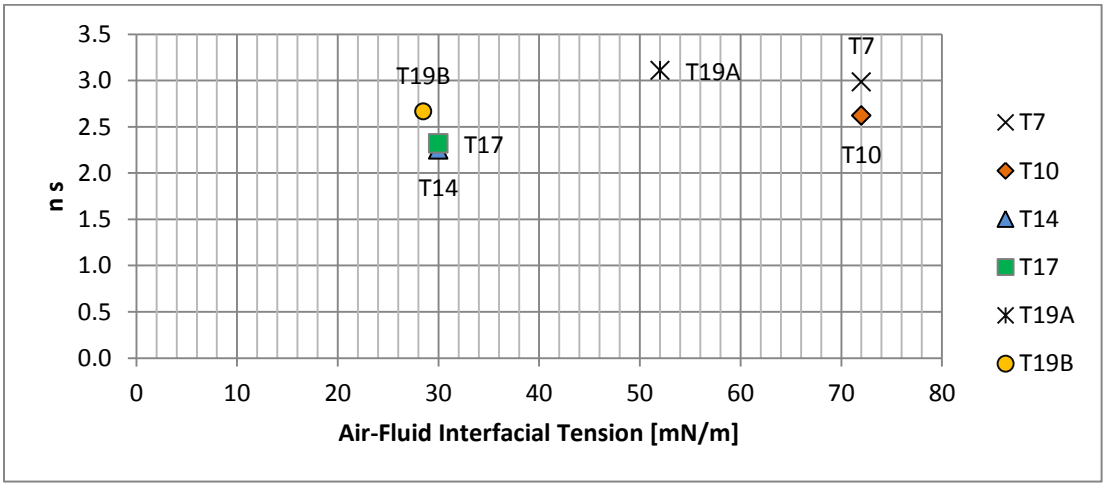

Figure 6.12: Scaling of Van Genuchten n-parameter

6.3 Time Histories and Back-fit Models.

In order to assess the quality of the fit between the measured data and the transient model, retention functions were chosen as discussed previously to match the flattened

portion of the transient outflow curve, at which point the assumption is that equilibrium has been nearly achieved. Suitable K-functions were then picked by trial and error within a given range of parameters, and the total error between the measured data and the simulation was computed for each fit point. More details about the numerical fitting scheme are included in Appendix A.

6.3.1 Model Quality

The results of some better and worse models for the transient outflow time history are shown in Figure 6.13, along with the measured data from Test 17 on an SDS saturated core:

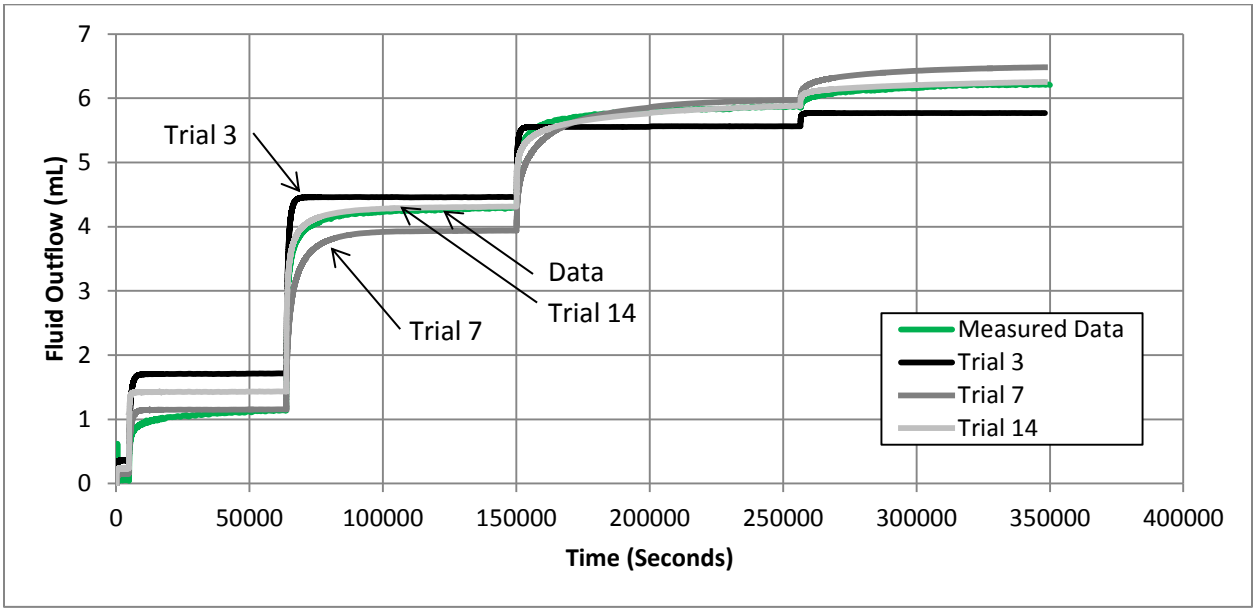

Figure 6.13: Sample History Matches for SDS Saturated Core (T17)

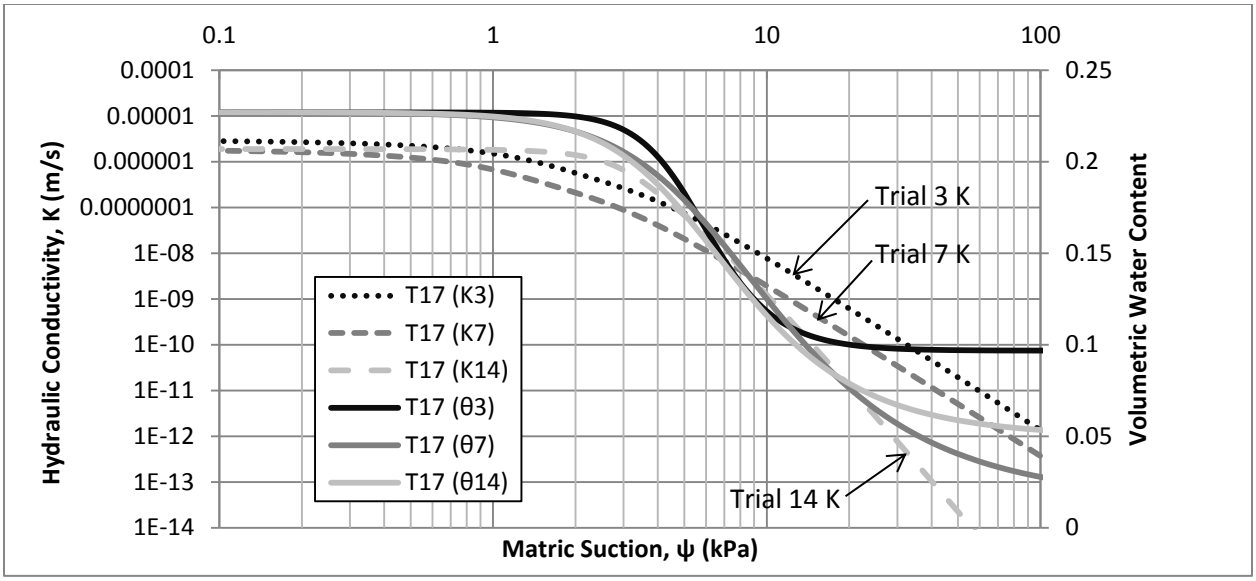

Figure 6.14: Input Retention and Conductivity Models

The results of a few numerical simulations are shown above to illustrate some of the better and worse models used to fit the transient outflow data. Trial 3 uses a retention curve with a comparatively large residual water content, meaning that as fluid drains, high suctions are reached relatively quickly and the suction profile equilibrates with the centrifugal potential relatively quickly. The K-function which provided the best fit for that retention curve in Trial 3 maintains a comparatively large conductivity value at large suctions; consequently the simulated time history is too step-like, with very flat plateaus during late times for each speed step. Additionally, the time history over-predicts flow at low speeds and under-predicts flow at the larger speeds due to the large residual water content. Trial 7 uses the opposite extreme in the retention curve, namely that the curve is very smooth down to the residual water content, which is itself much smaller. Because of this, the suction does not increase as much for each small loss in fluid. The best fit K-function in this case has a similar shape to that in Trial 3, but the overall conductivity itself is much lower, leading to a much smoother shape in the outflow curve. Additionally, because the residual water content is so small, the outflow curve tends to under-predict the flow at low speeds and over-predict the flow at high speeds. Trial 14 uses a retention curve which falls somewhere in between the other two trials. The

hydraulic conductivity function which provides the best fit remains reasonably large until near the air entry suction, at which point it decreases markedly with the increase in suction. The combination of this retention curve and K-function provides a good quality fit to the data. It should be noted that all of these simulations began with an initial saturation condition which was larger than measured in the actual test itself. This artifact manifests itself in the small plateau which is always larger than the measured data during the first speed. Subsequent models accounted for the true starting saturation, though the effect upon the best-fit hydraulic conductivity function was relatively minor. Table 6.2 shows the parameters used in these analyses:

Table 6.2: Input Parameters to Simulations

Parameter	Trial 3	Trial 7	Trial 14
S_0		0.999	0.999
S_L		0.951	0.951
as	0.00018566	0.00016333	0.00019442
ns	3.79761187	2.01231939	2.31512057
ms	0.73667662	0.50306099	0.56805705
θr	0.09681049	0.01531443	0.04988281
θs	0.227	0.227	0.227
ak	0.0004354	0.00058209	0.0002649
nk	2.93164171	2.89830024	4.51772818
mk	0.6588942	0.65497018	0.77864981
Ksat (m/s)	0.000003	0.0000019	0.0000019
Fit Error (mL/Data Point)	0.03415068	0.03015883	0.01561416

In general, changes in the retention curve tend to control the asymptote at each speed, while changes in the K-function tend to control the curvature of the transient solution. The back-fit solution is not unique, however, because the retention curve controls the strength of the applied gradient at each speed step, but the K-function determines how quickly that gradient changes with time, so equally good fits can be derived using much different retention functions. Assuming that the core is perfectly at equilibrium when the centrifuge speed is increased for the subsequent step produces a vastly different K-

function than when the assumption is made that the core still had more liquid remaining to drain at that speed. This implies that any comparison among the four fluids must be made using comparable sets of inputs to the numerical analysis. In order to make this comparison among different fluids, the retention curve will be assumed as the best fit to the measured centrifuge data, and the best K-function describing the time history will be regarded as the hydraulic conductivity. The residual volumetric water content is fixed within the range from 0.053 to 0.054 for all simulations. While the numerical analysis will produce fits which match the data well, the interpreted K-function may tend to deviate from the true function at volumetric water contents below the range of testing performed in this study.

6.3.2 Simulation Results

The best simulation results are presented in this section for tests on each of the four fluid types. Good general agreement between the time histories and the measured data was observed in most of the tests. The input K-functions and retention curves are provided below each time history to provide context for the visual quality of the fit to the data.

6.3.2.1: SDS saturated Core (T17)

Three simulated time histories are presented in Figure 6.15. Visually these curves appear to have a reasonably good fit, but as shown subsequently in Figure 6.16 the predicted hydraulic conductivity functions are somewhat different, even for very similar retention functions.

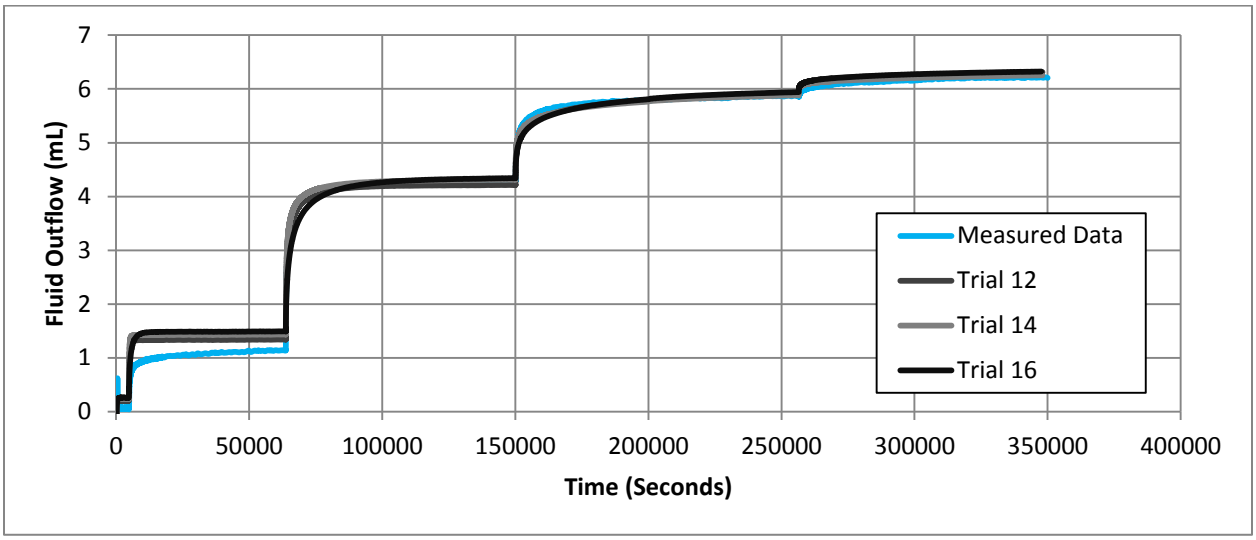

Figure 6.15: Time Histories for SDS Saturated Core (T17)

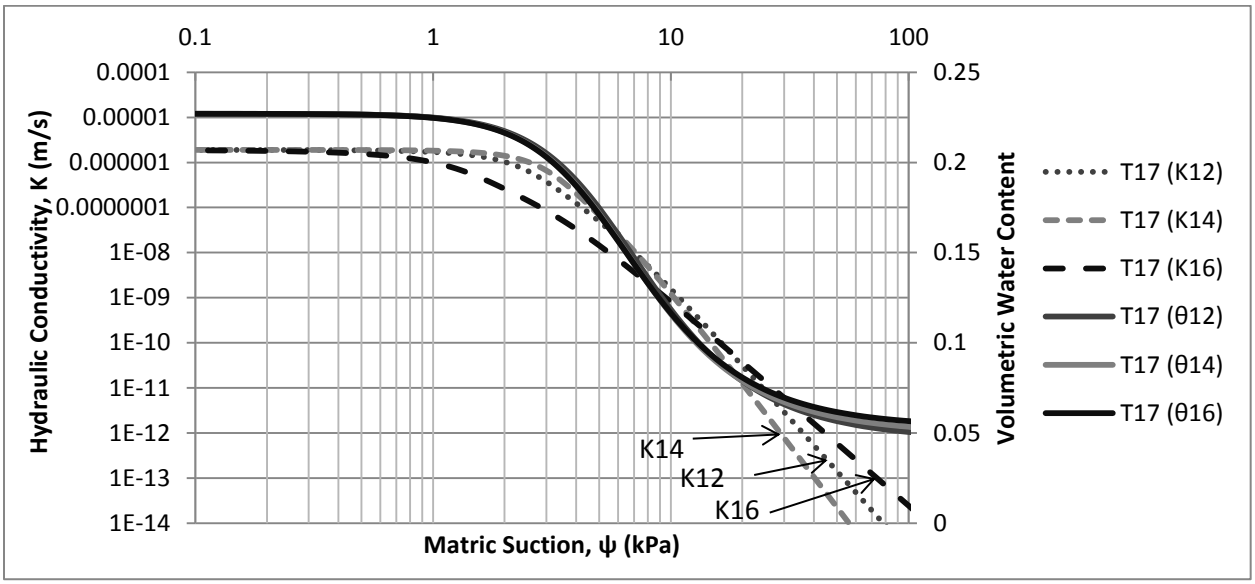

Figure 6.16: Best-Fit Hydraulic Models from SDS Simulations

A plot of the hydraulic conductivity against the water content is provided in Figure 6.17:

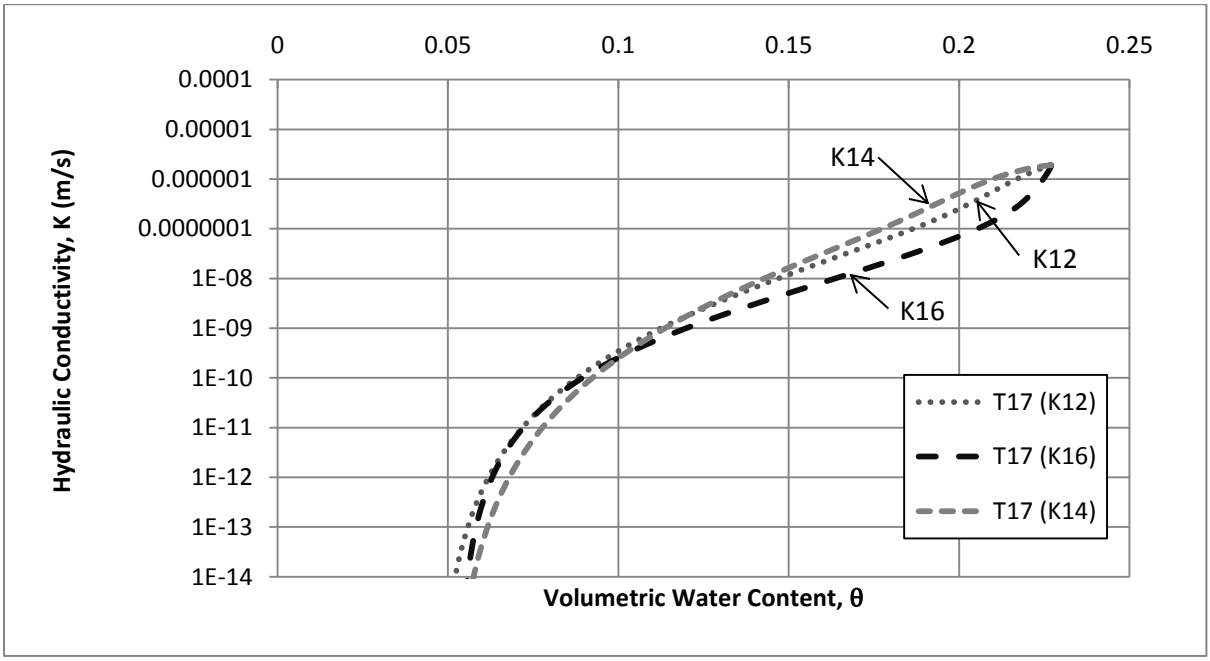

Figure 6.17 Hydraulic Conductivity vs Volumetric Water Content for SDS

Table 6.3 shows the parameters used in these analyses and the error between the simulation and the smoothed data:

Table 6.3: Best-fit Parameters from SDS Simulations (T17)

Parameter	Trial 12	Trial 14	Trial 16
S_0	0.999	0.999	0.999
S_L	0.951	0.951	0.951
as	0.0001849	0.00019442	0.00019825
ns	2.29284168	2.31512057	2.3211199
ms	0.56385999	0.56805705	0.56917348
θr	0.04640788	0.04988281	0.05321008
θs	0.227	0.227	0.227
ak	0.00030546	0.0002649	0.00051357
nk	3.99730709	4.51772818	3.30385911
mk	0.74983158	0.77864981	0.69732365
Ksat (m/s)	0.0000019	0.0000019	0.0000019
Fit Error (mL/Data Point)	0.0146	0.0156	0.0075

6.3.2.2 Oil Saturated Core (T19B)

Two simulations are shown for the oil saturated core in Figure 6.18. The results of the two simulations are reasonably similar; however, in Trial 6 the starting saturation in the simulation is probably closer to the real starting saturation in this centrifuge test, which results in a better fit during the first centrifuge speed.

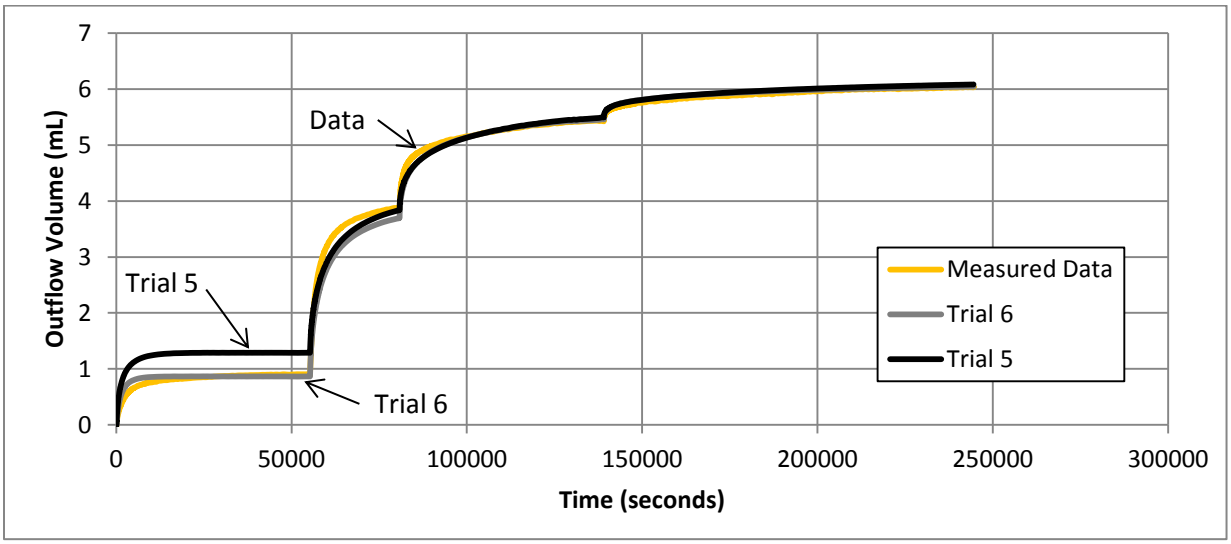

Figure 6.18: Time Histories for Oil-Saturated Core (T19B)

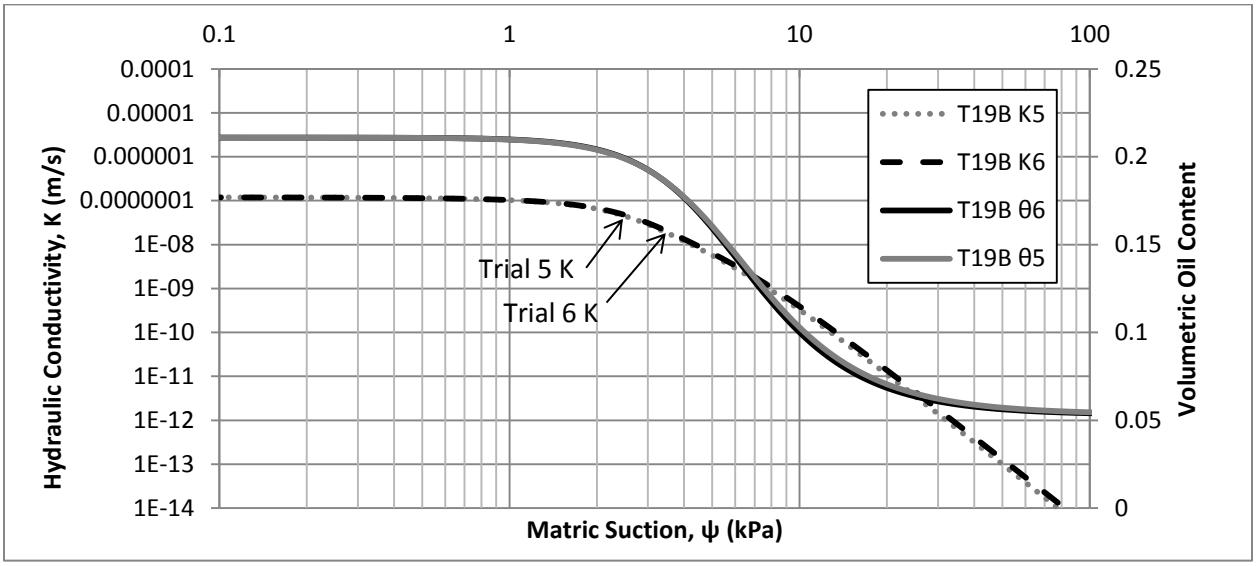

Figure 6.19: Best-fit Hydraulic Models from Oil Simulations

The saturated volumetric water content for this oil saturated core is only about 0.21 because some remaining salt from the brine crystallized inside the pores during the oven drying process while converting the core from water-wet to oil-wet.

The hydraulic conductivity as a function of the volumetric oil content is also plotted in Figure 6.20:

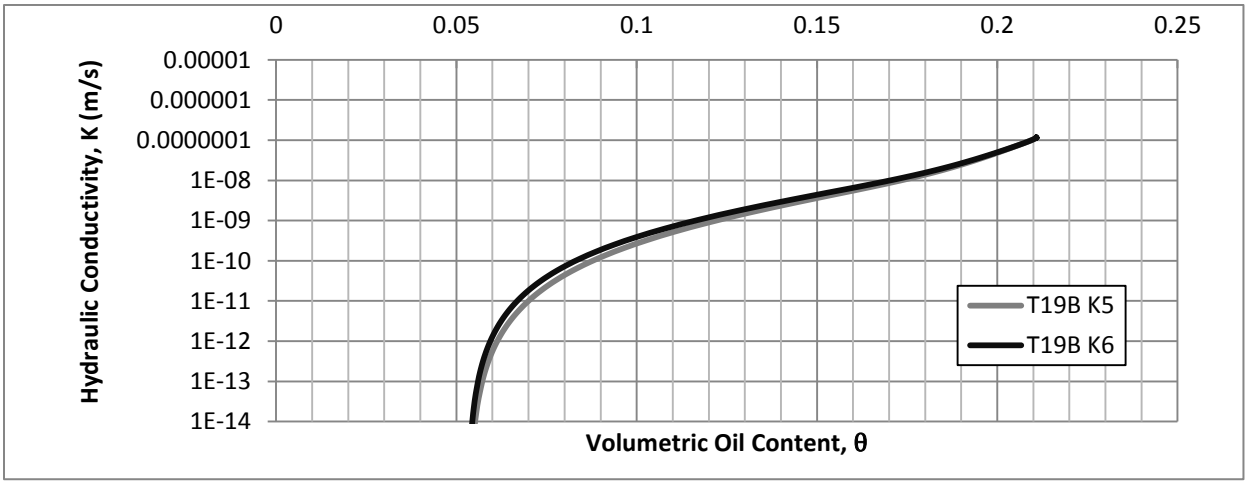

Figure 6.20: Hydraulic Conductivity vs. Volumetric Fluid Content for Oil

The parameters used in this simulation are included in Table 6.4.

Table 6.4: Best-Fit Parameters from Oil Simulations (T19B)

Parameter	Trial 5	Trial 6
S_0	0.999	1
S_L	0.975	0.964
as (ψ in Pa)	0.000188632	0.000189777
ns	2.655651091	2.73324636
ms	0.623444509	0.6341347
θr	0.053344977	0.05305553
θs	0.2109	0.2109
ak (ψ in Pa)	0.000279817	0.000271524
nk	3.637432212	3.617308449
mk	0.725080787	0.72355136
Ksat (m/s)	0.000000119	0.000000119
Fit Error (mL/Data Point)	0.0090	0.00782

6.3.2.3 Brine Saturated Core (T10)

Results from Test 10 on the Brine saturated core are shown in Figure 6.21. These simulations do not match the measured data as closely as the oil and SDS results. A larger range of possible K-functions and retention curves can describe the results when the global error is this large, as seen in Figure 6.22.

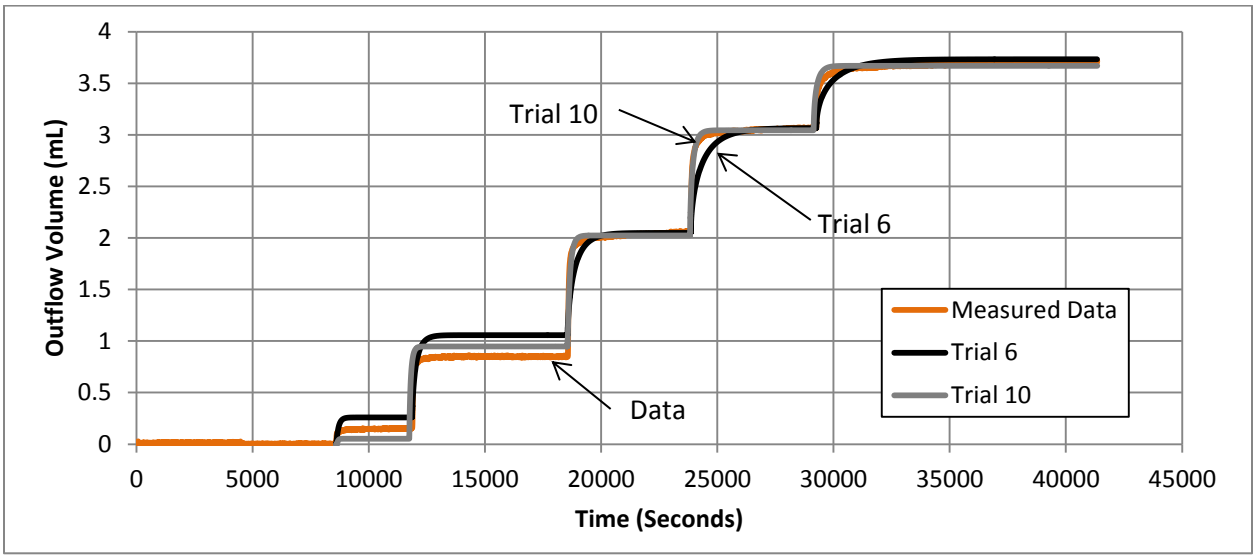

Figure 6.21: Time Histories for Brine Saturated Core (T10)

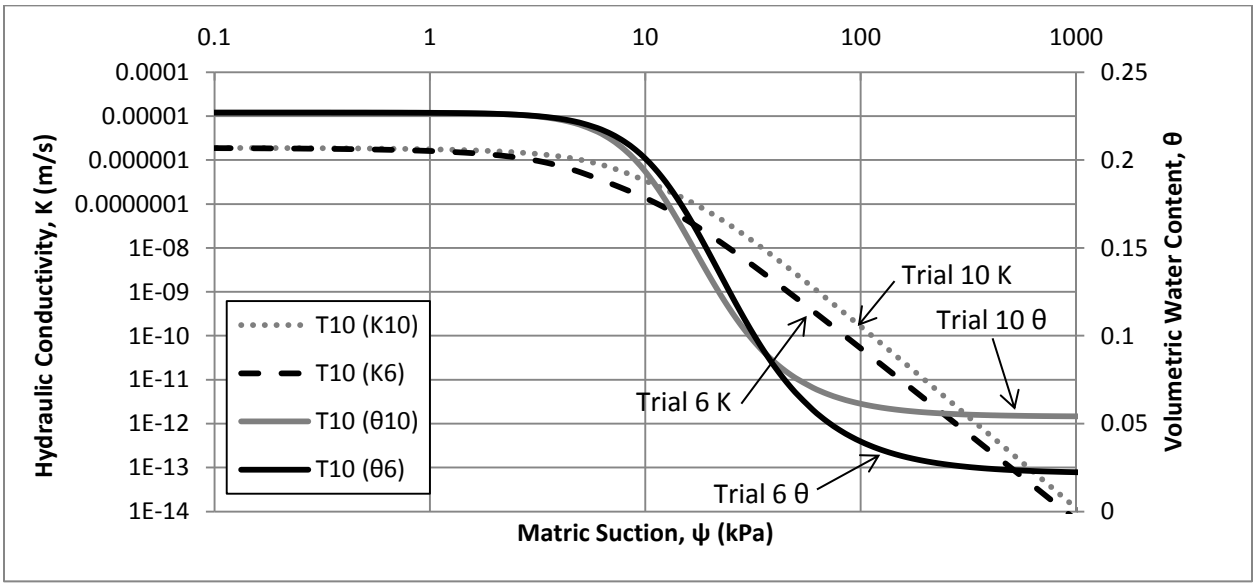

Figure 6.22: Best-Fit Hydraulic Models from Brine Simulations

Again, the hydraulic conductivity is plotted as a function of the water content in Figure 6.23:

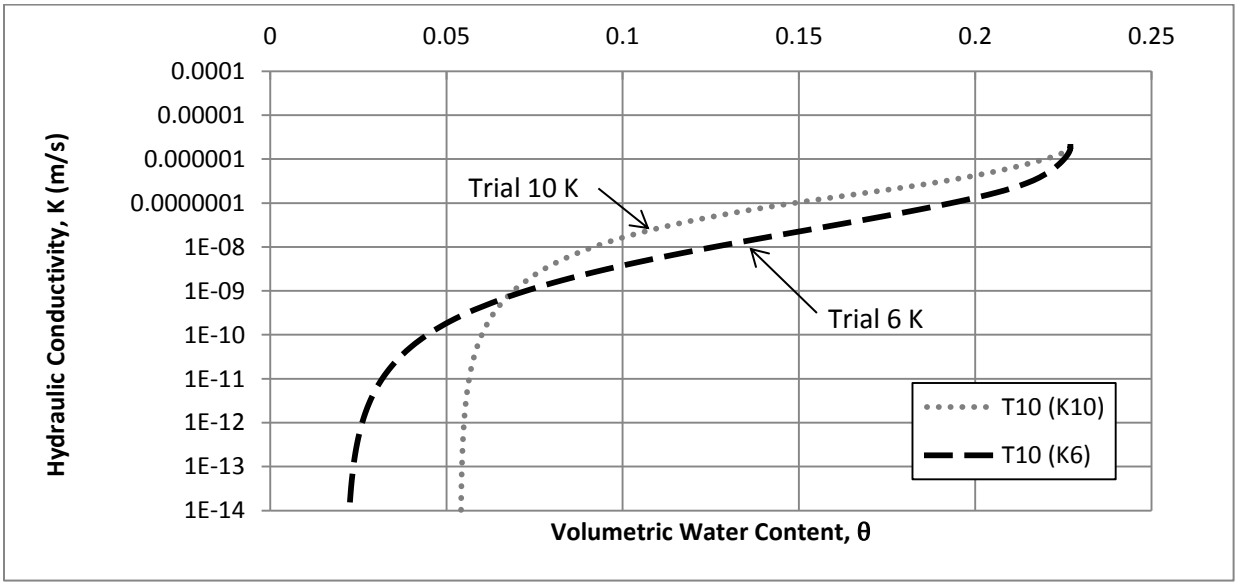

Figure 6.23: Hydraulic Conductivity vs. Volumetric Water Content for Brine

Parameters from these simulations are included in Table 6.5:

Table 6.5: Best-fit Parameters from Brine Simulations (T10)

Parameter	Trial 6	Trial 10
S_0	0.999	1
S_L	0.900	0.865
as (ψ in Pa)	0.000057163	0.000071549
ns	2.383023888	2.603960465
ms	0.580365096	0.615969592
θ R	0.021604185	0.053984427
θ S	0.227	0.227
ak (ψ in Pa)	0.000141374	9.11973E-05
nk	2.968735208	3.090786057
mk	0.663156216	0.67645771
Ksat (m/s)	0.0000019	0.0000019
Fit Error (mL/ Data Point)	0.0036	0.0023

6.3.2.4 Zonyl Saturated Core (T19A)

Simulation results from Test 19A on the Zonyl saturated core are reproduced in Figure 6.24. The retention function was picked to have the same residual water content as in the other core tests, and the best possible fit was determined from the plateaus in the time history, as before. This model does not describe the data very well, as the predicted flow stops sooner than the measurements indicate. This is likely due to the hydraulic conductivity function dropping off too quickly with the water content, which essentially shuts off the flow for the given applied gradient.

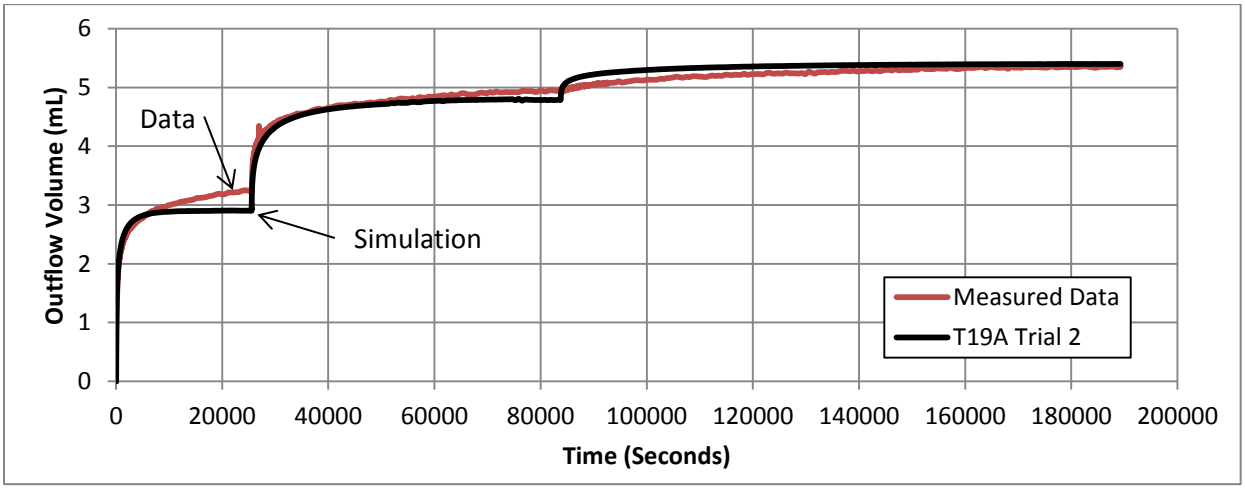

Figure 6.24: Time Histories for Zonyl Saturated Core (T19A)

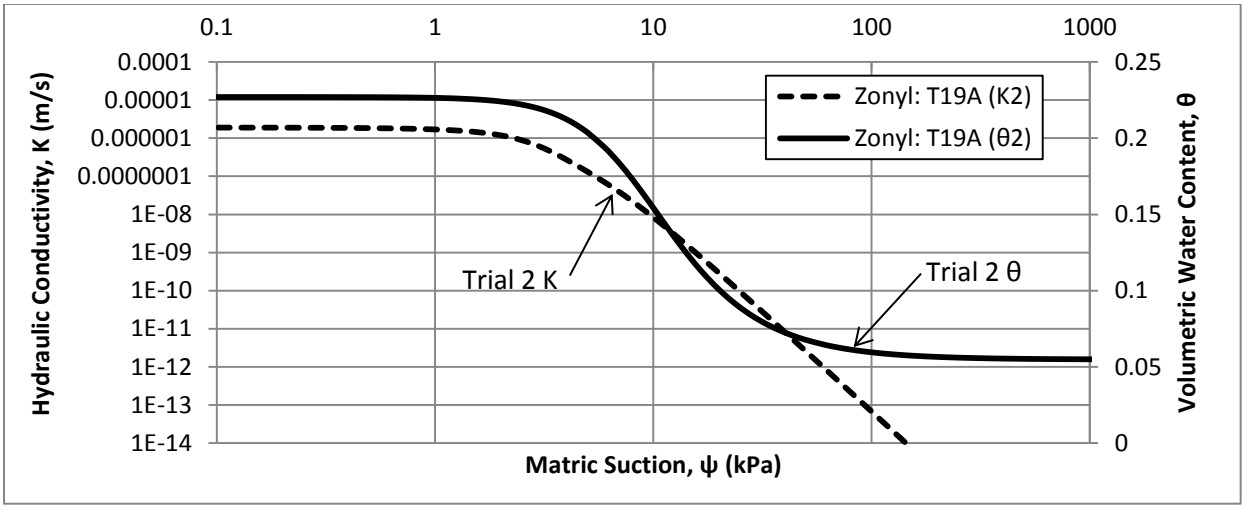

Figure 6.25: Best-Fit Hydraulic Models from Zonyl Simulations

The hydraulic conductivity as a function of water content is plotted in Figure 6.26:

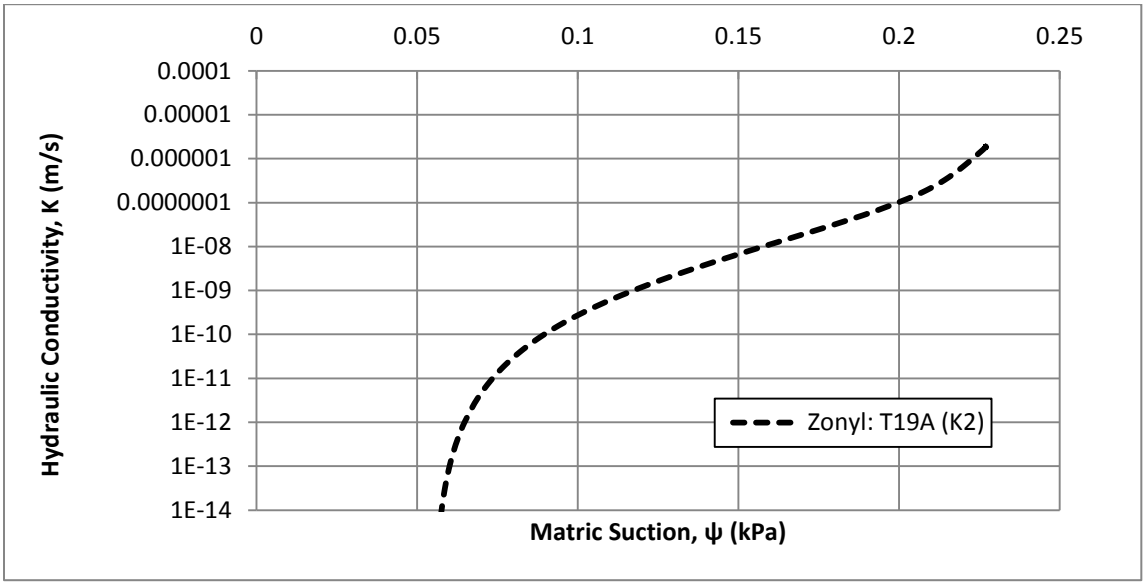

Figure 6.26: Hydraulic Conductivity vs. Volumetric Water Content for Zonyl Simulation

Parameters used in this analysis are included in Table 6.6:

Table 6.6: Best-fit Parameters from Zonyl Simulations (T19A)

Parameter	Trial 2
S0	1
SL	0.9997
as	0.0001188
ns	2.450
ms	0.5919
θr	0.0548
θs	0.227
ak	0.0002506
nk	3.656
mk	0.7265
Ksat (m/s)	0.0000019
Fit Error (mL/ Data Point)	0.0121

6.4 Comparison of Best-fit K functions

Given a reasonable quality fit of the transient solution of the centrifugal Richards' equation, and a consistent set of input retention functions, it is relevant to compare the best fit K-functions to observe how they change based on the fluid type, and how the interfacial tension and viscosity control the transient behavior. Figure 6.27 shows the best fit K-functions from each of the successful history matches in terms of the volumetric wetting fluid content:

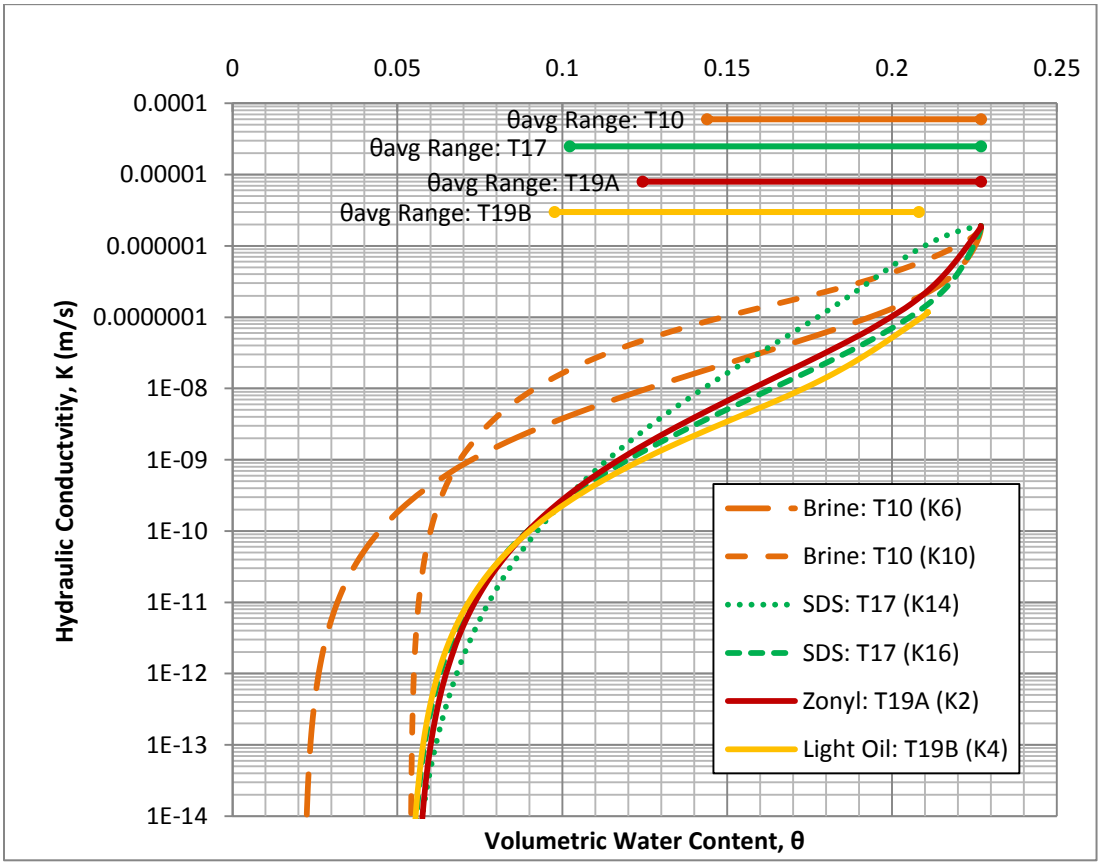

Figure 6.27:Comparison Between Best-Fit Hydraulic Conductivity Functions

Theoretically, these curves in Figure 6.27 ought all to fall in the same narrow band if the viscosity and density are similar. The functions do match within one order of magnitude over the water content range from 0.17 to 0.227, which corresponds to the majority of the measurement range during T10 on the brine saturated core. The reliability of the

simulation for values outside of the measured range is suspect, due to the multiplicity of possible retention functions which can fit the data. For the same quality of fit to the transient data, there is more variability in the possible K-function which can describe the behavior of the rock-fluid combination. This is partially because the K-function is very sensitive to the input parameters, and the fit is very sensitive to both the K-function and the retention curve (which helps control the hydraulic gradient during the test). The choice of a different retention curve can change whether the simulation was very close or not to equilibrium, which has a direct effect on the necessary K-function required to fit the data (c.f. T10 fits in Figures 6.21 and 6.22, above).

These same functions are plotted against the matric suction in Figure 6.28:

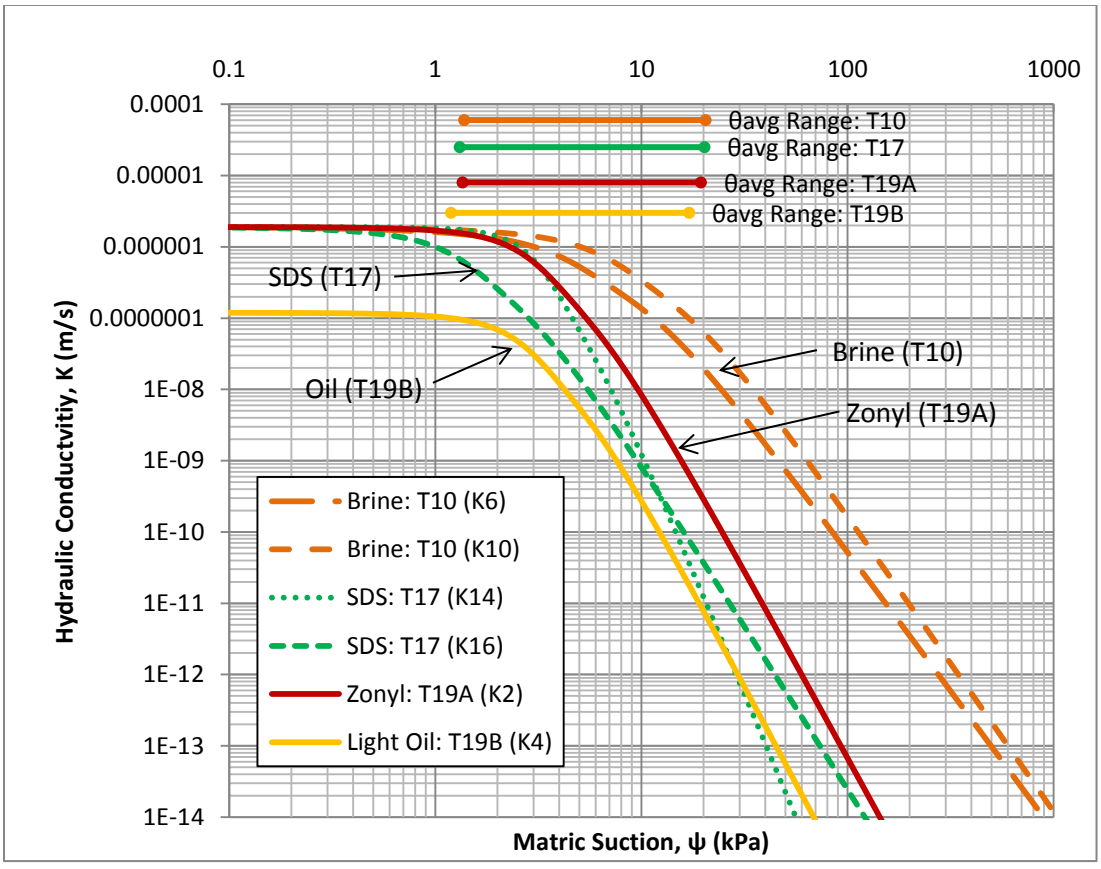

Figure 6.28: Suction Dependence of Best-Fit Hydraulic Conductivity Functions

Comparing the best input K-functions as a function of suction, there is a slight resemblance to the scaling between the retention behavior, however, the scaling coefficient is not nearly as obvious as in the retention functions. Whereas the retention behavior consistently scaled by the interfacial tension, the hydraulic conductivity is not that clean when scaled.

In fact, because of the different viscosity and density of the fluids, it is more reasonable to compare the intrinsic permeability as a function of water content and suction. Figure 6.29 shows the interpreted intrinsic permeability from these tests:

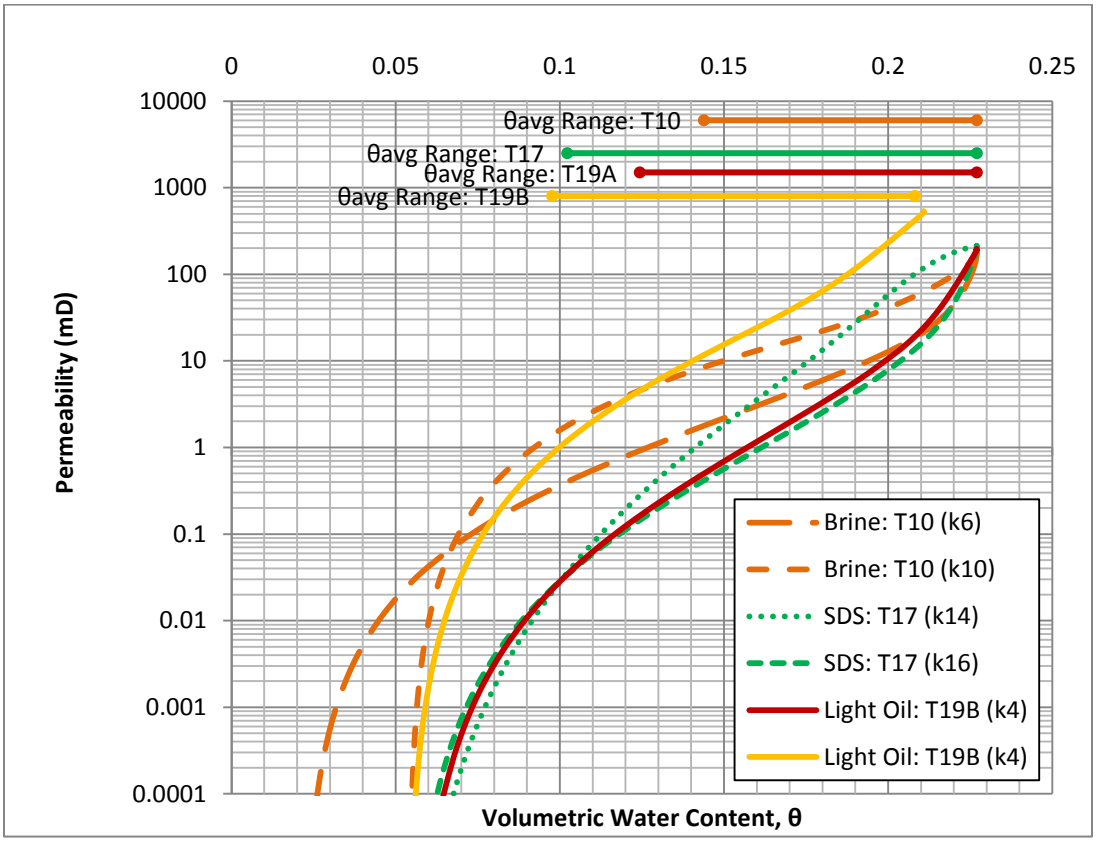

Figure 6.29: Intrinsic Permeability Functions

Figure 6.29 shows the intrinsic permeability for these cores as a function of the wetting fluid content. As observed previously in the saturated hydraulic conductivity data for the light oil and the SDS, the whole permeability function tends to have the same shape, but

is shifted and scaled by the porosity and the actual saturated permeability. Figure 6.30 shows the relative permeability functions plotted against the reduced saturation:

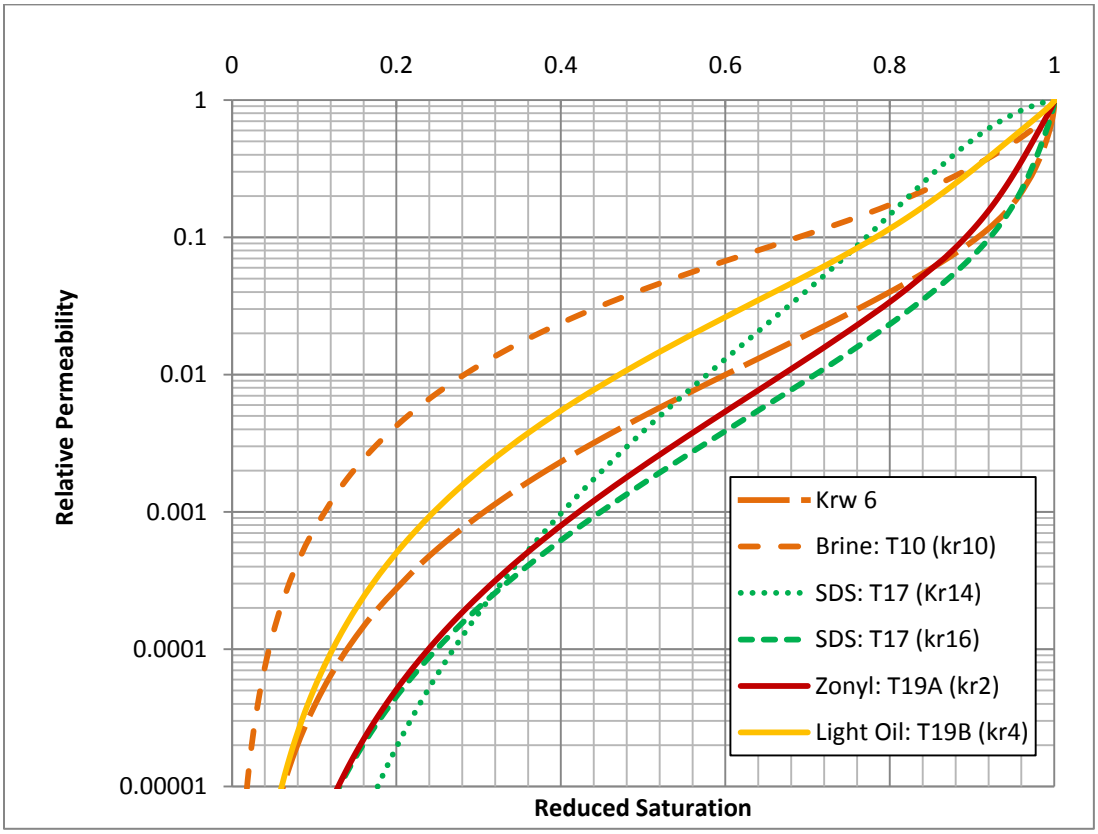

Figure 6.30: Relative Permeability Functions

The functions plotted in Figure 6.30 are normalized by the assumed mobile fluid saturation ($\theta s - \theta r$) and by the saturated hydraulic conductivity. This figure shows that the *relative* permeability functions have similar shapes within the precision of the fitting technique, even though the total permeability functions change from core sample to core sample, and from fluid to fluid, likely based on the diffuse double layer suppression as discussed above. A few other observations are in order from this data. First, the fitting technique is reasonably repeatable to within one and a half orders of magnitude for the hydraulic conductivity using the best possible results from several trials. Second, the oil saturated, oil-wet core seems to obey the same scaling laws as the water-wet, water saturated cores, at least within the range of saturations measured. This helps confirm the

concept of an intrinsic permeability function based on the shape and size of the fluid-filled pores. Finally, the transient time history fitting technique, while reasonably capable, lacks the precision necessary to truly understand the minute differences in the permeability and water content for even these simple systems on homogeneous cores. As shown by several previous researchers, it is ideal to be able to measure internal variables such as local saturation and local capillary pressure in-flight, to help constrain the transient model.

6.5 Comparison with K-functions given by Other Models

6.5.1. Relative Permeability according to Hagoort's Method

Hagoort (1980) developed a method to predict the relative permeability of the wetting phase under centrifugal drainage conditions, by assuming a specific shape of the hydraulic conductivity function and ignoring the capillary pressure. Under these conditions, the transient drainage from a saturated core occurs as a shock front followed by a slow desaturation of the remaining wetting phase in response to the change in hydraulic conductivity with saturation. Their experimental setup consisted of 1 inch diameter, 2 inch long cores placed inside a small centrifuge operated at 3000 RPM (1,400 g's) in one single step. The objective is to drain the core near to the residual saturation very quickly in an effort to observe this plug-flow like behavior and the subsequent slow drainage. After the supposed gas breakthrough, the expectation is that the core will continue to desaturate near the outflow end along with the body of the core, giving a direct measurement of the relative permeability of the outflow end. There is also a small volume correction term in their solution for the "capillary end effect", which is simply the manifestation of the low suction, high saturation portion of the retention curve over the applied suction range, assuming the outflow end is at zero capillary pressure. In order for this manifestation to simply be considered an "end effect", the applied centrifugal potential must be large enough over the majority of the core such that the saturation is also approaching the residual value over most of the core. This translates to the use of

large centrifugal gradients during the test. Whereas the maximum centrifugal gradient used in our tests was only 100 g's, Hagoort (1980) uses a gradient around 1,400 g's. This method, however, does not correctly treat the capillary suction gradient which develops in response to the continuing desaturation behind the shock front. Whereas this method assumes that capillarity is irrelevant behind the shock front, the full theory of retention curves shows that the capillary suction is very sensitive to small changes in saturation near the residual saturation value (Figure 6.31), so instead of the capillary forces becoming negligible behind the shock front, the capillary gradient, $\frac{\partial(P_c)}{\partial S}$, actually should begin to dominate the problem once the shock front has passed.

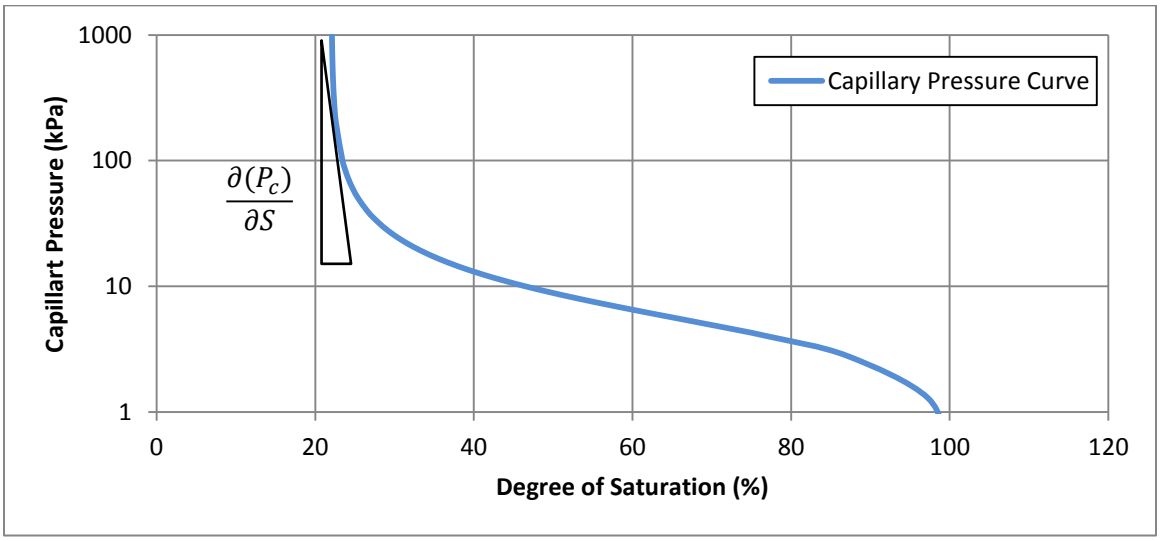

Figure 6.31: Sensitivity of Capillary Pressure gradient at low Saturations

In fact, the capillary suction gradient in the upper regions of the core will steadily climb to eventually meet the applied centrifugal potential as the fluid continues to drain after the shock front has passed. This ultimately means that the *net applied hydraulic gradient* decreases from the original 1,000 g's to asymptotically close to 0 g's during the post breakthrough stages of this test. Consequently, Hagoort's method is expected to produce relative permeability values which could be as much as 1,000 times lower than those given by a full history match. Figure 6.32 shows a comparison between results derived from a full history match and results obtained by Hagoort's method. It is important to

note that the centrifuge gradients used in the single stage tests as part of this study were approximately 10 times smaller than those used in Hagoort's original work. Another important caveat to this comparison is that the best full-history matches were performed on multi-stage tests, while Hagoort's method can only be applied to single-stage tests. These results were obtained from the exact same core plugs, however, so the comparison is still quite relevant.

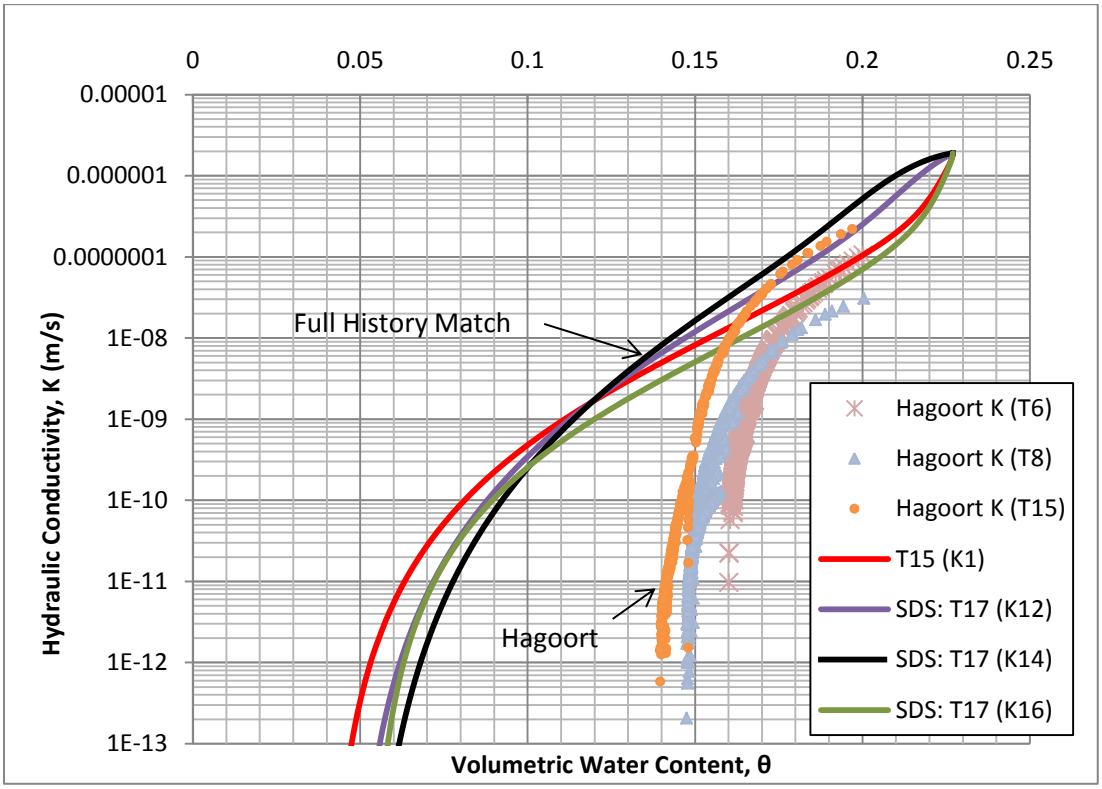

Figure 6.32: Comparison of Numerical History Match and Hagoort Models

As seen in Figure 6.32, Hagoort's method does under predict the hydraulic conductivity by something approaching 2 to 3 orders of magnitude at the lower water contents, due to the assumption that the capillary pressure is irrelevant in the low saturation regime. At best, the results from the full history match can be expected to be reasonably accurate down to a volumetric water content of 0.1, since the lowest measured volumetric water content using the CT was around 0.07. Nonetheless, the results according to Hagoort's method at comparatively low saturations diverge significantly from those predicted from

a full history match. The results from Hagoort's method at higher saturations do, however, fall within the bounds determined from the full history matching scheme, indicating that this method is not completely inaccurate and may provide a valid quick estimate of the conductivity at moderate saturations. Again, the vast difference in the g-levels between the single-stage test as originally envisioned by Hagoort and the tests run in this study prohibits a more robust comparison of the relative merits of Hagoort's analytical model against the full history matching approach. A sample calculation from Test T8 using Hagoort's method is provided in Appendix B.

6.5.1 Van Genuchten Mualem Coupled and Independent Models

One additional model worthy of examination is the Van Genuchten- Mualem model as originally presented by Van Genuchten (1980). In this model, a simplified solution to the capillary network integral allows the hydraulic conductivity function to be derived from the retention curve (Equation 2.23). This coupled model is beneficial because it allows the prediction of the hydraulic conductivity function from the retention curve without the need for tedious simulation of the full time history. We compare the transient outflows for one test (T19B) using the original coupled model implementing the retention curve as established above in Section 6.3, with the time history fits generated using the Van Genuchten- type equations with independent hydraulic parameters (Equation 2.24). Figure 6.33 shows the measured data from Test 19B on the Oil saturated core, along with the numerical matches from the two models:

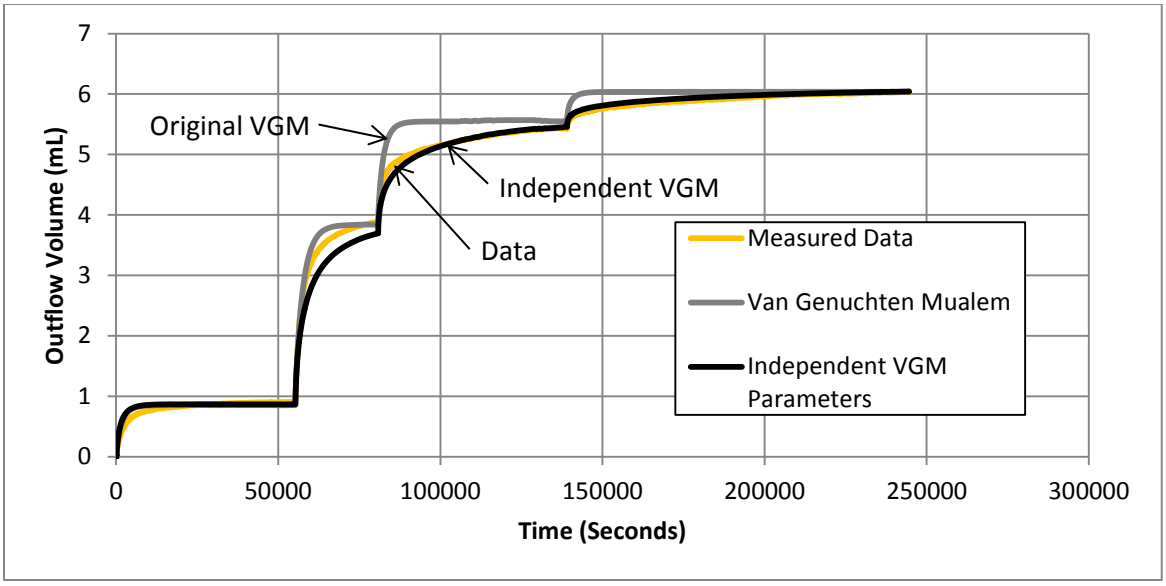

Figure 6.33: Measured data and simulated time histories using different Van Genuchten-Mualem type Models

In Figure 6.33, the models corresponding to the original Van Genuchten Mualem model tend to predict faster initial rates of drainage, followed by a much flatter curve. This indicates that equilibrium is established too quickly in this model, whereas the data show a smoother response to the applied centrifuge gradient. The Van Genuchten-Mualem model which uses independent parameters to describe the retention curve and the K-function is able to predict the measured outflow much more accurately. The speed with which equilibrium is reached in these models is dependent on the hydraulic conductivity function. Figure 6.34 shows the models used in these simulations.

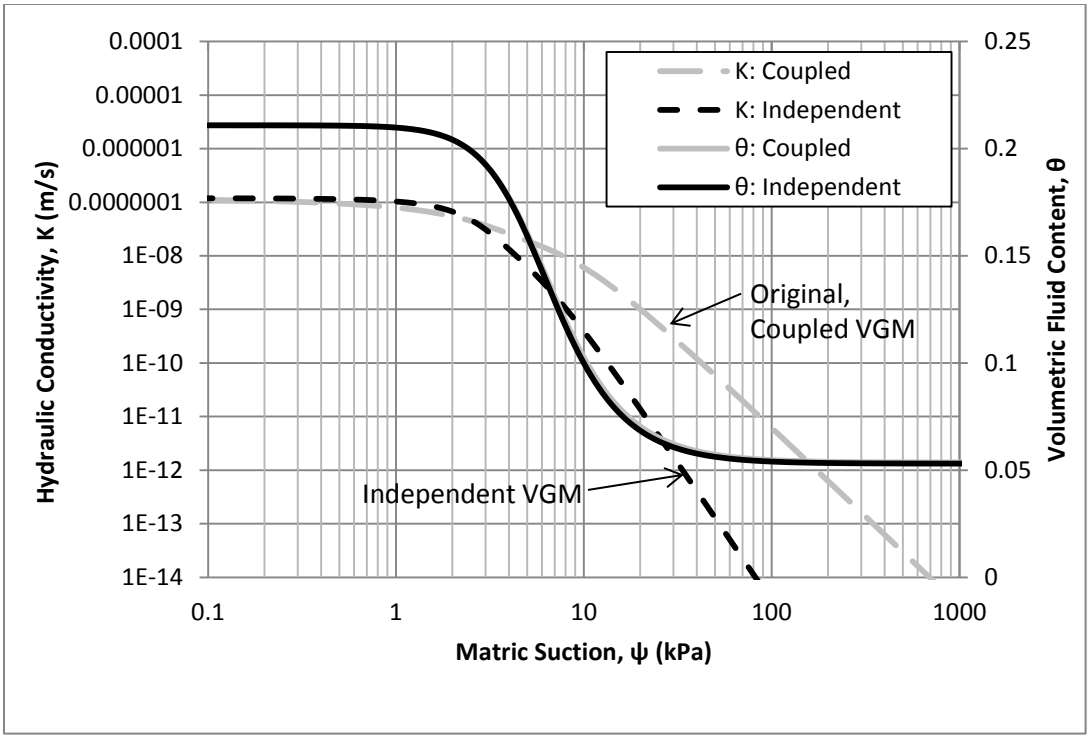

Figure 6.34: Input Hydraulic Models for Van Genuchten Comparisons

Both models have very similar retention curves because they are both constrained to match the endpoints of the measured outflow time histories, however, the independent parameter model predicts a more rapid decay in the hydraulic conductivity as the suction is increased, while the coupled model predicts a higher hydraulic conductivity at large suctions. Figure 6.35 shows the hydraulic conductivity functions plotted against the volumetric fluid content:

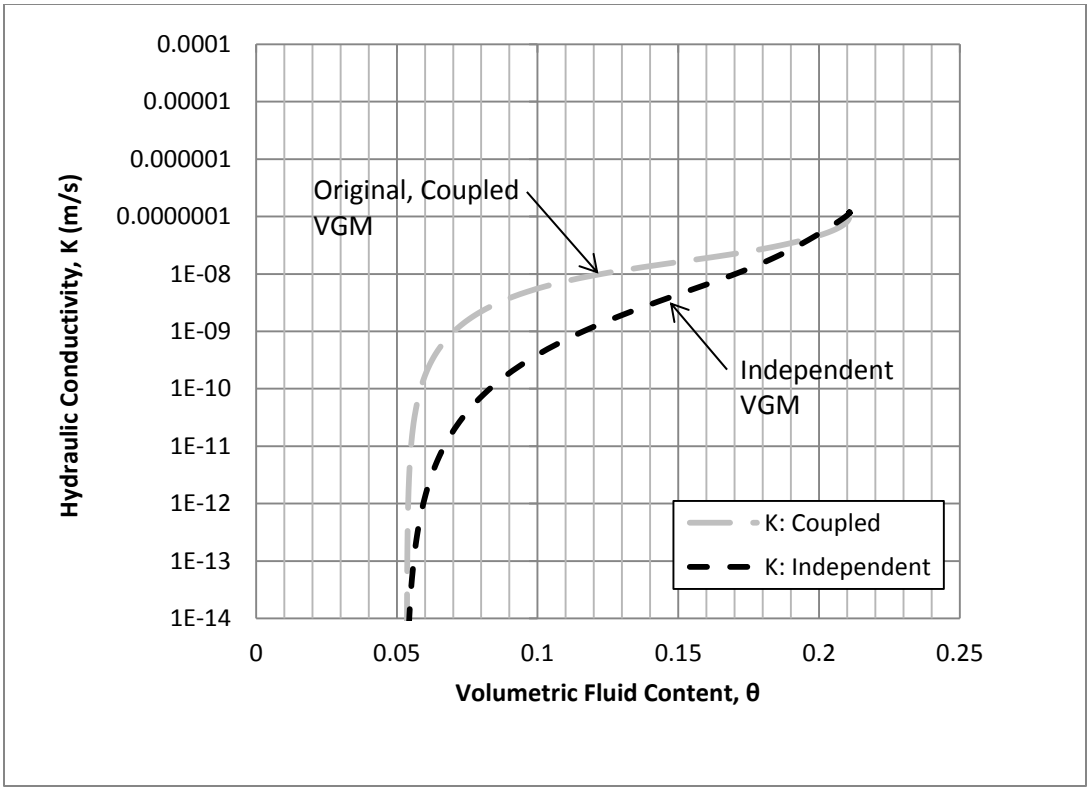

Figure 6.35: Hydraulic Conductivity vs. Fluid Content for Van Genuchten Comparisons

While the two simulations produce notable differences in the time-history, the two functions are within one order of magnitude of one another, even down to a volumetric fluid content of about 0.1. This appears to be a similar spread in the hydraulic conductivity function as derived from better-fitting numerical simulations shown in Section 6.3.2.3for the brine saturated core. As shown in Figure 6.36, however, the coupled Van Genuchten model still falls above the range derived from the independent parameter fits to the brine, as it did in the oil simulations:

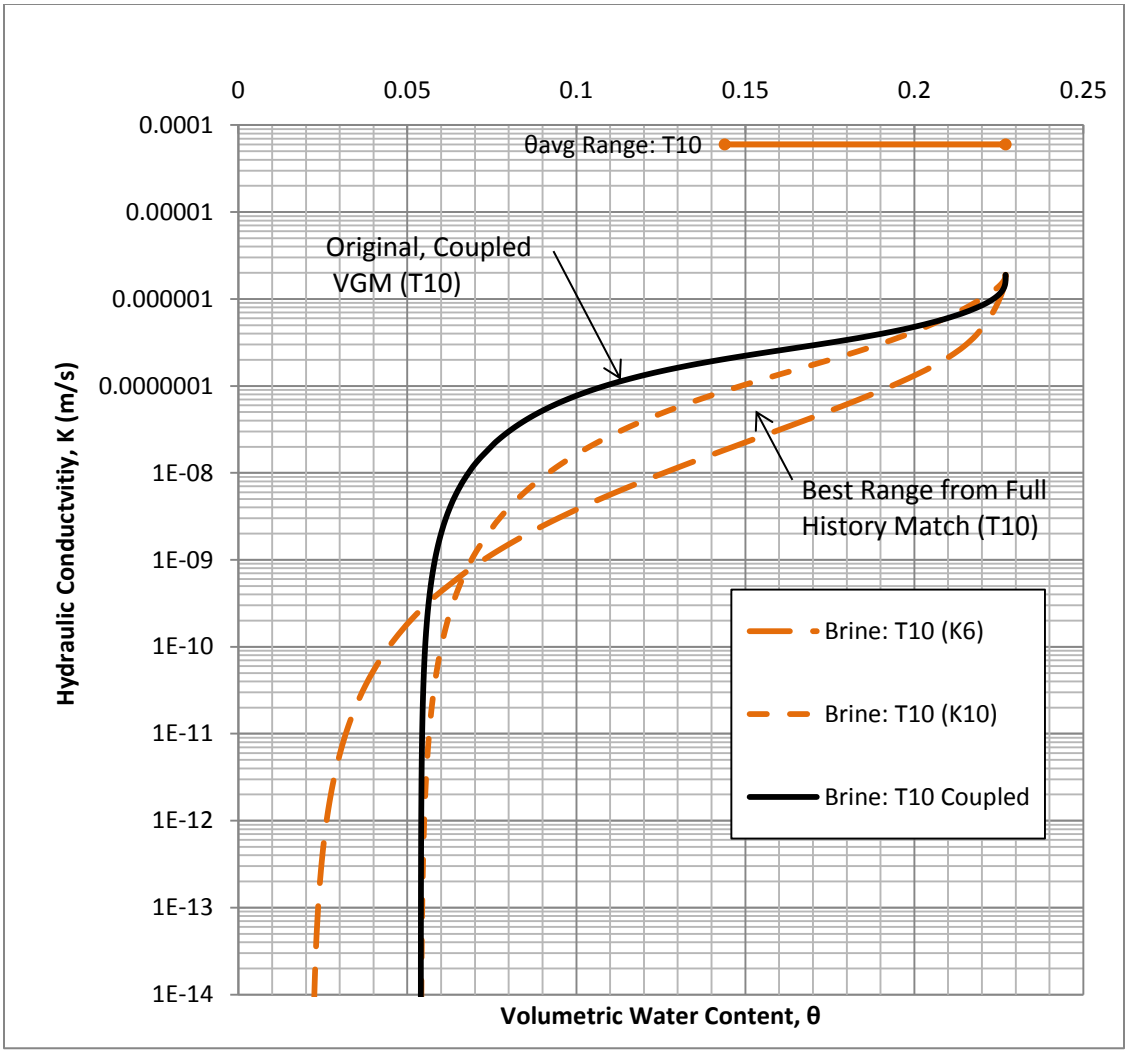

Figure 6.36: Comparison of Coupled Parameter and Independent Parameter Functions for Brine Saturated Cores (T10)

Based on these simulations, it is observed that the original Van Genuchten Mualem model consistently tends to over-predict the hydraulic conductivity function in these sandstone cores for low wetting-fluid saturations.

Chapter 7: Conclusions

Two-phase transient flow tests were conducted in a centrifugal environment to determine the retention behavior and relative permeability functions for Berea Sandstone using several different fluid types. The results generated in this study are deemed applicable to uniform fine-grained materials involving a single wetting fluid being displaced by a gas. All results from this study were generated using flow parallel to the bedding plane under comparatively low confining pressures, and without significant amounts of dissolved gas. Overall, a theoretically consistent interpretation of multi-speed centrifuge outflow experiments accounting for both the capillary pressure curve and the relative permeability curve was found to yield excellent fits to the measured transient data.

- Transient centrifuge measurements of the drainage capillary pressure curve (retention curve) as well as the inferred hydraulic conductivity function were found to be reasonably repeatable.
- The camera system implemented in this study was found to produce precise measurements of outflow to the nearest 0.01 ± 0.005 mL, generating adequate data during late times in long transient tests.
- An analysis of the transient centrifuge data using the analytical method developed by Hagoort, (1980) to predict the relative permeability function, showed that neglecting the capillary pressure gradient at low saturations vastly underestimates the wetting phase relative permeabilities compared to those derived from a theoretically consistent full-history match. On the other hand, this simplified method was found to yield reasonable results for the relative permeability at comparatively high saturations.
- An analysis of the transient centrifuge data using the original Van Genuchten-Mualem model demonstrated that this model overestimates the hydraulic conductivity function for these sandstones when using an experimentally justifiable retention curve to describe the measured data.

- Computed Tomography-derived retention curves on rock samples obtained after spinning in the centrifuge revealed consistent trends with the centrifuge data obtained from multiple runs, complementing the results derived from centrifuge testing.
- The saturated hydraulic conductivity of the Berea Sandstone using the various fluids investigated in this study follows the relationship $K = k\rho g/\mu$ to within a factor of 3.
- The retention curves developed for the Berea Sandstone using four different wetting liquids were found to demonstrate that the capillary pressure curve for a given rock matrix scales by the liquid-gas interfacial tension.
- The hydraulic conductivity functions were found not to scale as accurately by the interfacial tension as did the retention curves.
- The two-phase relative permeabilities for the brine and oil saturated cores were found to reduce to a single function of the wetting phase saturation within one order of magnitude.

Appendix A: Finite Element Implementation of Richards' Equation

Appendix A describes the implementation of the numerical solution to the transient centrifuge flow problem for the purposes of matching the time histories measured in the centrifuge. Included in this section are brief descriptions of the overall history matching process and the Finite Element implementation of the centrifugal Richards' equation.

A transient numerical solution to the centrifugal Richards' equation is the basis for the unsaturated hydraulic conductivity functions generated in this study. In this study, the numerical solution was passively constrained to match the measured time histories from the centrifuge by repeatedly solving the transient problem with randomly selected sets of parameters, and searching for the solution with the minimum error out of the set of trial solutions. This implies that the best solution from each numerical run was not strictly a global, or even a true local minimum for the parameter sample space; however, with enough trial solutions, adequate resolution in each of the input parameters could be obtained, so the results are generally valid. While this method was more cumbersome and inefficient than other available optimization methods, it did generate adequate results for the comparison between numerical history matching and the two analytical models considered in this study. Additionally, the results of good history matches are able to provide a reasonably constrained range for the hydraulic conductivity function, which is one of the primary goals of a transient centrifuge outflow test.

The governing differential equation for two-phase flow in the centrifuge is described by the centrifugal Richards' equation:

$$\varepsilon \frac{\partial S}{\partial \psi}\frac{\partial \psi}{\partial t} = \frac{\partial}{\partial z_m}\left(K(\psi)\left[\frac{\omega^2}{g}(r_0 - z_m) + \frac{1}{\Delta\rho g}\frac{\partial \psi}{\partial z_m}\right]\right) \quad \text{(A.1)}$$

Where ε is the porosity of the rock

S is the degree of saturation of the wetting fluid

ψ is the suction in the porous matrix

t is the time

K is the hydraulic conductivity of the wetting fluid as a function of the matric suction

ω is the rotational speed of the centrifuge

g is the gravitational acceleration at the Earth's surface

r_o is the radius to the free water surface in contact with the specimen

z_m is the coordinate along the length of the specimen, where the positive direction lies toward the axis of centrifugation.

And Δρ is the difference between the wetting fluid density and the invading fluid density. Collectively, the left-hand terms in equation A.1 describe the derivative of the fluid discharge per unit area of the specimen cross section, while the right-hand terms represent the conductivity and the potential gradient across the sample. Integrating Equation A.1 and multiplying by a test function gives:

$$\int_0^L \left(\frac{\partial}{\partial z_m}\left(K(\psi)\left[\frac{\omega^2}{g}(r_0 - z_m) + \frac{1}{\Delta\rho g}\frac{\partial\psi}{\partial z_m}\right]\right) - \varepsilon\frac{\partial S}{\partial\psi}\frac{\partial\psi}{\partial t}\right)\phi_i \; dz_m = 0 \qquad \text{(A.2)}$$

A Finite Element numerical scheme was employed to solve the spatial distribution of the variables, while an iterative time-splitting Finite Difference technique was used to solve temporal distribution of the variables, similar to that employed by Van Genuchten (1978). The resulting linear equation at each half-time step is:

$$[A]^{t+\frac{1}{2}\Delta t}\,(\widehat{\omega})\{a\}^{t+\Delta t} + [B]^{t+\frac{1}{2}\Delta t}\,\frac{\{a\}^{t+\Delta t}}{\Delta t} =$$

$$-[A]^{t+\frac{1}{2}\Delta t}\,(1-\widehat{\omega})\{a\}^{t} + [B]^{t+\frac{1}{2}\Delta t}\,\frac{\{a\}^{t}}{\Delta t} + \{C\}^{t+\frac{1}{2}\Delta t} - \left\{q\;\phi_i\Big|_0^l\right\} \qquad \text{(A.3)}$$

Where:

$$[A] = \int_0^L \frac{K(\psi)^{t+\frac{1}{2}\Delta t}}{\Delta\rho g}\;\frac{d\phi_i}{dz_m}\;\frac{d\phi_j}{dz_m}\;dz_m \qquad \text{(A.4)}$$

$$[B] = \int_0^L \left\{-\varepsilon\frac{dS}{d\psi}\right\}^{t+\frac{1}{2}\Delta t}\phi_i\,\phi_j\;dz_m \qquad \text{(A.5)}$$

$$\{C\} = \int_0^L \{K(\psi)\}^{t+\frac{1}{2}\Delta t}\;\frac{\{\omega^2\}^{t+\frac{1}{2}\Delta t}}{g}(r_o - z_m)\frac{d\phi_i}{dz_m}\;dz_m \qquad \text{(A.6)}$$

$\{a\}^t$ is a vector of matric suction values at each node within the mesh at time *t*

$\{a\}^{t+\Delta t}$ is a vector of matric suction values at each node at time *t+Δt*

$\{a\}^{t+\frac{1}{2}\Delta t}$ is a vector of matric suctions at each node at the half-time $t+\frac{1}{2}\Delta t$

$\widehat{\omega}$ is the time weighting factor, taken as 0.5 in this study

A, and B are matrices containing information from the discrete test function and the discretized basis function. C is a vector containing information from the test function. The term $\left\{q\ \phi_i\Big|_0^l\right\}$ represents the boundary conditions on the 1-D system.

The numerical simulations in this study all used an enforced saturation boundary condition at the outflow end, and a free condition at the top of the core.

Because the hydraulic conductivity, K, and saturation, S, are both non-linear functions of the matric suction, these terms must be estimated at every node at each time-step in order to compute A,B, and C. Thus, equation A.3 is solved iteratively beginning with the initial condition $\{a\}^t$, generating the A, B, and C matrices, and then solving for $\{a\}^{t+\Delta t}$. Then, $\{a\}^{t+1/2\,\Delta t}$ is linearly interpolated as:

$$\{a\}^{t+\frac{1}{2}\Delta t} = \widehat{\omega}\{a\}^{t+\Delta t} + (1-\widehat{\omega})\{a\}^t \qquad \text{(A.8)}$$

The A, B, and C matrices are generated in terms of $\{a\}^{t+\frac{1}{2}\Delta t}$, and the equation (A.1) is solved again. Iteration for a given time step stops once $\{a\}^{t+\Delta t}$has converged to a single profile within some tolerance.

The relations between the hydraulic conductivity, saturation, and suction are modeled using Van Genuchten functions with independent parameters for the K-function and saturation, as described in Section 2.1.

The 2nd order polynomials were used as the basis and test functions. Simulations on these cores typically were run using 100 elements. The time-step size, Δt, was limited to a minimum of the time interval in the measured data and the Courant number criterion, Cr ≤ 1:

$$\Delta t \leq \frac{\Delta z}{q_{outflow}} \qquad \text{(A.8)}$$

The outflow rate, $q_{outflow}$, used in equation A.8 was determined by fitting a 3rd or 4th order polynomial to the outflow data from each centrifuge speed step and calculating the slope of the outflow curve at each point. Δz was determined by the minimum element size. After determining the suction profile at each time step, the saturation profile is calculated from the suction profile, and integrated over the length of the core to give the outflow

volume. The simulated time history is then compared to the measured time history at each measured data point to determine the global error.

Figure A.1 shows sample computed suction and moisture profiles from a simulation:

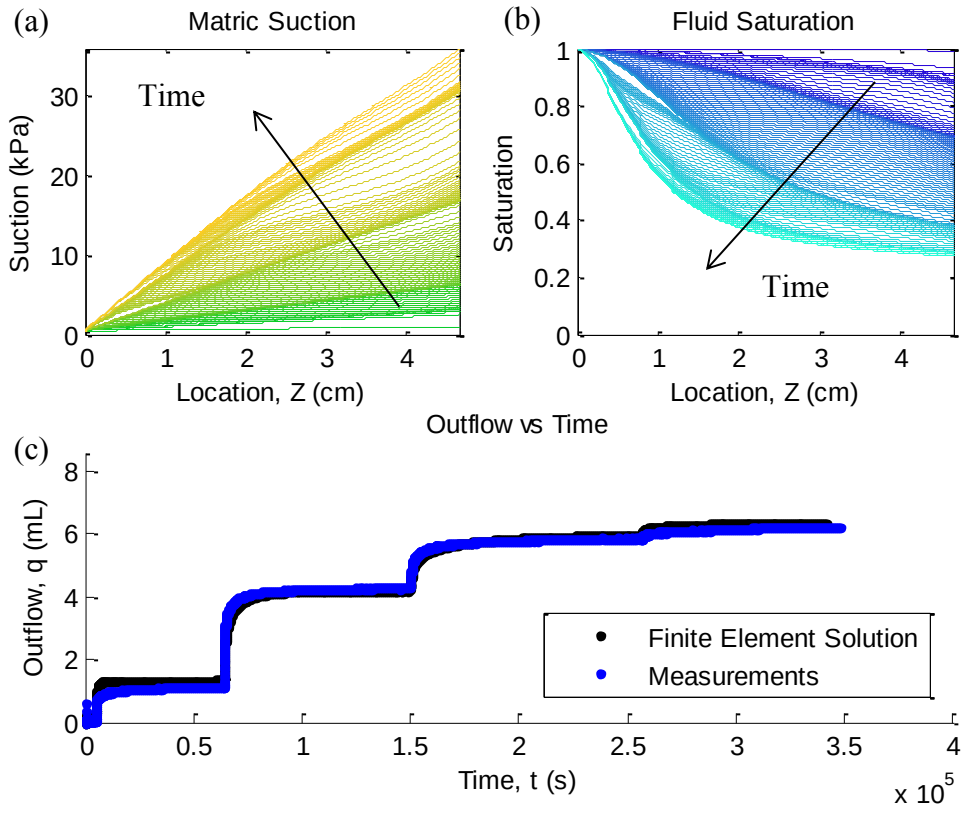

Figure A.1: Numerical Simulations: (a) Suction Profiles (b) Saturation Profiles (c) Outflow Time History

Note that in the suction profiles, time increases from green to orange, while in the saturation profiles, time increases from a dark to light blue color.

All of the Simulations were initialized using a linear profile in saturation, starting at about 100% at the outflow end, and decreasing to a value such that the average across the core would be equal to the average measured saturation at the beginning of the centrifuge test.

Appendix B: Sample Calculation using Hagoort's Method

A sample calculation of the wetting phase relative permeability according to Hagoort's method (Hagoort, 1980) is presented in this appendix.

The measured time-series in Test T8 is plotted in Figure B.1:

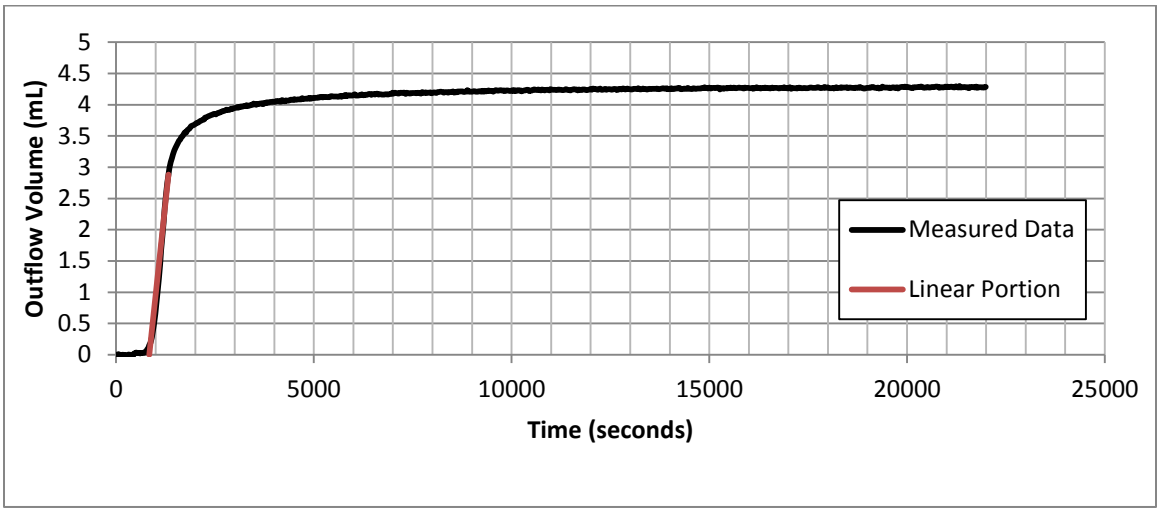

Figure B.1: Measured Time Series

In order to apply Hagoort's method (Hagoort, 1980) to the measured centrifuge data, the time-series is simplified to remove the centrifuge spin-up effects prior to the supposed gas breakthrough. The linear portion of the measured time series is projected back to where it intersects the time axis, which is then defined as the beginning of the experiment, or t = 0.

The dimensionless time is given by:

$$t_D = = \frac{\Delta\rho_{gl} g_a \, k_{sat}}{\mu \phi^* L} t \tag{B.1}$$

Where Δρ is the difference between the gas and liquid mass densities

g_a is the centrifugal acceleration, taken as $g_a = r_{mid}\omega^2$

The cumulative production is given by:

$$N_p = \frac{V_{out}}{V_{pores}} = \frac{V_{out}}{\phi AL} \tag{B.2}$$

Where V_{out} is the measured outflow volume

V_{pores} is the pore volume of the core

ϕ is the porosity of the core

A is the cross sectional area

And L is the length of the core.

The remaining mobile saturation inside the core is :

$$S_o^* = \frac{S_{oil} - S_{org}}{1 - S_{org} - S_{i,cw}} \quad \text{(B.3)}$$

Where S_o is the oil saturation (or water saturation in this case)

S_{org} is the residual oil saturation due to gas displacement

$S_{i,cw}$ is the initial connate water saturation, equal to zero in these tests where water was used as the draining fluid.

In this notation, it is assumed that the draining phase is oil, while some connate water is present in the rock, and the fluid is displaced by the gas. In these tests the draining fluid is the water and no other connate fluid is present, while the gas remains the displacing phase.

Figure B.2 shows the adjusted time-history in terms of the dimensionless units:

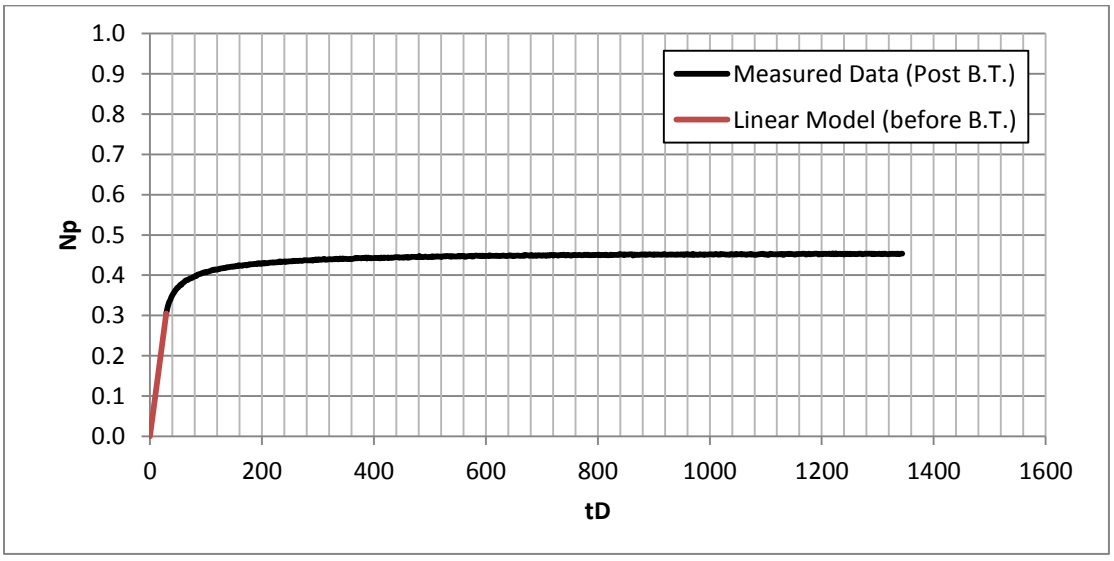

Figure B.2: Adjusted Time History

After Breakthrough, the slope of the production curve is said to be equal to the relative permeability:

$$k_{ro} = \frac{dN_p}{dt_D} \tag{B.4}$$

The data must be smoothed before computing this slope, which was done for these datasets using a moving average of the outflow measurements. The moving average was taken over a range from 4 data points immediately after breakthrough up to 50 points at late times. Once the relative permeability is determined, it is related to the supposed outflow end saturation by the equation:

$$S^*_{oe} = \left(1 - N_p\right) + k_{ro} * t_D \tag{B.5}$$

Figure B.3 shows this curve computed for Test T8:

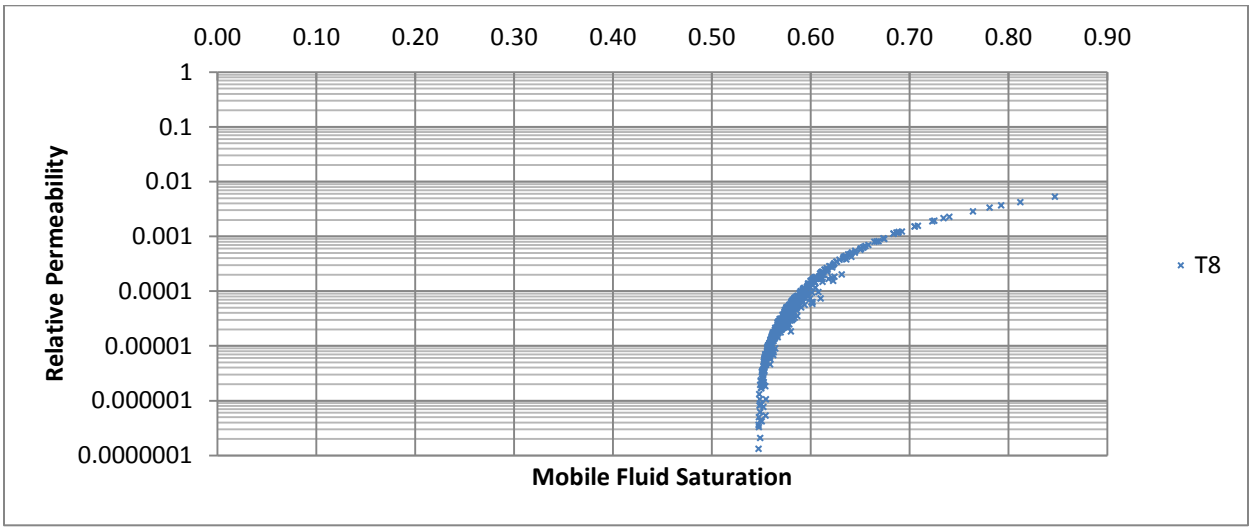

Figure B.3: Hagoort Relative Permeability for T8

The hydraulic conductivity (plotted in Section 6.8) is then determined from the relative permeability as:

$$K = k\, k_{ro} \frac{\rho g}{\mu} \tag{B.6}$$

And the relevant volumetric water content is computed as:

$$\theta = \left(S^*_{oe}\left(1 - S_{org} - S_{cwi}\right) + S_{org}\right) * \phi \tag{B.7}$$

Table B.1 shows the rock and fluid input parameters to the analysis of centrifuge test T8:

Table B.1: Rock & Fluid Parameters for T8

Rock/Fluid				
L	0.04855	(m)	4.85	(cm)
d	0.03775	(m)	3.775	(cm)
A	0.00112	(m2)	11.19241	(cm^2)
V	5.434E-05	(m3)	54.34	(mL)
φ	0.227	( )	0.227	( )
PV	0.0000123	(m3)	12.33	(mL)
Scwi	0	( )	0	( )
θs	0.227	( )	0.227	( )
θr	0.053	( )	0.053	( )
Soi	1	( )	1	( )
Sorg	0.233	( )	0.233	( )
Vom	9.4546E-06	(m3)	9.45	(mL)
φ*	0.174		0.174	( )
ρ liquid	1022	(kg/m3)	1.022	(g/mL)
μ	0.00101	(Pa-s)	1.01	(cP)
σ	0.072	(N/m)	72	(mN/m)
K Sat	5.87791E-06	(m/s)	0.000588	(cm/s)
k Sat	5.9214E-13	(m^2)	600	(mD)
ρ gas	1.2	(kg/m3)	0.0012	(g/mL)

Table B.2 shows the centrifuge parameters for T8:

Table B.2: Centrifuge Parameters for T8

Centrifuge/Gravity				
ω	40.3	(rad/s)	385	RPM
r_o	0.5434	(m)	54.34	(cm)
r_t	0.4949	(m)	49.49	(cm)
g	9.81	(m/s^2)	981	(cm/s^2)
g_a	843.89	(m/s^2)	84389	(cm/s^2)
u	0.000505	(m/s)	0.0505	(cm/s)
N_{cg}	1.066			
N_{gv}	0.0116			
g-level	86.02	(g_0)		

Table B.3 shows sample data from the calculation of the relative permeability for the first six data points post-breakthrough:

Table B.3: Post-Breakthrough Sample Results

tD Adjusted	Np	dNp/dtD OR kro(Soe*)	Soe*	θoe	K = k kro ρg/μ (m/s)	K (cm/s)
28.93885923	0.30	0.005250624	0.85	0.200423	3.08627E-08	3.09E-06
30.73248816	0.32	0.004184182	0.81	0.194322	2.45942E-08	2.46E-06
32.52611709	0.33	0.003648047	0.79	0.190938	2.14429E-08	2.14E-06
34.31974602	0.33	0.003321705	0.78	0.188909	1.95247E-08	1.95E-06
36.11337495	0.34	0.002861328	0.76	0.18598	1.68186E-08	1.68E-06

References

Chen, Q. and Balcom, B.J., 2005. Measurement of rock-core capillary pressure curves using a single-speed centrifuge and one-dimensional magnetic-resonance imaging. *The Journal of chemical physics*, *122*(21), p.214720.

Churcher, P.L., French, P.R., Shaw, J.C. and Schramm, L.L., 1991, January. Rock properties of Berea sandstone, Baker dolomite, and Indiana limestone. In *SPE International Symposium on Oilfield Chemistry*. Society of Petroleum Engineers.

Daniel, D.E. 1989, December. A Note on Falling-Headwater and Rising-Tailwater Permeability Tests. *Geotechnical Testing Journal* GTJODJ, 12(4) pp. 308-310

Dell' Avanzi, E., Zornberg, J.G. and Cabral, A.R., 2004. Suction profiles and scale factors for unsaturated flow under increased gravitational field. *Japanese Geotechnical Society*, *44*(3), pp.79-89.

Firoozabadi, A. and Aziz, K., 1991. Relative permeabilities from centrifuge data. *Journal of Canadian Petroleum Technology*, *30*(05).

Hagoort, J., 1980. Oil recovery by gravity drainage. *Society of Petroleum Engineers Journal*, *20*(03), pp.139-150.

Hassler, G.L. and Brunner, E., 1945. Measurement of capillary pressures in small core samples. *Transactions of the AIME*, *160*(01), pp.114-123.

Holt, R.M., Glass, R.J., Sigda, J.M. and Mattson, E.D., 2003. Influence of centrifugal forces on phase structure in partially saturated media.*Geophysical research letters*, *30*(13).

McCartney, J.S. and Zornberg, J.G., 2010. Centrifuge permeameter for unsaturated soils. II: Measurement of the hydraulic characteristics of an unsaturated clay. *Journal of geotechnical and geoenvironmental engineering*,*136*(8), pp.1064-1076.

Melrose, J.C., 1988. Interpretation of centrifuge capillary pressure data. *The Log Analyst*, *29*(01).

Melrose, J.C., Dixon, J.R. and Mallinson, J.E., 1994. Comparison of different techniques for obtaining capillary pressure data in the low-saturation region. *SPE Formation Evaluation*, *9*(03), pp.185-192.

Nimmo, J.R., 1990. Experimental Testing of Transient Unsaturated Flow Theory at Low Water Content in. *Water Resources Research*, *26*(9), pp.1951-1960.

Reis, R.M., Sterck, W.N., Ribeiro, A.B., Dell'Avanzi, E., Saboya, F., Tibana, S., Marciano, C.R. and Sobrinho, R.R., 2011. Determination of the Soil-Water Retention Curve and the Hydraulic Conductivity Function Using a Small Centrifuge.

Shaw, J.C., Churcher, P.L. and Hawkins, B.F., 1991. The effect of firing on Berea sandstone. *SPE Formation Evaluation*, *6*(01), pp.72-78.

Šimůnek, J. and Nimmo, J.R., 2005. Estimating soil hydraulic parameters from transient flow experiments in a centrifuge using parameter optimization technique. *Water resources research*, *41*(4).

Sinnokrot, A.A., Ramey Jr, H.J. and Marsden Jr, S.S., 1971. Effect of temperature level upon capillary pressure curves. *Society of Petroleum Engineers Journal*, *11*(01), pp.13-22.

Van Genuchten, M.T., 1978. *Numerical solutions of the one-dimensional saturated-unsaturated flow equation*. Water Resources Program, Department of Civil Engineering, Department of Geological and Geophysical Sciences [Princeton University].

Van Genuchten, M.T., 1980. A closed-form equation for predicting the hydraulic conductivity of unsaturated soils. *Soil science society of America journal*, *44*(5), pp.892-898.

Zornberg, J.G. and McCartney, J.S., 2010. Centrifuge permeameter for unsaturated soils. I: Theoretical basis and experimental developments. *Journal of Geotechnical and Geoenvironmental Engineering*, *136*(8), pp.1051-1063.